FLUX GROWTH AND CHARACTERISTICS OF CUBIC BORON PHOSPHIDE

by

UGOCHUKWU NWAGWU

B.S., Pittsburg State University, 2009

A THESIS

submitted in partial fulfillment of the requirements for the degree

MASTER OF SCIENCE

Department of Chemical Engineering
College of Engineering

KANSAS STATE UNIVERSITY
Manhattan, Kansas

2013

Approved by:

Major Professor
J. H. Edgar, PhD

Copyright

Abstract

Boron phosphide, BP, is a III-V compound semiconductor with a wide band gap of 2.0 eV that is potentially useful in solid state neutron detectors because of the large thermal neutron capture cross-section of the boron-10 isotope (3840 barns).

In this study, cubic BP crystals were grown by crystallizing dissolved boron and phosphorus from a nickel solvent in a sealed (previously evacuated) quartz tube. The boron - nickel solution was located at one end of the tube and held at 1150°C. Phosphorus, initially at the opposite end of the tube at a temperature of 430°C, vaporized, filling the tube to a pressure of 1–5 atmospheres. The phosphorus then dissolved into solution, producing BP. Transparent red crystals up to 4 mm in the largest dimension with mostly hexagonal shape were obtained with a cooling rate of 3°C per hour. The crystal size decreased as the cooling rate increased, and also as growth time decreased. The characterization with x-ray diffraction (XRD) and Raman spectroscopy established that the BP produced through this method were highly crystalline. The lattice constant of the crystals was 4.534 Å, as measured by x-ray diffraction. Intense, sharp Raman phonon peaks were located at 800 cm^{-1} and 830 cm^{-1}, in agreement with the values reported in the literature. The FWHM for XRD and Raman spectra were 0.275° and 4 cm^{-1} which are the narrowest ever reported and demonstrates the high quality of the produced crystals. Energy dispersive x-ray spectroscopy (EDS) and scanning electron microscope (SEM) also confirmed the synthesized crystals were cubic BP crystals, with a boron to phosphorus atomic ratio of 1:1. Defect selective etching of BP at 300ºC for two minutes with molten KOH/NaOH revealed triangular and striated etch pits with low densities of defects of ~4 x 10^7 cm^{-2} and 9.2 x 10^7 cm^{-2} respectively.

The BP crystals were *n*-type, and an electron mobility of ~39.8 $cm^2/V*s$ was measured. This is favorable for application in neutron detection. Scaling to larger sizes is the next step through gradient freezing and employing a larger crucible.

Table of Contents

List of Figures

List of Tables

Acknowledgements

First, a special thanks to Dr. James Edgar, my advisor for giving me an opportunity to further my education in chemical engineering, and also for all of his kind support, and excellent guidance throughout my studies. I would also like to extend my thanks to Dr. Larry Glasgow and Dr. Keith Hohn for serving on my advisory committee.

Some of this work would not have been possible without the help of many people. I would like to thank Dr. Rebecca Nikolic and her group at LLNL for packaging devices and electrically characterizing some of the crystals. I want to thank Dr. Yigan Gong and Dr. Kuball at University of Bristol, UK; and also Vika Berry's group especially Phong Nquyen and Vasanta Lakshmi Pallem, for their assistance in Raman analysis.

It was a great honor working with and getting to know several students in my research group including Clinton Whiteley, Yi Zhang, Benjamin Clubine, Clint Frye, Balaji Padavala, Daming Wei, Tashfin Hossain, Timothy Hoffman, and Kevin Cooper. Their contributions to my project meant so much to me, and I wish them success and happiness in their research and future endeavors.

Finally, I like to thank all the faculty and staff of the chemical engineering department whom I had a pleasure to work with during my time at Kansas State University.

Dedication

I dedicate my paper to my family and wife: my mom, Stella Nwagwu; my siblings Chizzy, Chisom, Kelly, Chibueze; and my wife, Crystal, for their unconditional support, patience and constant encouragement during my studies.

Chapter 1 - Introduction

Motivation

Demand for neutron detectors has surged as a result of increased efforts to stop nuclear proliferation and terrorism, but production of helium-3, a critical element in the most common neutron detectors, has not kept pace; existing ^{3}He stockpiles are quickly dwindling (*1*). Helium-3 is a rare isotope that strongly interacts with thermal neutrons; its thermal neutron capture cross-section is 5330 barns (*2*). It is formed when tritium, a heavy isotope of hydrogen that is used to enhance the yield of nuclear weapons, decays. Since 1988, tritium has not been produced and helium-3 is now only obtained from dismantled or refurbished nuclear weapons, which has led to reduced helium-3 production levels (*3*). Furthermore, due to long term stability problems like gas leakage and the inconvenience of replacing pure helium-3 gas, the gas-filled detectors operate at close to atmospheric pressure, therefore reducing its detection efficiency. Highly pressurized large tubes are needed to get a notable electronic signal when a neutron interaction occurs, which results in significant complications in field applications (*4*). To overcome these problems, alternatives are currently in the early stages of development and researchers are pursuing several promising leads for solid state thermal neutron detector concepts (*1*).

Solid-state devices have potentially improved efficiencies compared with gas-filled devices because of the increase in the density of the material (*4*). Furthermore, they will have a more robust, and compact design, which makes it easier for routine deployment and air transport. Table 1-1 shows the elements that have relatively significant thermal neutron capture cross-sections, and their high-energy charged particles produce from their reactions with neutrons.

Table 1-1: Comparison of elements useful for the neutron to charged particle reaction (*2*)

Isotope (% abundance)	Charged Particle Produced	Q Value (MeV)*	Thermal neutron capture cross section (barns)	State of material
^{10}B (19.9)	^{7}Li, α	2.78	3840	Solid
^{6}Li (7.59)	^{3}H, α	4.78	973	Solid
^{3}He (0.000137)	^{3}H, p	0.765	5400	Gas

**Q Value is the kinetic energy released in the decay of the particle at rest.*

Boron-10 (^{10}B) is an excellent neutron absorber with a large thermal neutron capture cross-section of about 3840 barns. This compares favorably with the solid element with the next highest thermal neutron cross section which is ^{6}Li (less than 1000 barns). When ^{10}B reacts with thermal neutrons, two nuclear reactions occurs (*2*):

$$^{10}B + n \rightarrow {}^{7}Li\ (0.84\ MeV) + {}^{4}He\ (1.47\ MeV) + \gamma\ (0.48\ MeV) \quad (94\%) \qquad (2)$$

$$^{10}B + n \rightarrow {}^{7}Li\ (1.02\ MeV) + {}^{4}He\ (1.78\ MeV) \quad (6\%)$$

Both of these reactions produce high energy Li and He (alpha particles) ions. Each neutron captured in a ^{10}B-containing semiconductor will create a large number ($\sim 1.5 \times 10^{6}$) of electron-hole pair as the energetic ions pass through the material. The created charge is large enough to be detected without any amplification. Hence, ^{10}B compound semiconductors can be used in the form of Schottky, *pn*, or *pin* diodes for fabrication of thermal neutron detectors.

Several ^{10}B solid-state thermal neutron detectors concepts have been presented over the years. One of the earlier concepts presented was a layered structure with ^{10}B material as the neutron converter on top of a semiconducting material as the charge-collector (*5*), (see Figure 1-1). The efficiency of this ^{10}B coated device structure was limited because the travel range of the charged alpha particles and Li ions is approximately 3μm in ^{10}B, but, a film thickness of 50μm is needed to absorb most of the neutrons. To improve the efficiency of the ^{10}B coated device, fabrication of pillared devices as shown in Figure 1-1b have been reported, where arrays of *pin* Si pillars are impregnated with a conformal coat of ^{10}B to increase the probability of neutron capture and alpha particle-spawn electronic signals (*4*). Although this improves the overall efficiency from 5% to 25% (*4*), further improvements are possible. To achieve the maximum efficiency possible, the neutron-converter and the charge-collector materials are integrated into a single material (seen in Figure 1-1c), which is a ^{10}B-containing semiconductor, such as boron carbide (*6*), boron nitride (*7*), and boron phosphide (*8*). The outstanding features of cubic BP are a high charge carrier mobility, and *n*- and *p-type* conductivity. These are important for quick transport and collection of the charged particles, and a space charge region to separate mobile charges, which makes it a good fit for neutron detectors application (*1*).

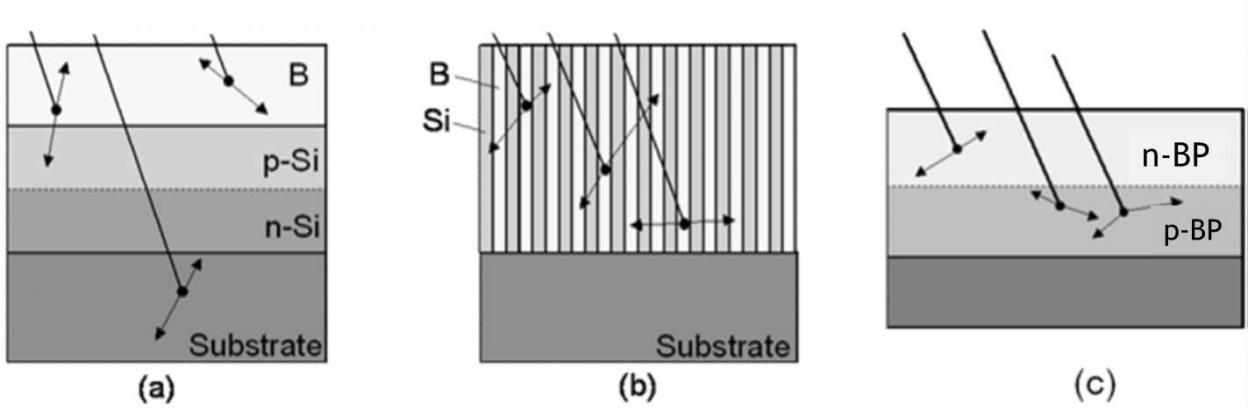

Figure 1-1: Diagrams of neutron detectors depicting (a) a ^{10}B conversion coating on a Si *pn* junction diode; (b) alternating narrow pillars of ^{10}B for conversion and Si for charge collection; and (c) single ^{10}BP crystal as both the neutron-converter and collector. The dots represent the ^{10}B-neutron reaction

Goal

In order to fabricate a device using a high quality BP crystal with low charge trap densities, it is best to establish a bulk BP crystal growth technique. The goal of this study is to grow reasonably large BP crystals of high structural quality and low residual impurity concentrations. Having large crystals will make it easier to fabricate devices, and high structural quality and low impurity concentrations are necessary to obtain the best electrical properties.

Crystalline Boron Phosphide

Boron phosphide (BP) is a III-V compound semiconductor with a wide band gap of 2.0 eV. Its synthesis was first reported in 1891 by Henri Moissan (*9*). Although the structure and composition of the BP produced was unknown, Moissan reported preparing BP by reacting boron halides with phosphorus. Over the years, there has been little interest in the applications of BP; its development has been considerably slower than other III-V compounds because of its unusual properties and the difficulties of preparation of single crystals with high structural quality. Recently, as new controllable synthesizing techniques emerge, BP, because of its high thermal conductivity, chemical stability, mechanical strength, and charge mobility, has been considered for application in electronic devices that can operate in extreme conditions of high temperature, and under intense radiation (*10, 11*).

Structure

Although boron phosphide had existed for many years, its wasn't until 1957 that Popper *et al* (*12*) determined it has a zinc-blende structured crystal. BP, usually referred to as cubic boron phosphide or boron monophosphide, has the zinc blende structure made up of light elements of boron and phosphorus that exhibits strong covalent bonding because the electro-negativities of boron and phosphorus are almost exactly the same. Its lattice constant is 4.538Å (*11*, *13–16*) which is similar to that of both 3C-silicon carbide (SiC) 4.36Å, and gallium nitride (4.51Å for cubic GaN (*17*)). BP also has a compact crystal structure because of the small atomic radius of boron (0.82 pm) which gives it a great stability advantage over other III-V compounds (Al – 1.18 pm, Ga -1.26 pm, In -1.44 pm, P – 1.06 pm) (*18*). These stabilizing effects leads to a larger orbital overlap and a higher ionization energy (*11*). Although BP has high stability, it decomposes to boron subphosphide, B_6P (aka icosahedral boron phosphide, $B_{12}P_2$) at elevated

temperatures (> 1100ºC) and low phosphorus pressures (<1 atm) by losing phosphorus. Figure 1-2 illustrates the crystal structures of both boron phosphides.

$B_{12}P_2$ has a rhombohedral unit cell containing 12-boron atom icosahedra at each of its eight vertices with a pair of phosphorus atoms in the center (*19*). The phosphorus atoms are bonded to each other and to three adjacent icosahedrons. The icosahedral structure has an unusually strong three-center covalent bonding between its boron atoms, the result of electron deficient bonding: where two valence electrons are shared between 3 atoms (*19*). This feature in the structure of $B_{12}P_2$ makes it extremely stable and also chemically inert, with a high melting point of 2700K. However, its unique bonding structure changes some of its properties and adds some special effects (*20*). For example, it usually has a *p*-type conductivity, while cubic BP can be either *p*- or *n*-type. The band gap is 3.3eV as opposed to 2.0 eV (*21*, *22*) for cubic BP. And finally, it "self-heals" when bombarded with radiation (*20*). Both BP and $B_{12}P_2$ can be thermodynamically stable compounds depending on the process conditions. BP is favored at relatively high phosphorus vapor pressures, while $B_{12}P_2$ is favored at low phosphorus vapor pressures and high temperatures.

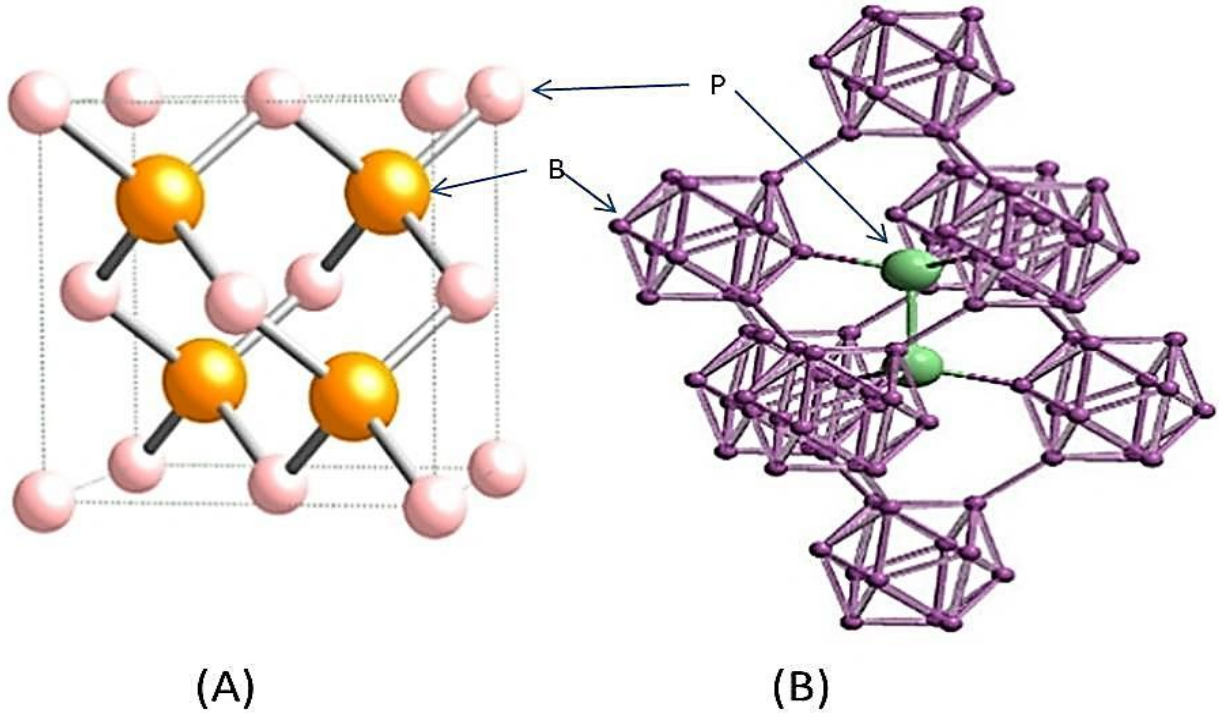

Figure 1-2: Crystal structures of (A) cubic BP and (B) icosahedral $B_{12}P_2$

Electrical and Physical Properties

As with other group III-V compounds, cubic boron phosphide (BP) has been of interest because of its semiconducting properties. When compared to other III-V semiconductors, crystalline BP has several distinct properties that make it useful for niche electronic devices (*13*). Its wide band gap gives it a low intrinsic conductivity at room temperature. It also has a high melting point, greater than 3000°C (*11*), which makes it an ideal candidate for high temperature electronic devices. And as mentioned previously, the ^{10}B isotope has a large thermal neutron capture cross section that is suitable for neutron detectors.

Table 1-2 compares some properties of cubic BP with some group III-V and IV compounds used for devices.

Table 1-2: Selected properties of some III-V and IV compounds (*23–27*)

	BP	GaN	AlN	InN	GaAs	Si	3C-SiC
Structure	Z.b	Wurtzite	Wurtzite	Wurtzite	Z.b	Diamond	Z.b
Band gap (eV)	2.0 (Indirect)	3.4 (Direct)	6.2 (Direct)	1.89	1.4	1.1	2.39 (Indirect)
Lattice constant, a, c (Å)	4.538	3.189 5.185	3.112 4.982	3.540 5.705	5.653	5.431	4.3596
Density, (g/cm^3)	2.94	6.1	3.26	6.88	5.32	2.33	3.17
Mohs hardness	9.3				4.5	7	9.2-9.3
Thermal expansion coefficient ($10^{-6}K^{-1}$)	~3.6	5.59	5.3		6.0	2.6	3.9
Melting point (ºC)	>2000	>1700	3000	1100	1238	1415	2730
Thermal conductivity (W/cm*K)	4.0	1.5	2		0.46	1.5	3.2
Refractive index	3.4				3.3	3.42	2.55

Compared to other boron compounds, crystalline cubic BP has several advantages that are essential for electronic devices. First, BP is one of the few boron-based compounds that can be doped to produce both *p* and *n*-type conductivity (*28*); unlike the icosahedral pnictides, $B_{12}As_2$ and $B_{12}P_2$, which have always been reported to exist with *p*-type conductivity (*19*). BP also has relatively high charge mobility. Studies have reported that the hole mobility of doped BP ranges from 20-350 cm^2/V-sec (*29*) and the electron mobility from 107- 120 cm^2/V-sec (*10*), depending on the crystals' impurity and defect concentration. The high charge mobility of BP is

important for charge transport, and it is good enough for efficient operation of electronic devices. Table 1-3 shows typical properties of boron-based compounds.

Table 1-3: Typical properties of some boron-based compounds (*13*, *16*, *27*, *29–36*)**.**

	BP	**B_4C**	**BAs**	**$B_{12}P_2$**	**$B_{12}As_2$**	**cBN**
Color	Reddish brown, transparent	Orange, yellow	Dark brownish	black, blue, transparent	Amber, transparent	Black, golden
Structure	Cubic	Rhombo-hedral	Cubic	Rhombo-hedral	Rhombo-hedral	Cubic
Lattice constant, a, c, (Å)	4.538	5.987 11.841	4.777	5.987 11.841	6.156 11.929	3.615
Melting point (°C)	>2000	2450		2120	2027	
Band gap (eV)	2.0 (indirect)	2.5	1.46	3.35	3.34	6.4(indirect)
Resistivity, (Ω-cm)	*p*-type, 10-12.5 *n*-type, 0.15-2.5	0.1-10	*p*-type, 0.01	*p*-type, 5.2e+4, 9.2e+4	*p*-type, 10^4-10^5	*p*-type, 1-1000 *n*-type, 1-1000
Mobility (cm^2/V sec)	20-350	<1	100-400	50	80	0.2-4
Holes						
Electrons	107-120					
Thermal conductivity (W/cm-K)	4.0	0.29-0.67		0.38	1.2	4-7

Crystal Growth Methods of BP

It is difficult to synthesize crystalline BP from the melt due to its high phosphorus vapor pressure at its melting temperature. Hence, over the years, many other methods have been employed to synthesis BP crystals including chemical vapor deposition (CVD) (*37*, *38*), chemical vapor transport (CVT) (*13*, *30*), flux growth (*39*), and high-pressure, high temperature growth methods (*11*, *14*, *21*). Of these, CVD and flux growth methods have been the most widely used because of their ability to produce BP crystals at relatively low temperatures (<1400°C).

Chemical Vapor Deposition (CVD)

One of the most reported techniques used for BP synthesis is the CVD method for epitaxial film growth on silicon (Si) (*29*, *32*) or much less common growth on hexagonal silicon carbide (SiC) (*40*) substrates. Thin BP films are produced from gas phase reactants in an open system as illustrated in Figure 1-3. The BP deposition can be carried out using thermal decomposition of hydride - diborane (B_2H_6) and phosphine (PH_3) in a hydrogen atmosphere or by using the thermal reduction of halides - boron tribromide (BBr_3) and phosphorus trichloride (PCl_3) mixtures with hydrogen gas.

$$\begin{aligned} B_2H_6 + 2PH_3 &\xrightarrow{Heat} 2BP + 6H_2 \\ BBr_3 + PCl_3 + 3H_2 &\xrightarrow{Heat} BP + 3HBr + 3HCl \end{aligned} \qquad (1)$$

For the thermal decomposition of hydrides, B_2H_6 (1% in H_2) and PH_3 (5% in H_2) are introduced as reactants into a fused quartz tube chamber leading to BP deposition on a substrate placed on a susceptor externally heated by an RF generator. With the chamber wall water cooled to minimize gas phase reaction, the substrate is heated to temperatures ranging from 950 to 1250ºC. At such high substrate temperatures, the phosphorus partial pressure needs to be higher than that of BP's vapor pressure (*40*); therefore the flow rate of PH_3-H_2 is at least several times that of the B_2H_6-H_2 to insure the formation stoichiometric BP and not $B_{12}P_2$ (*29*). The outcomes of BP deposition can be an amorphous, polycrystalline or single crystal film, with *p*-type or *n*-type conductivity depending on the variation of the PH_3-H_2 flow rate ratio to B_2H_6-H_2 and also substrate temperature (*29*).

When using BBr_3 and PCl_3 as reactants, the apparatus is basically the same as with B_2H_6 and PH_3, but the carrier gas is bubbled through two constant temperature bubblers containing liquid BBr_3 and PCl_3 to pick up these vapors (*40*).

BP films are typically deposited on Si and SiC substrates, but mismatch of the film-substrate properties like lattice constants and thermal expansion coefficient creates stresses, defects and contamination from the substrate, thus degrading the quality and properties of the BP films. Silicon substrates have a large lattice mismatch of 16%, but are the most common substrates used for epitaxial growth because they are readily available with *n* or *p*-type conductivities, inexpensive, exists in many orientations, and also can be selectively removed from deposited BP film (*31*, *32*, *41*). Quality BP films are grown at high temperatures (>950ºC), but at these temperatures silicon diffuses into the deposited BP films, thus, degrading its electrical properties (*42*). Rough surface morphology and cracking in BP films is typical due to the strains caused by the lattice mismatch and the difference in thermal expansion coefficients of BP and Si (*42*). The strain causes the BP film to bow after the removal of silicon (*31*). The lattice mismatch of BP on SiC is much smaller, about 4%. SiC is thermally stable and inert with a high melting point of 2730ºC, and is therefore much less likely to contaminate the deposited BP film. Also, the thermal expansion coefficient of SiC and BP are very close when compared to Si (*27*), as shown in

Table 1-2. The high cost of high quality SiC and its inability to be chemically removed substrates has limited SiC use.

It is relatively easy to dope films in the CVD technique. However, it is difficult to grow really thick (> 50 μm) films by CVD, and the defect densities are much higher in the thin films compared to bulk crystals.

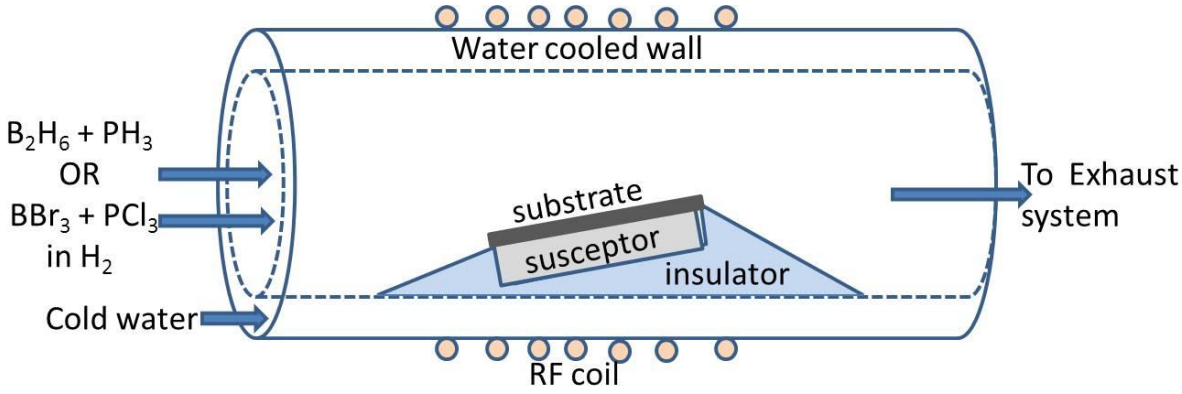

Figure 1-3: Schematic illustration of a CVD reaction chamber

Flux Growth

The flux growth method avoids some of the problems associated with the CVD method like lattice mismatch and thermal expansion coefficient differences between the grown film and the substrate. Like the melt growth technique, it also involves liquids but uses a solution that is heated to high temperature to form a homogeneous liquid. The melt growth technique usually has higher growth rates and has no contamination from a solvent. Flux growth is relatively simple, and achieving high phosphorus vapor pressure is also possible.

In the flux growth method, the material to be crystallized is dissolved in a solvent and then crystallization occurs as the solution becomes critically supersaturated (*43*) as shown in Figure 1-4. Supersaturation is promoted either by cooling the solution or by a transport process in which the solute is dissolved in a hotter region where the solubility is greater and precipitated in a cooler region, where the solubility is reduced (*43*). The key advantage of using a solvent is that crystal growth occurs at a lower temperature than the melting temperature of the solute. Additional advantages to flux growth are that the growing crystal is not exposed to steep temperature gradients and also the crystal can grow without any mechanical or thermal constraints (*43*). When compared to crystals from CVD method, it often results in a better crystal quality with respect to stresses and defects. However, this method has some disadvantages, like substitutional or interstitial incorporation of solvent atoms or ions into the crystal, microscopic or macroscopic inclusions of impurities, non-uniform doping, and a slow growth rate (*43*). The flux growth method can produce high quality large size crystals for electronic devices with careful attention to the choice of solvent and the experimental conditions for stable growth (*43*).

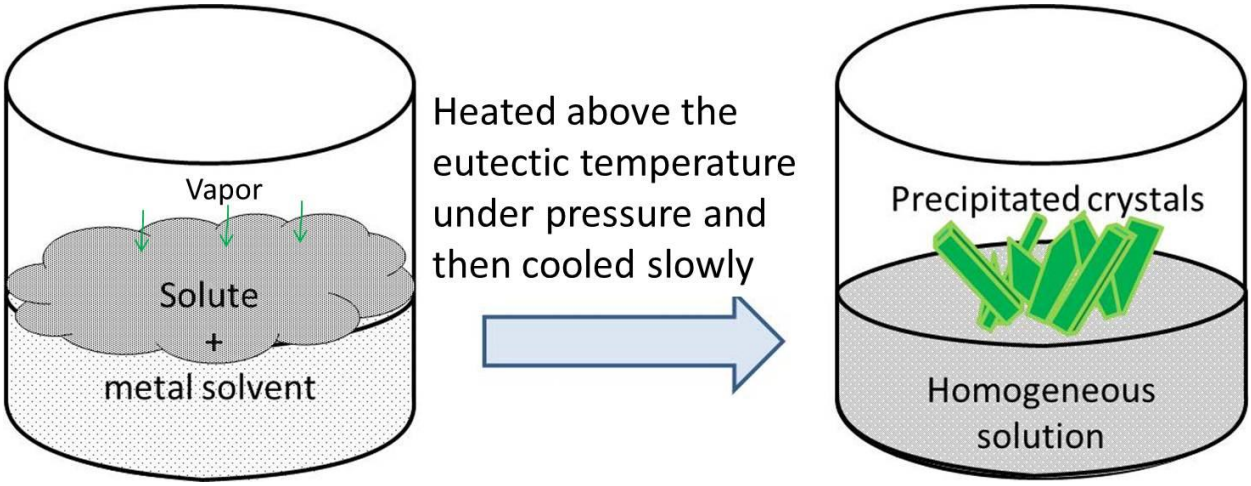

Figure 1-4: Schematic depicting precipitated crystals from solution in flux growth method.

In this study, bulk BP crystals were grown by the flux method, using a molten metal solvent to dissolve boron and phosphorus at lower temperatures (< 1200ºC). BP crystals precipitate when the solution is cooled. In this process, it was important to know which solvent has the best solubility of boron or boron compounds, low vapor pressure, and the least reactivity with boron. Platinum, nickel, copper, iron, and their phosphides are all potential solvents capable of dissolving boron at lower temperatures (*14*, *28*, *39*, *44*, *45*). Several studies have reported producing 1-8mm sized BP crystals by dissolving BP powder in a copper, nickel, or their phosphides (Ni_5P_4, Cu_3P) at high temperatures (1200-1400ºC) and pressure (2-18 atmospheres) (*39*, *45*). A summary of some of these studies of BP growth by flux method is shown in

Table 1-4. Yamamoto *et al* (*44*) grew up to 3 mm size BP crystals in Cu solvent, and were able to prove that the crystal size was a function of the growth temperature. At elevated temperatures, phosphorus vapor pressure above atmospheric is needed to form BP to and not $B_{12}P_2$. To prevent this, Kumashiro *et al* (*45*) employed high pressure of 18 atm to grow BP crystals at 1400°C. Chu *et al* (*39*) grew BP at a lower temperature of 1200°C with a much lower pressure of 1-5 atm. He also introduced a technique where the Ni_2P-BP-P solution was rotated during growth to form a homogeneous mixture. The technique insured that all BP powder dissolved in the solution; as a result, larger crystals were grown.

Nickel solvent was preferred in this study because of the high boron solubility, which is Ni-45at.%B at eutectic temperature of 1018°C (see binary phase diagram in Figure 1-5) (*46*), and also it is cheaper compared to platinum (which is also a good solvent). Instead of adapting the rotation technique reported by Chu *et al* (*39*) to form a homogenous mixture, the nickel and boron eutectic solution was held at a growth temperature for various periods of times in the absence of phosphorus vapor; this will be referred to as the soak time. Phosphorus vapor was then transported to the nickel-boride (Ni-B) solution where it reacted with the dissolved boron to form BP crystals at lower pressure (1-3 atmospheres) and growth temperature (1150°C). Since the size and purity of the crystals are essential for fabrication of neutron detectors, the effects of parameters such as the soak time, growth temperature dwell time, cooling rate, and source material purity, were studied to optimize the conditions for stable growth, produce high quality and purity and large size crystals at the adapted lower growth temperature and pressure.

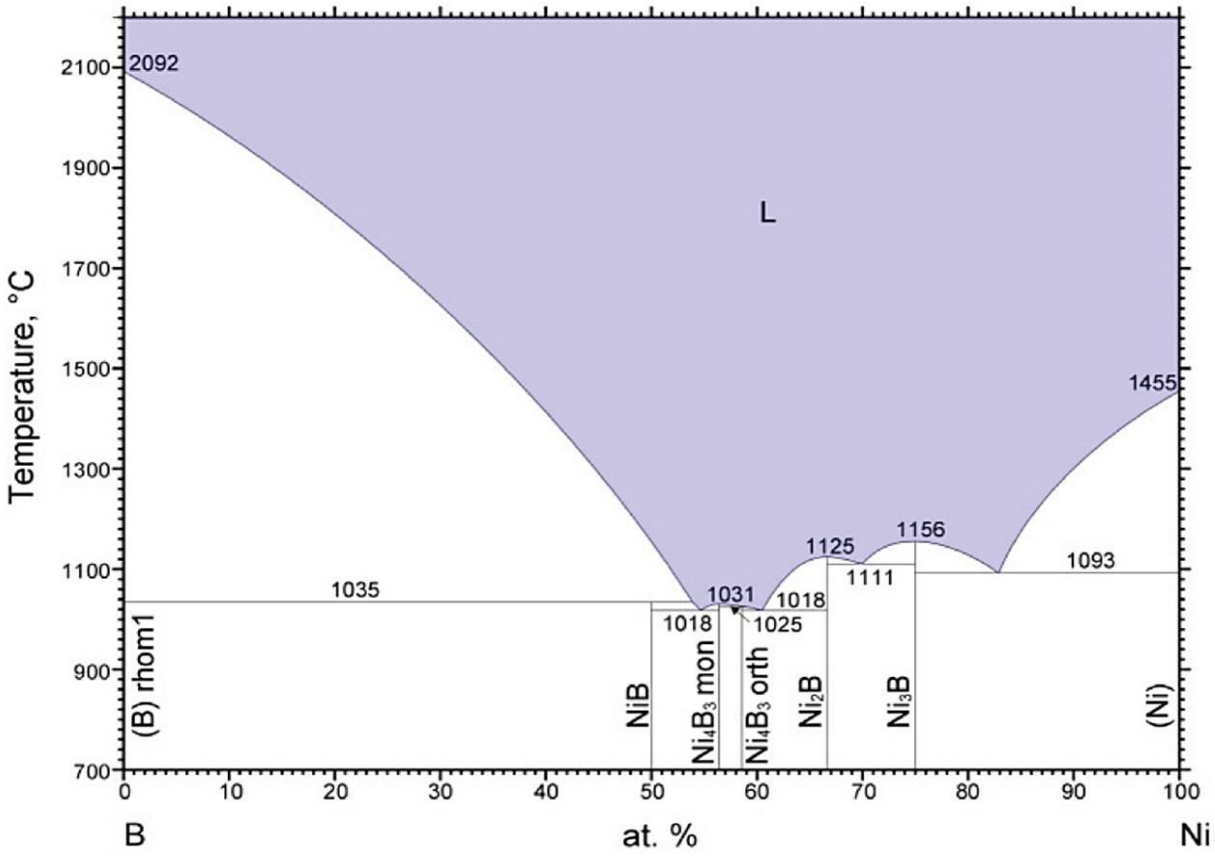

Figure 1-5: The nickel boron binary phase diagram. The liquid phase is maintained down to the eutectic temperature of 1018°C (55mol% Ni) (*46*)**.**

Table 1-4: Summaries of other studies of BP growth by flux method.

Solvents	Solution temperature	Phosphorus pressure	Max. crystal size	Growth time	Comments	References
Cu	1180-1270°C	_	3 mm	24 hr.	Size as a function of temperature	Yamamoto *et al* (*44*)
Cu_3P	1400°C	18 atm.	5 mm	120 hr.	BP powder as source	Kumashiro *et al* (*45*)
Ni_2P	1200°C	1-5 atm.	5-8 mm	4 weeks	Solution rotated at 120 rpm	Chu *et al* (*28*, *34*, *39*)
_	_	_	1 mm	_	Slow cool	Stone *et al* (*14*)
Ni	1250	1 atm.	5 mm	_	Gradient cooling	Iwami *et al* (*37*, *47*)

Chapter 2 - Experimental

The main focus of this project is the flux growth of cubic BP crystals using nickel as the solvent in a sealed vacuum quartz tube. This closed system was necessary to maintain the vapor pressure of sublimed phosphorus. There are many benefits associated with this technique, such as the ability to produce large and well-orientated crystals. Unlike the CVD technique, crystals produced are highly crystalline, and have no structural constraints and minimal defects. Nickel was chosen as a solvent because of its relatively low cost and its ability to dissolve large amounts of boron.

The unintentional incorporation of impurities into the crystals is a concern, not only the solvent, but also impurities in the tube and source materials. Oxygen and carbon are of particular concern. The use of high purity source materials (B, Ni, & P) may reduce the amount of impurities in the produced BP crystals. Also, the introduction of oxygen-savaging material like aluminum or titanium at elevated temperature could reduce the oxygen content of the crystals. Therefore, experiments were conducted to understand techniques that would lead to high quality bulk BP crystal. This work describes the synthesis of bulk BP crystals through nickel-fluxed melt. X-ray diffraction, Raman spectroscopy, photoluminescence spectra, energy dispersive x-ray spectroscopy (EDS) and scanning electron microscope (SEM) were used to characterize the BP crystals produced. Lastly, simple devices were fabricated and tested.

Materials and Methods

Crystal Growth

In a conventional experiment, 10.42g (0.178mol) and 1.57g (0.145mol) of pure nickel and boron powders respectively, which is approximately the eutectic composition of boron and nickel binary system, were mixed in a pBN sample boat. 10g (0.322mol) of pure phosphorus powder was then placed in the closed end of a quartz tube, which is enough to form a 1:1 stoichiometric BP ratio, as well as 1:1 NiP ratio. Next, the sample boat containing B-Ni powder mixture was placed in the center of the quartz tube (already containing phosphorus). After loading the sample into the quartz tube, the quartz tube was connected to a vacuum system (see

Figure 2-1) and heated with heating tape to about 125°C while under vacuum to remove volatile impurities. The system was evacuated by the mechanical pump to a pressure of 10^{-4} torr and then purged twice with argon. After purging, the system was evacuated to 10^{-4} torr again, and then was vacuumed overnight to about 10^{-6} torr with the turbo pump. The quartz tube was then sealed under vacuum and placed into a multi zone furnace as illustrated in Figure 2-2.

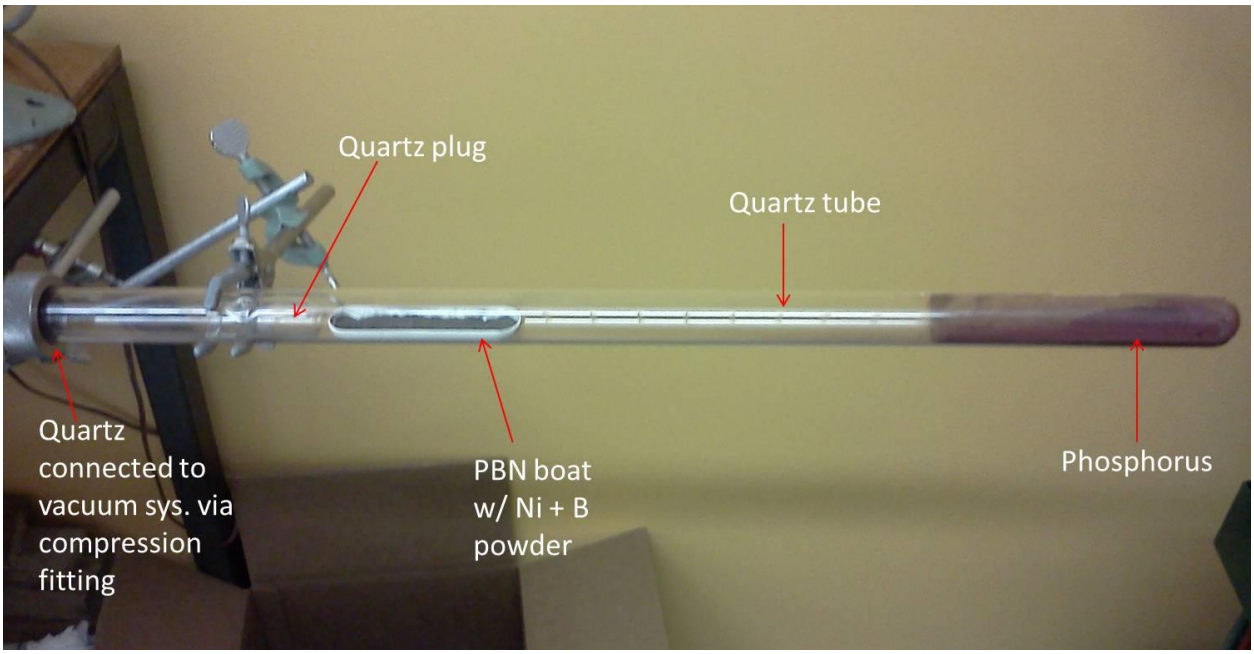

Figure 2-1: PBN boat with boron and nickel in a quartz tube (containing phosphorus) connected to a vacuum system. The system was evacuated to a pressure of 10^{-6} torr with a mechanical pump and a turbo pump.

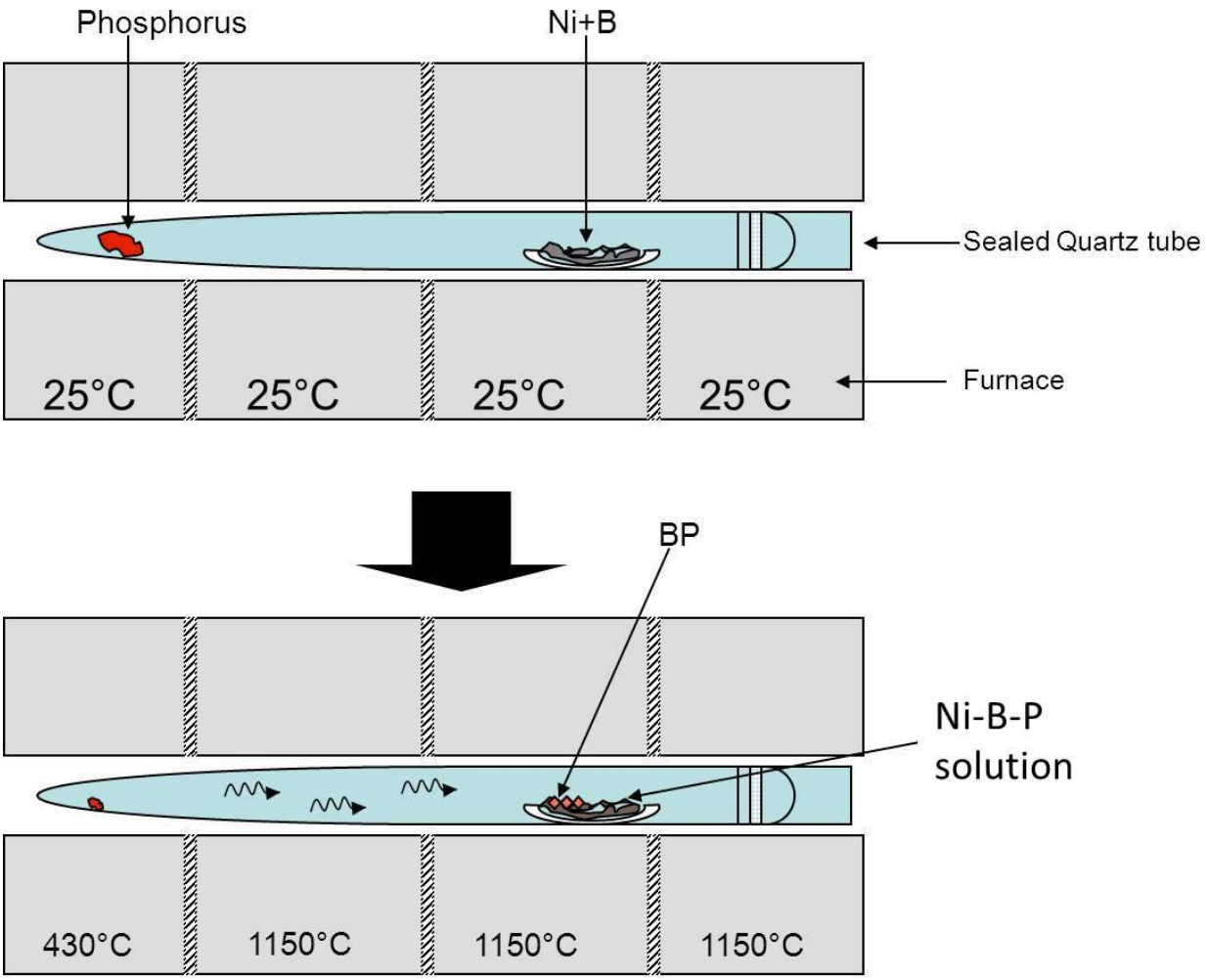

Figure 2-2: Schematic diagram of the flux growth process. (Top) Initially, reactants are positioned in an evacuated quartz tube at room temperature. (Bottom) BP crystals precipitate as sublimed phosphorus reacts with dissolved boron at elevated temperatures.

To allow the boron to completely react with nickel before reaction with phosphorus occurs, the end containing nickel and boron was first heated to and allowed to dwell for 24 hours (soak time) at 1150°C, while the other end containing red phosphorus was slowly heated to 430°C within 24 hours. Figure 2-3 illustrates soak and dwell times with temperature versus time plot for the hot and cold zones of the furnace. The phosphorus end temperature was heated to 430°C to keep the system's phosphorus pressure at between 1 - 3 atmospheres. It was important for the vessel pressure to not exceed 3 atmospheres because its rupture pressure at room temperature is between 5 to 6 atmospheres and less at elevated temperatures. The temperature -

pressure relation for phosphorus was calculated using Antoine's equation (see Equation 3) which is in good agreement with experimental measurements done by Iseler *et al* (*48*) and Bachmann *et al* (*49*). The Antoine coefficients for phosphorus are A = 8.18302, B = 2718.69, and C = 81.7464. In addition, studies done by Bachmann *et al* (*49*) suggests that phosphorus sublimes as P_4 molecule from the 430°C zone, but dissociates to P_2 species at the 1150°C zone which creates a non-ideal behavior for phosphorus vapor (*49*). The plot of phosphorus vapor pressure as a function of temperature is shown in Figure 2-4.

$$Log(P) = A - \left(\frac{B}{T + C} \right) \qquad (3)$$

The solution temperature was held at 1150°C for an extra 28 hours and then was cooled to 1000°C at a rate of 3°C per an hour. The whole system was then quench cooled to room temperature. A few experiments were conducted at various soak times (0, 24, 36, and 52 hr.), and also dwell times (0, 52, 72, and 96 hr.) for different cooling rates (3, 10 and >500°C/hr.), as shown in Table 3-2 and Table 3-3.

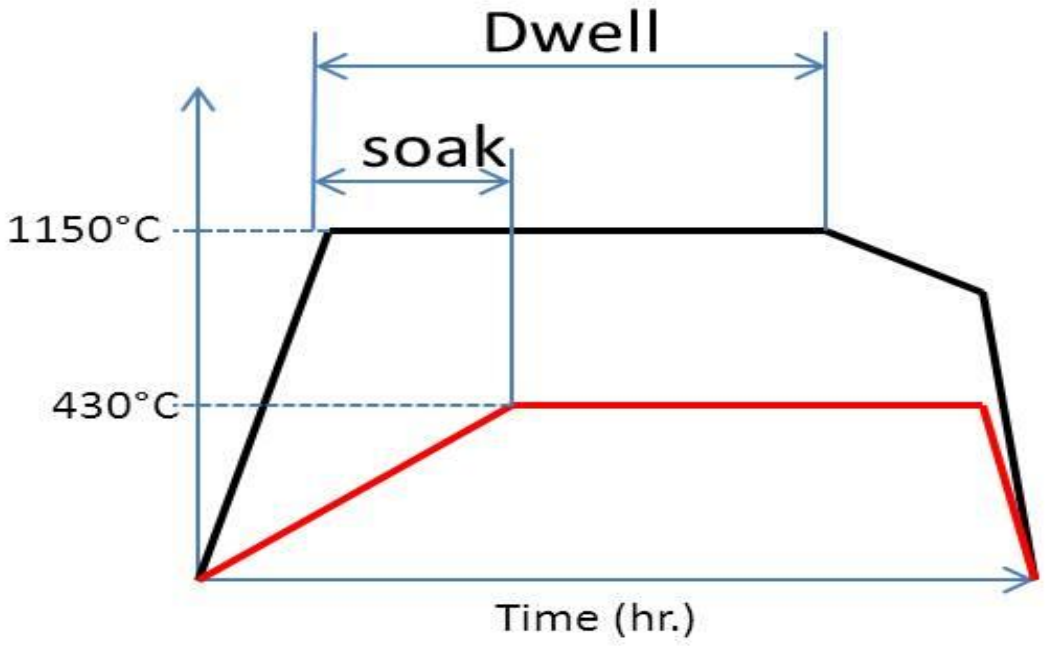

Figure 2-3: Temperature vs. time plot of the hot and cold zones explaining dwell and soak times.

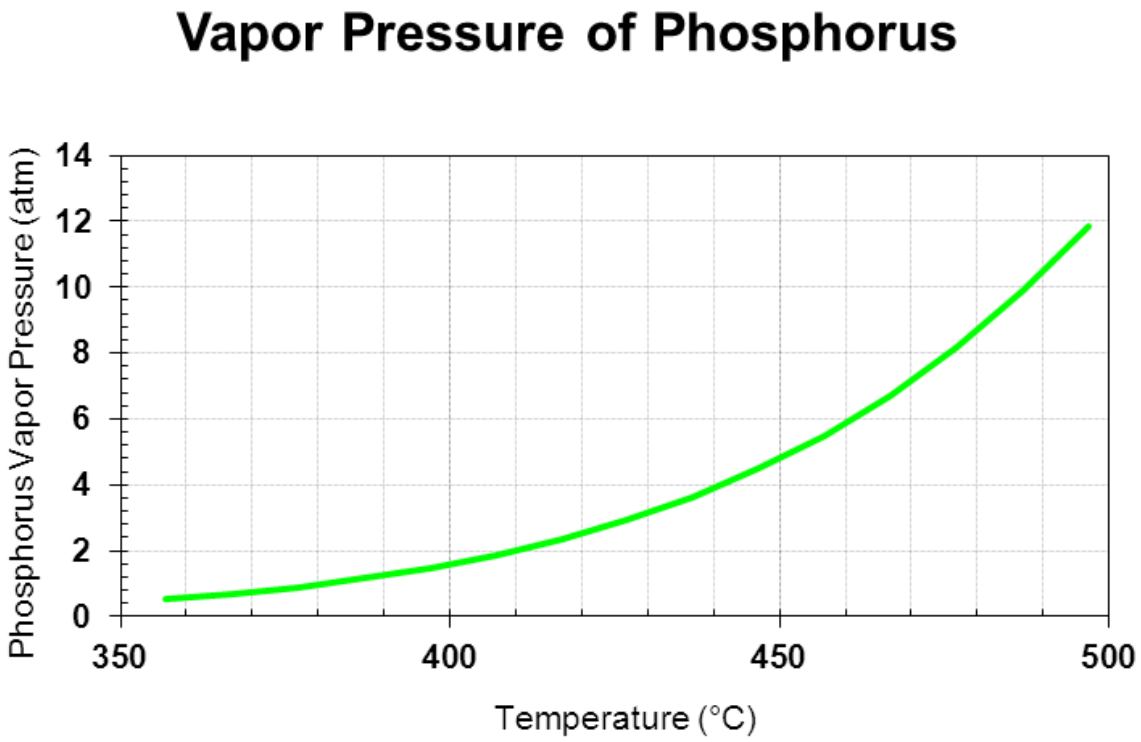

Figure 2-4: Calculated phosphorus vapor pressure as a function of temperature. Pressure of the system is controlled by phosphorus temperature.

After crystal growth, while equipped with appropriate PPE (face shield and thermal gloves) to prevent any incident from white phosphorus build-up in the quartz tube, the sample boat was carefully pulled out of the quartz tube. The nickel phosphide ingot imbedded with BP crystal, was etched in aqua regia (a mixture of nitric acid and hydrochloric acid, with a volumetric ratio of 1:3) overnight to remove the nickel phosphide away from the crystals at room temperature. The resulting crystals were then examined using optical microscopy, and characterized with defect selective etching (DSE), x-ray diffraction (XRD), Raman spectroscopy, photoluminescence, and energy dispersive spectrometer (EDS).

Materials

Both low and high purity source materials were used in our crystal growth experiments. The low purity source materials were used to establish the process and to study the growth rate and mechanism, while the high purity source materials were employed to grow higher purity crystals. Some information about the source materials is summarized in Table 2-1. The purities

quoted by the vendors are usually for metal basis only, and does not include the carbon or oxygen. Only Ceradyne provides isotopically pure boron; the other vendors sell only natural abundance boron (20% ^{10}B and 80% ^{11}B).

Table 2-1: Purity of source materials used for crystal growth.

Material	Purity %	Carbon/oxygen	Supplier	Form	Isotope
Boron	99	C→0.35% O_2→2.02%	Materion	powder	Natural abundance
Boron	97.79		Ceradyne	powder	Boron-10
Nickel	99.9	C→0.088% O_2→0.1%	Acros Organic	powder	Natural abundance
Phosphorus	99		Sigma Aldrich	powder	
Nickel	99.995		Materion	3x3 pellets	
Nickel	99.999	(C<100ppm)	Alfa-Aesar	powder	
Boron	99.9999 (UHP)	C→0.084% O_2→1.63%	Ceradyne	powder	Boron-11
phosphorus	99.9999		Acros Organic	chunks	

Boron and nickel source materials mixtures were contained with two different types of sample boats: pyrolytic boron nitride (PBN) and alumina sample boats are shown in Figure 2-7. These boats (both 10 cm long) contained fewer impurities and didn't impede the growth of crystals in anyway, or show signs of degradation or deformation during crystal growth. They were ideal for quality crystal growth.

Some information on additional equipment such as the furnace and the vacuum system utilized in this study is summarized in Table 2-2.

Table 2-2: Summary of equipment utilized during experiments.

materials		Base pressure	Max temperature	size	Note	Figure
Vacuum system	Edward roughing pump	10^{-3} torr			Equipped with thermocouple and ionic pressure gauges	Figure 2-1, Figure 2-6
	Varian turbo pump	10^{-6} torr				
Four zone Furnace	$MoSi_2$ heating elements (3 zones)	1 atm.	1550°C		Equipped with R-type thermocouples, and programmable controllers	Figure 2-5
	Resistance wire heating elements (1 zone)		1100°C			
Reactor	Quartz tube	5 atm. (rupture pressure)	1683°C (softening) 1215°C (annealing)	27 mm ID x 30 mm OD x 700 mm long	Fused at one end	Figure 2-1
Sample boats	Pyrolytic boron nitride (PBN)			10 cm long	PBN boats were most employed	Figure 2-7
	Alumina					

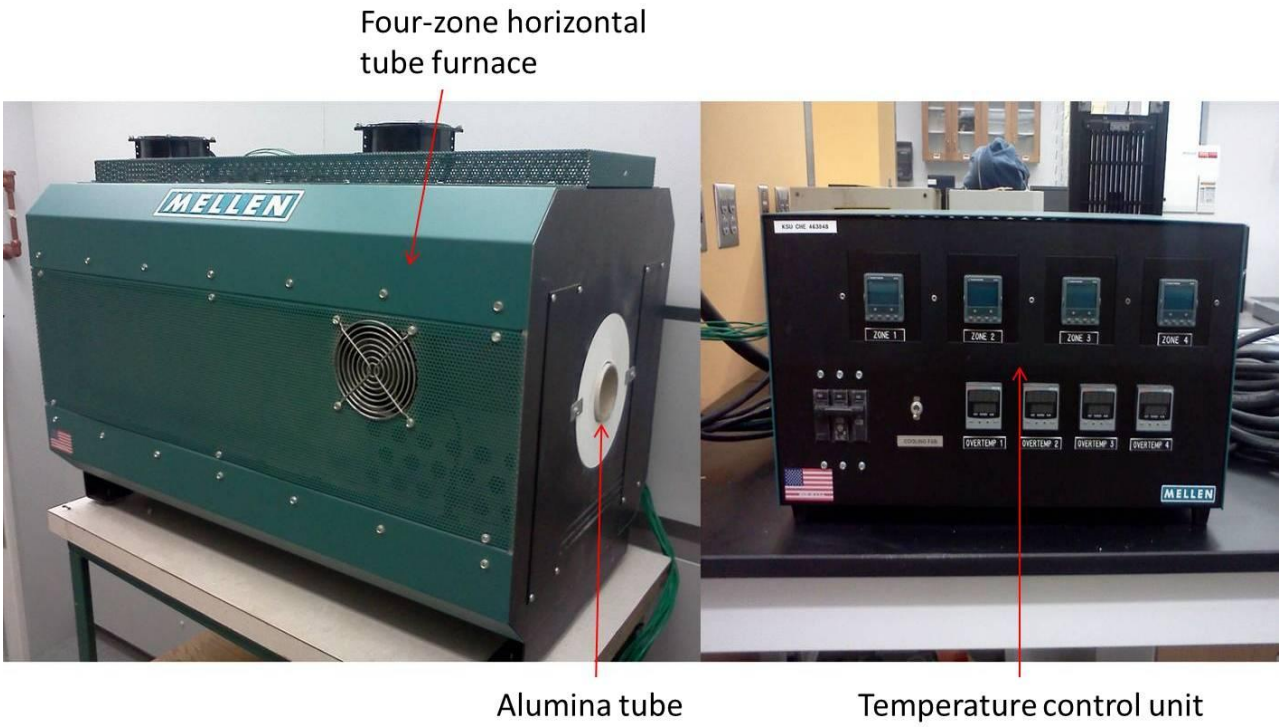

Figure 2-5: Photographs of the four-zone tube furnace and the controller used in the flux growth of BP crystals.

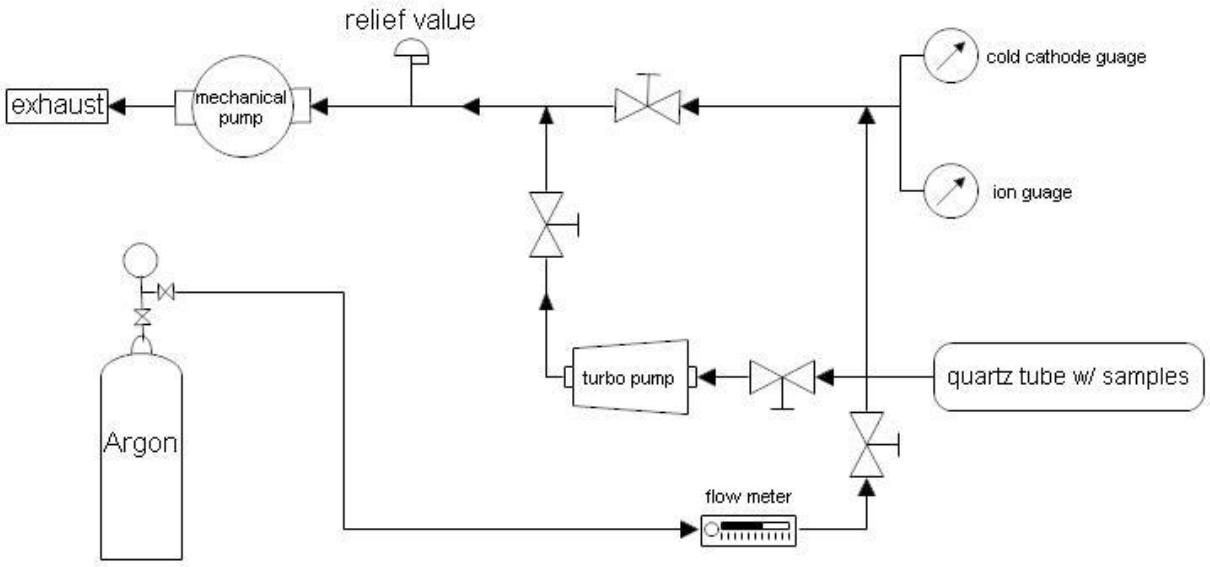

Figure 2-6: Schematic of the vacuum system used for evacuating the quartz tube.

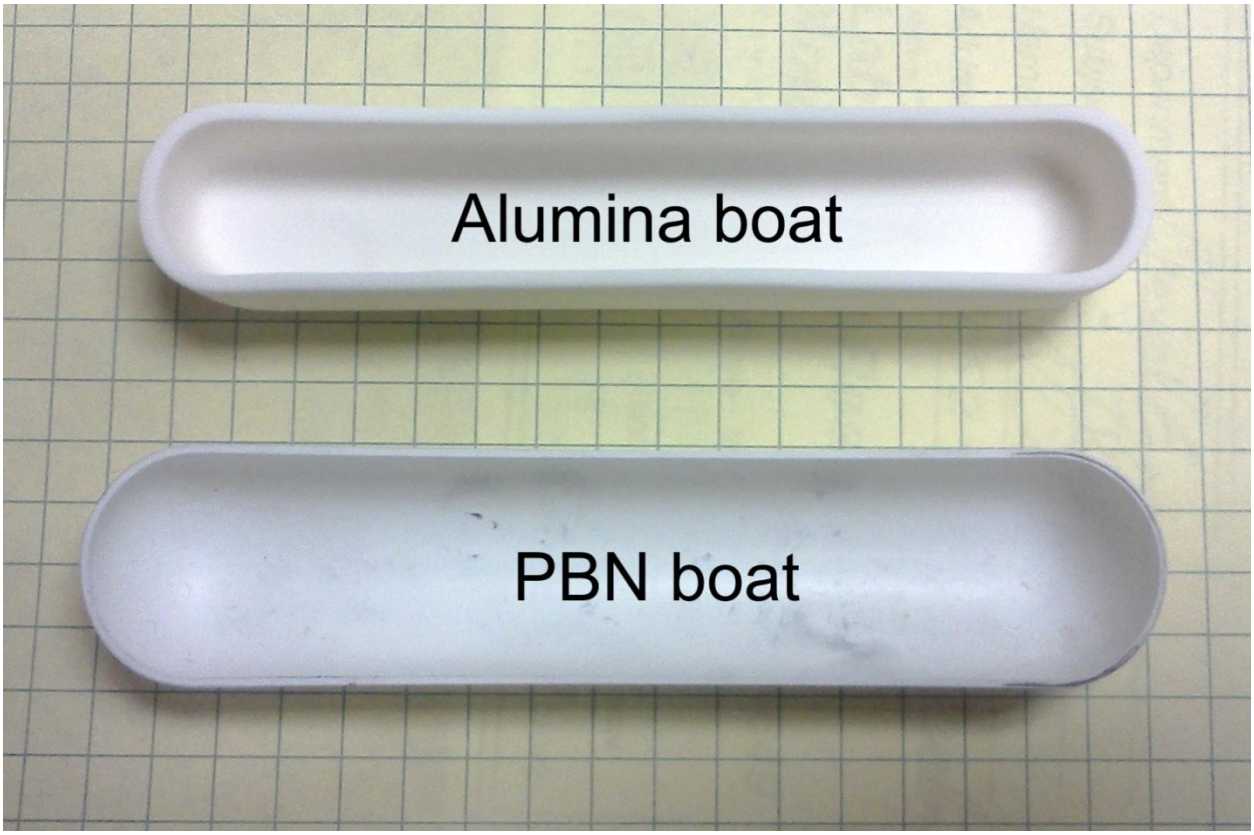

Figure 2-7: Photograph of the alumina and pBN sample boats used for crystal growth (each square is 0.25” x 0.25”).

Characterization of BP

The BP crystals were characterized by several analytical techniques. The surface morphology, elemental composition, and defects, were analyzed using optical microscopy, defect selective etching (DSE), scanning electron microscopy with energy-dispersive x-ray spectroscopy, x-ray diffraction, Raman spectroscopy, and photoluminescence spectroscopy. To successfully fabricate BP electronic devices, their electrical properties should be known. Therefore, current-voltage (IV), capacitance-voltage (CV), and Hall-effect measurements were employed to characterize the electrical properties.

Defect Selective Etching

Defect selective etching (DSE) of BP crystals was done to identify defects like edge and screw dislocations, and to estimate defect densities in the samples. In this technique, etch pits are formed on the crystal as a result of the etchant being more reactive at areas with defects or impurities. Thus DSE is useful for evaluating the crystal quality through measurement of etch pits per unit area.

BP is chemically inert to aqueous acid and alkalis, but can be preferentially etched by a molten mixture of KOH and NaOH to reveal defects (*28*). Molten KOH and NaOH have been successfully employed by many investigators to study III-V compound at various etching temperatures (*30, 40, 50–54*). In this study, etching experiments were done to determine the optimum temperature and time to reveal the defects on the grown BP crystals. BP crystals were submerged in a eutectic molten mixture of KOH and NaOH (~50 mol% each) with a melting point of 170°C contained in a vitreous carbon crucible. Crystal samples were first etched for one minute at temperatures ranging from 300 to 475°C, to determine the optimum etching temperature. Then a time evolution experiment was conducted at the optimum temperature of 325°C for times of 2 to 10 minutes. Samples were subsequently examined by optical and electron microscopies to determine etch pit sizes, shapes, and densities. The goal was to produce individual etch pits that did not merge together, and which could be readily seen with an optical microscope. Pit sizes 5-10 μm across were optimal.

Scanning Electron Microscopy/Energy-Dispersive X-ray Spectroscopy

A FEI Nova NanoSEM 430 with an energy-dispersive x-ray spectrometry (EDS) attachment was utilized to characterize the surface morphology of the cubic BP crystals, examine the etch pits produced by selective etching, and provided elemental mapping analysis.

SEM captures images by scanning the sample with focused electron beam and detecting the emitted secondary and reflected backscattered electrons. Primary electrons are emitted thermionically through an electron gun (field-emission gun) (*55*). When these incident electrons come in contact with sample surface, secondary electrons are emitted and are subsequently collected and analyzed by a detector. One of the commonly used detector is the Everhart-Thornley detectors (ETD) (*56*). Figure 2-8 shows features in a typical SEM system.

The samples also emit characteristic x-rays during electron beam bombardment. Since the emitted X-ray wavelengths are unique to each element, the x-ray detector in the attached EDS analyses the samples to create an elemental composition of the surface.

If the sample is electrically insulating, surface charging can occur repelling the incident electrons and degrading the image quality. Applying a conductive layer can reduce the surface charging. Since the SEM imaging and contrast depends mainly on the emitted secondary electrons, thin conductive layer (~1-2nm) of gold was sputtered on BP samples using a Hummer Sputtering system with a gold target.

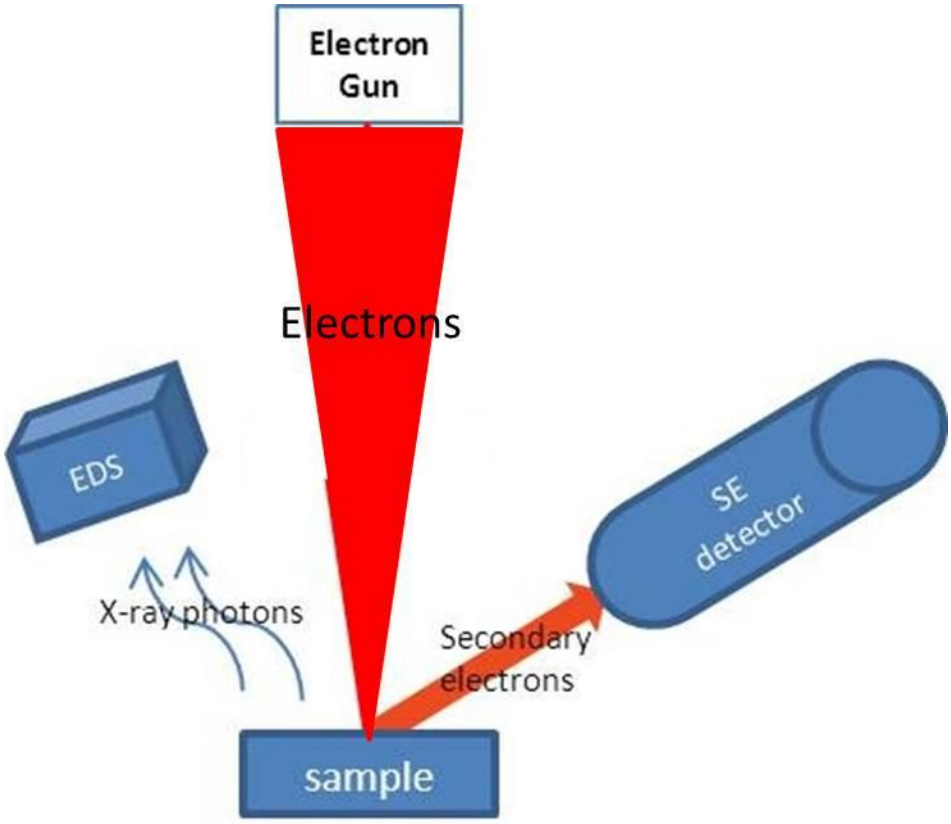

Figure 2-8: Depiction of typical SEM system. Primary electrons generated by the electron gun are incident on the sample, generating secondary electrons and x-rays. These signals are used to generate an image of the surface morphology and elementary composition.

X-ray Diffraction

The x-ray diffraction (XRD) patterns to study the preferred orientations of the produced crystals in this study were taken with a Rigaku MiniFlex II powder x-ray diffractometer which has a Cu Kα x-ray source (λ = 0.154056 nm). The patterns were then analyzed with PDXL XRD software to identify diffraction peaks.

XRD studies the atomic arrangements, preferred orientation, crystallographic planes and the lattice constant of a crystalline solid (*57*). An incident beam of x-rays is scattered by planes of atoms producing a diffracted x-ray beam. The atoms diffract the x-rays at an angle θ to the plane, as shown in Figure 2-9 where the horizontal lines represent crystal planes. The diffracted x-ray beams are then detected and counted. The equation known as Bragg's law, $n\lambda=2dsin\theta$ gives a relationship between the x-ray wavelength λ, inter-planar spacing d, the incident angle θ, and order of reflection n (1, 2, 3…). By scanning a sample over a range of incident angles, the diffracted x-rays are used to obtain the inter-planar spacings which are unique for every material.

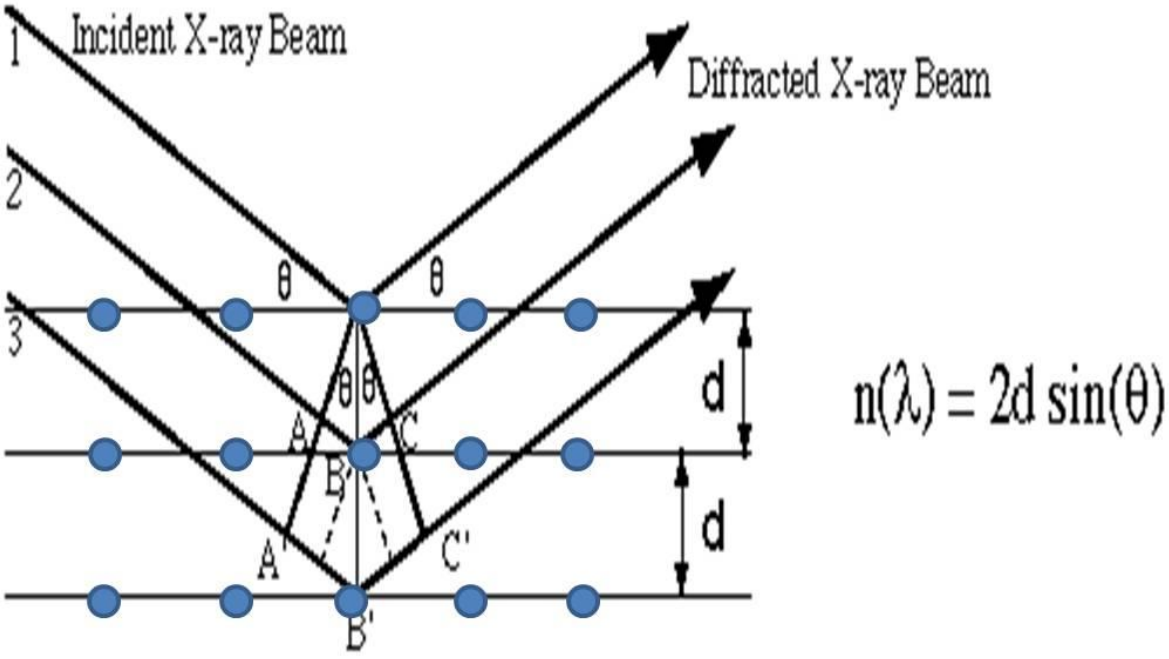

Figure 2-9: The Bragg diffraction condition for x-rays by crystal planes with incident angle-θ, the distance (d) between crystal planes is determined from Bragg's law.

Raman Spectroscopy

Raman spectroscopy is a non-destructive vibrational spectroscopic technique that can be employed to analyze organic and inorganic materials and measure the crystallinity of solids (*55*)(*58*). Raman spectroscopy relies on an intense monochromatic light source incident on a sample, which interacts with optical phonons on the sample's surface creating higher or lower photon energy shifts. This interaction is known as *Raman-shifted scattering*. The reflected scattered light and intensities of Raman-shifted wavelengths are easily detected and analyzed with a photo-detector to match known wavelengths for identification.

In this study, Martin Kuball's research group at the University of Bristol, United Kingdom, and Vikas Berry's research group at Kansas State University obtained Raman spectra. Table 2-3 summarizes some of the reported Raman shifts for BP from the literature. BP has been widely reported to have characteristic transverse optical (TO) phonon peak at 800cm^{-1} and a longitudinal optical (LO) phonon peak at 830cm^{-1}. The spectrum collected was then compared with the data presented in literature.

Table 2-3: Raman peak positions reported for BP

Raman shift, cm^{-1}		FWHM, cm^{-1}	Sample	Reference
TO	LO			
800	827	17	BP microcrystals (CSVT)	(*13*)
806	-	200	Amorphous BP films	(*22*)
- -	828.6 846.2	- -	Natural BP Isotope BP	(*32*)
799	828.9	10	BP platelets	(*59*)

Electrical Characterization

For useful electronic devices to be fabricated from BP crystals, it is important to understand its electrical characteristics and operating parameters such as charge mobility, resistivity, conductivity type, and majority carrier concentration. There are various techniques available to study the electrical characteristics of semiconducting materials like current –voltage (I-V) measurement, capacitance-voltage (C-V), and Hall effect measurements, and deep level

transient spectroscopy (DLTS), to determine the resistivity, carrier concentration, threshold voltage, breakdown voltage, built-in potential, mobility, contact resistance, barrier height, dielectric constant, depletion width, interface states, carrier lifetimes, and deep level impurities of a semiconductor. To exploit these electrical properties, the semiconductor material can be made into simple devices like Schottky barrier diode and/or ohmic device. Schematic diagrams of such devices are shown in Figure 2-10.

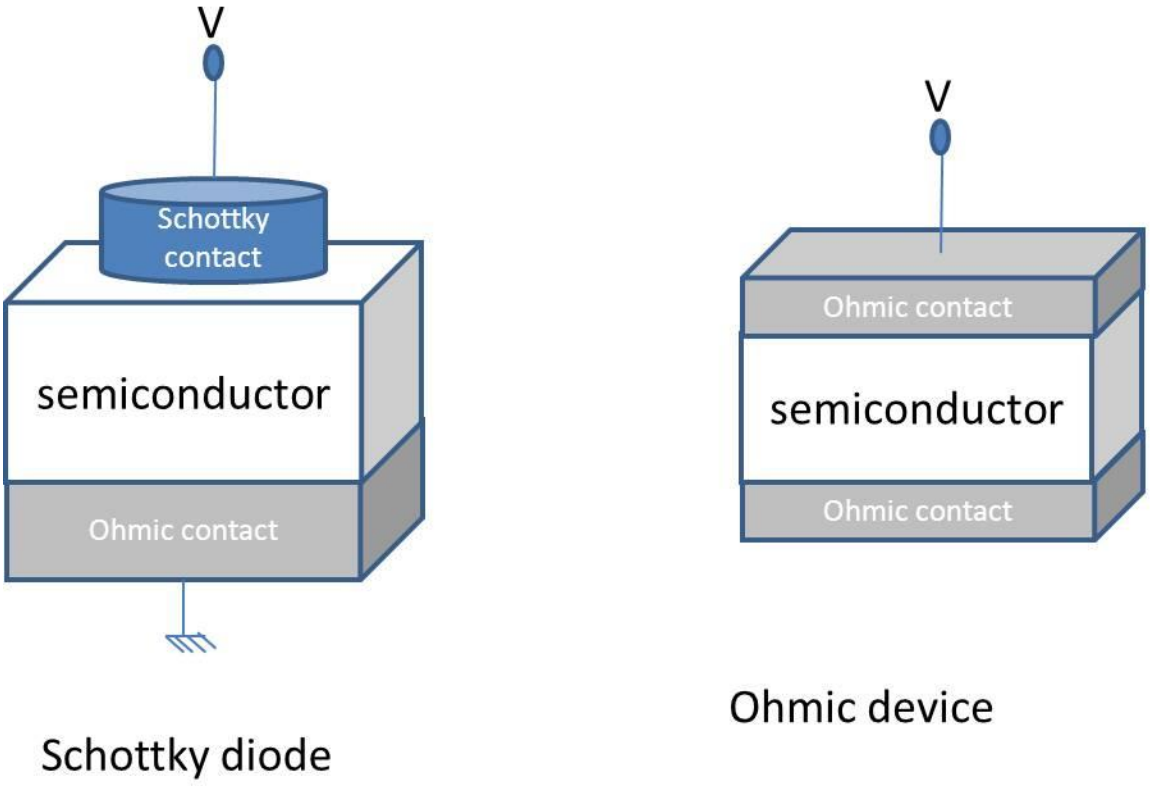

Figure 2-10: Perspective view of a Schottky diode and an ohmic device. In this study, Schottky barrier contacts were made with gold (Au) while ohmic (linear) contacts were made using aluminum (Al).

Making these devices requires the formation of Schottky barriers and ohmic contacts on the surface of the BP crystals. In this study, Schottky barrier (rectifying) contacts were made with gold (Au), and aluminum (Al) as the ohmic contact (non-rectifying). The BP Schottky diodes and ohmic devices were characterized using I-V, C-V, and Hall-effect measurements.

1.2 mm^2 ohmic contacts for both the Schottky diodes and the ohmic devices were made by sputtering 5000Å thick aluminum on clean surfaces of BP crystals, and then annealing in

vacuum with a rapid thermal annealing system (RTA) at 400ºC for 1min. The annealing diffuses some of the aluminum into the BP crystal which promotes low resistance between the metal layer and the crystal (*60*). 1 mm^2 Schottky barriers were made by sputtering 5000Å thick Au on top surface of the crystals through a Si wafer shadow mask. These metals were deposited using a Perkin-Elmer plasma sputter system model 4400 equipped with Au and Al targets. All contacts made were courtesy of researchers at LLNL. Devices were mounted on a header and wire bounded to the external package connectors. A packaged Schottky diode is shown in Figure 2-11.

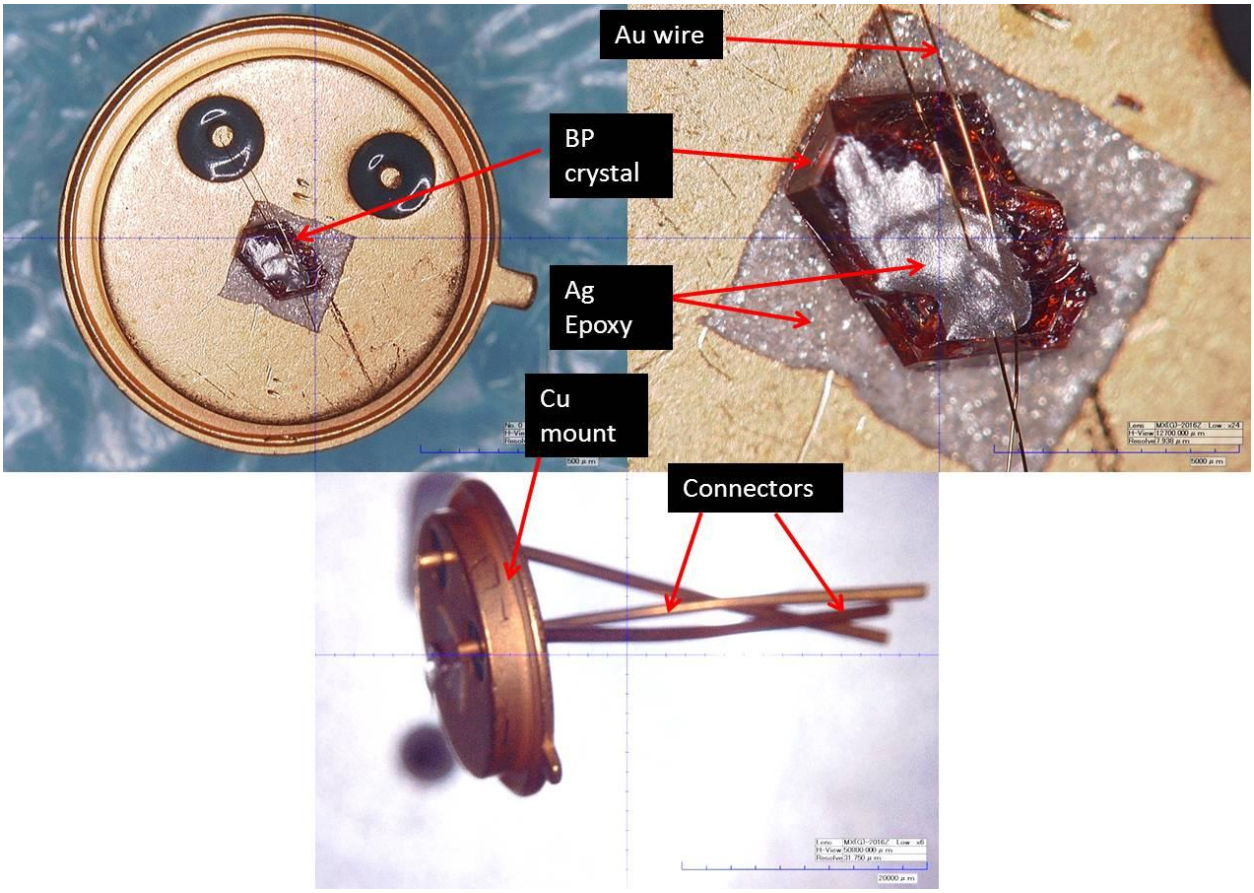

Figure 2-11: Packaged diode with Au contact faced down against Ag epoxy tape. Wire contacts on the Au & Al contacts were made with Ag epoxy and 0.001" Au wire

I-V measurements on both the Schottky diodes and ohmic devices, and C-V measurements on just the Schottky diodes were done using a KEITHELY Model 4200-SCS semiconductor characterization system. I-V measurement is typically a plot of electrical current through a device with a corresponding voltage bias across it. This shows how a device would

behave as a circuit. I-V plot obtained from the Schottky barrier diodes were used to extract the ideality factor η, leakage current, and turn-on voltage. Figure 2-12 shows mock I-V characteristics plots of a Schottky diode indicating where to extract information. The ideality factor η can be obtained from the slope of the semi-log I-V plot by applying equation (4):

$$\eta = \left(\frac{q * dV}{kT * d\ln(I)} \right) \qquad (4),$$

where q is the elementary charge = 1.602 x 10^{-19} C, k is the Boltzmann constant = 1.38 x 10^{-23} J/K, T is the absolute temperature in Kelvin, V is the bias voltage in volts, and I is the current across the diode in amps.

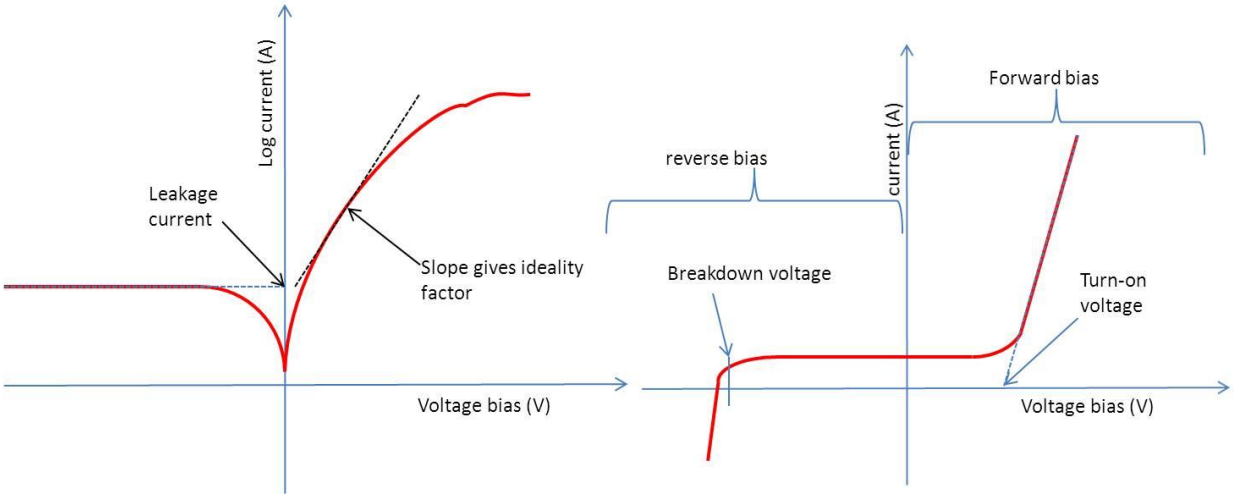

Figure 2-12: Semi-log and direct I-V characteristics of a Schottky diode.

I-V measurement on an ohmic device (resistor) should display a linear increase in current for all voltages across it. In other words, the resistance is totally independent of the polarity or magnitude of the applied voltage bias (*60*). The plot of the voltage bias against the current flow through an ohmic device will produce a straight line, as shown in Figure 2-13. The slope of the linear I-V plot was equal to the total resistance R_T of the ohmic device in ohms (Ω), which also is the sum of the two contact resistances R_c and the sheet resistance R_s, i.e. $R_T = R_s + 2R_c$. The sheet resistivity of the semiconductor, ρ_{sh}, was also calculated by measuring the resistance as the distance between contacts varies, as illustrated in Figure 2-14.

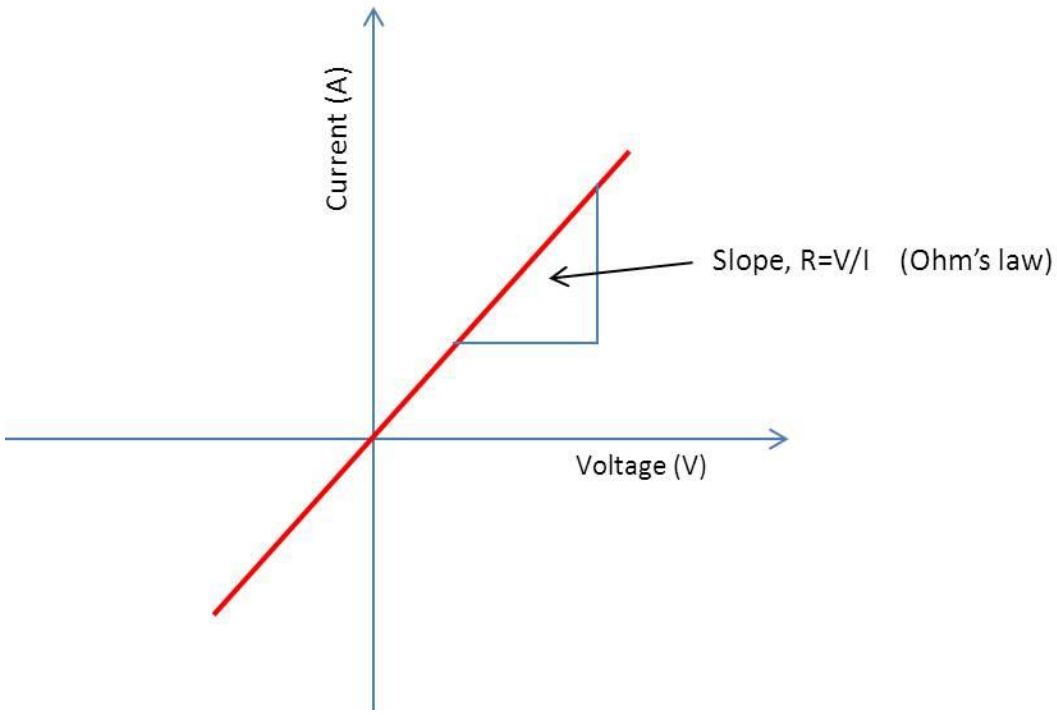

Figure 2-13: I-V characteristics of an Ohmic device. The slope is equal to the total resistance (R_T) of the material.

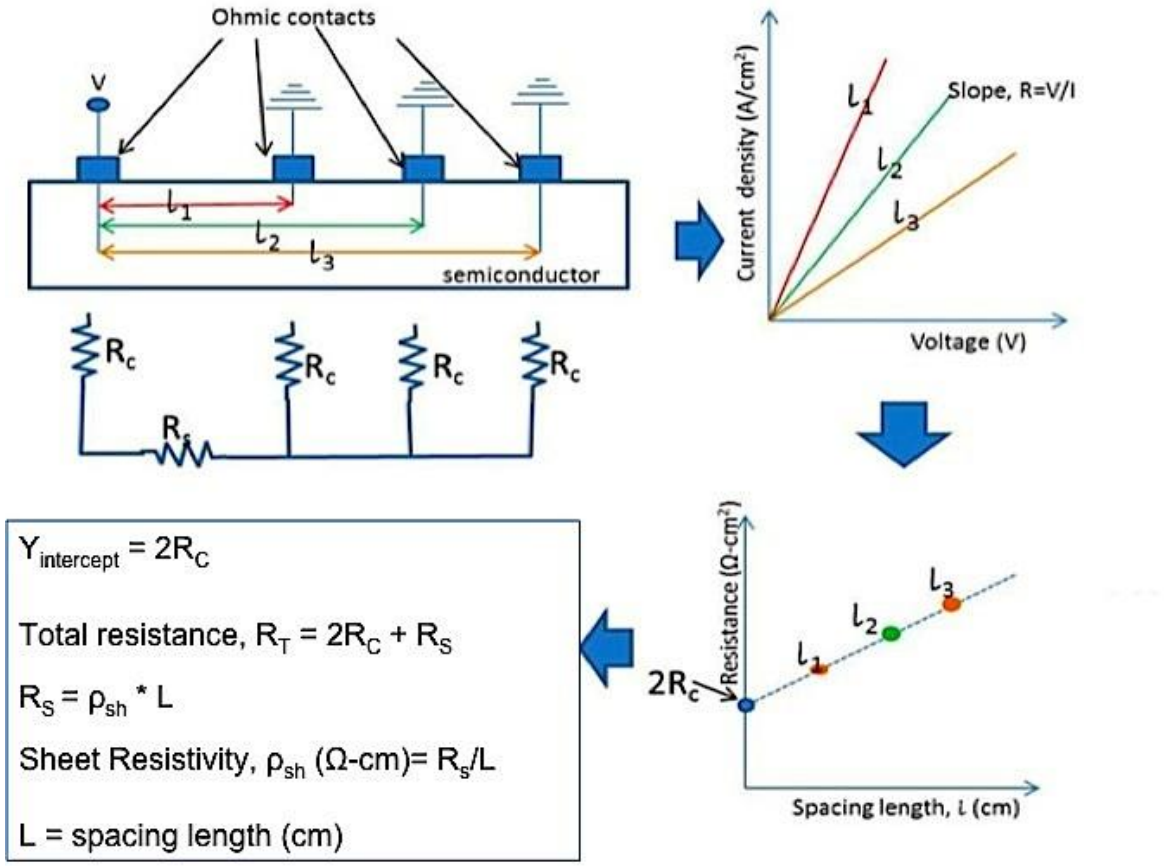

Figure 2-14: Steps necessary to calculate the sheet resistivity, ρ_{sh}.

The majority charge carrier concentration, NB, built-in potential V_{bi}, and dielectric constant εBP, were revealed from the C-V measurements (*60*). The capacitance of an Au-BP Schottky diode was measured as a function of applied voltage at room temperature. Using the capacitance versus voltage plot, the dielectric constant of BP was calculated from the maximum capacitance per unit area using equation (5).

$$C_{\max} = \frac{\varepsilon_o \varepsilon_{BP}}{W} \qquad (5)$$

Where C_{max} is the maximum capacitance per unit area (F/cm^2), ε_o is vacuum permittivity = 8.854 x 10^{-14} F/cm, W is the semiconductor width, and ε_{BP} is the dielectric constant of BP. A linear plot was obtained from the C^{-2} versus applied voltage plot, where the intercept at $C^{-2} = 0$ corresponds to the built-in potential of the Au-BP Schottky diode. The slope of the linear plot

was applied to the equation (6) to obtain the majority charge carrier concentration N_B, which is assumed to be constant.

$$N_B = \frac{2}{q\varepsilon_o\varepsilon_{BP}}\left[\frac{-1}{d\left(1/C^2\right)/dV}\right] \qquad (6)$$

One of the most important parameter of a semiconductor is the charge mobility μ. It describes how strongly the motion of an electron is influenced by an applied electric field (*60*). Mobility μ, along with resistivity ρ, and charge carrier concentration can accurately be determined using the Hall effect measurement. The Hall effect measurement involves studying the transport of free carriers in a semiconductor while applying a voltage bias as well as a magnetic field (*61*). Figure 2-15 depicts the Hall effect setup where a constant current *I* flows along the x-axis in the presence of a magnetic field applied in the z-direction. Mobile electrons or holes in the semiconductor drift away from the current direction toward the y-axis, resulting in an excess surface electrical charge on this side of the semiconductor. This charge results in the Hall voltage, a potential drop across the two sides of the sample (*62*).

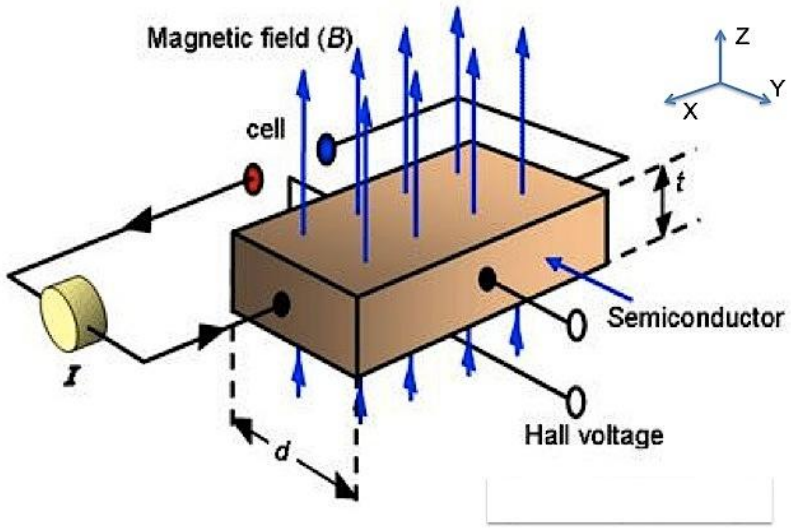

Figure 2-15: Hall effect schematic diagram of the applied voltage and magnetic field, and the generated electric field (Hall voltage).

To determine the mobility μ of a semiconductor, the Hall voltage VH needs to be measured from known values of current I, magnetic field B, and q ($1.6*10^{-19}$C) which are used to calculate the sheet density n_s of charge carriers in the semiconductor using $n_s = IB/q|V_H|$ (*62*). A

negative Hall voltage implies that the majority charge carriers are electrons while a positive measurement suggests holes are the majority carriers. The sheet resistance R_s is determined using the Van der Pauw technique. Van der Pauw showed that two resistances R_A and R_B corresponding to two terminals shown in Figure 2-16, are related to the sheet resistance R_s through the equation (7). R_A and R_B are obtained using equation (8).

$$e^{\frac{-pR_A}{R_s}} + e^{\frac{-pR_B}{R_s}} = 1 \tag{7}$$

$$R_A = \frac{V_{43}}{I_{12}}, R_B = \frac{V_{14}}{I_{23}} \tag{8}$$

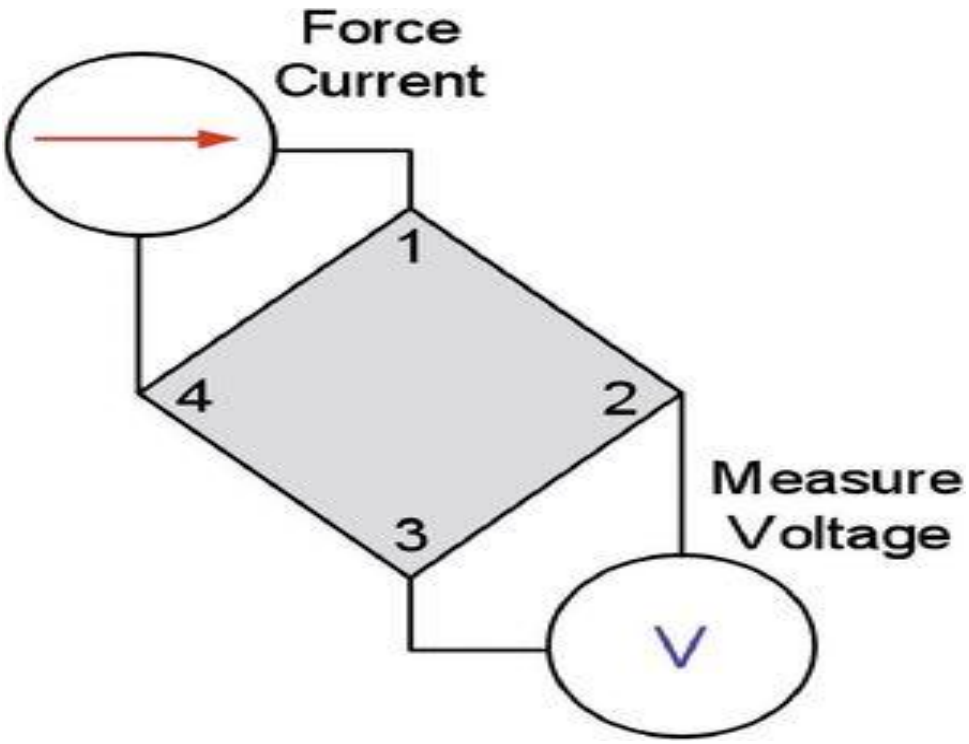

Figure 2-16: Van der Pauw technique for obtaining sheet resistance R_s.

Once the sheet resistance R_s is calculated, the mobility μ can then be determined using the equation (9).

$$\mu = \frac{|V_H|}{R_s IB} = \frac{1}{qn_s R_s} \tag{9}$$

The Hall effect measurements in this study were done on a BP crystal using a Lakeshore Hall effect measuring system. The BP crystal used had an array of ohmic square contacts made by first depositing a 10nm adhesive layer of chromium, and then a 200nm layer of gold through a

TEM grid shadow mask using E-beam deposition courtesy of researchers at NIST (shown in Figure 2-17). The measurement on the BP crystal provided much needed mobility, carrier type, and sheet resistance of the synthesized BP.

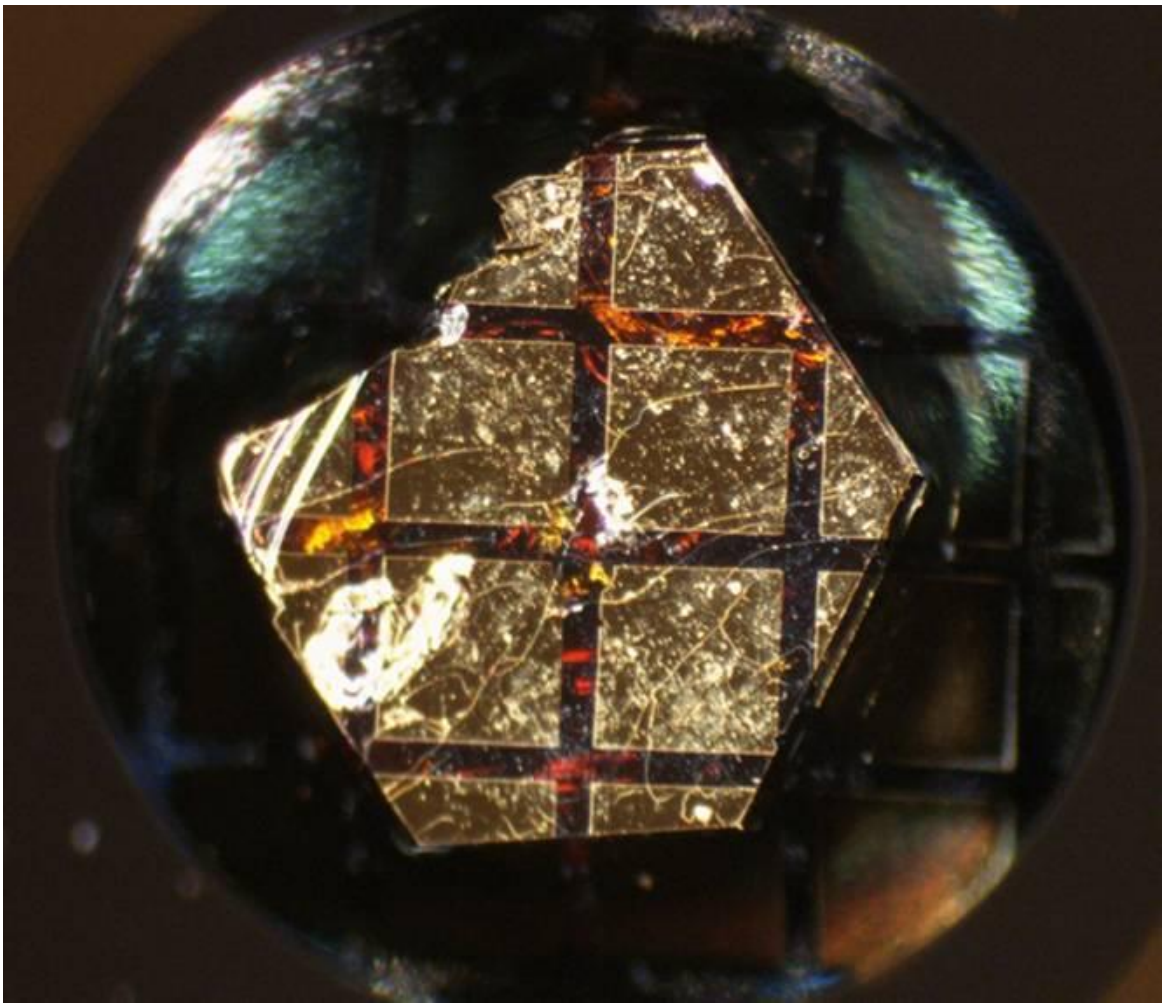

Figure 2-17: BP crystal with an array of Cr-Au ohmic contacts

Chapter 3 - Results and Discussion

Crystal Growth Analysis

Red, transparent and mostly hexagonal-shaped BP crystals were obtained in this study. The crystals were randomly distributed throughout the ingot, and sometimes formed in geodes surrounded by a Ni_5P_4 shell as shown in Figure 3-1. The crystals varied in size and morphology. The specific cooling rate did have an impact on the distribution, morphology and size. Experimental factors that affect the growth of BP crystals are presented in the following sections.

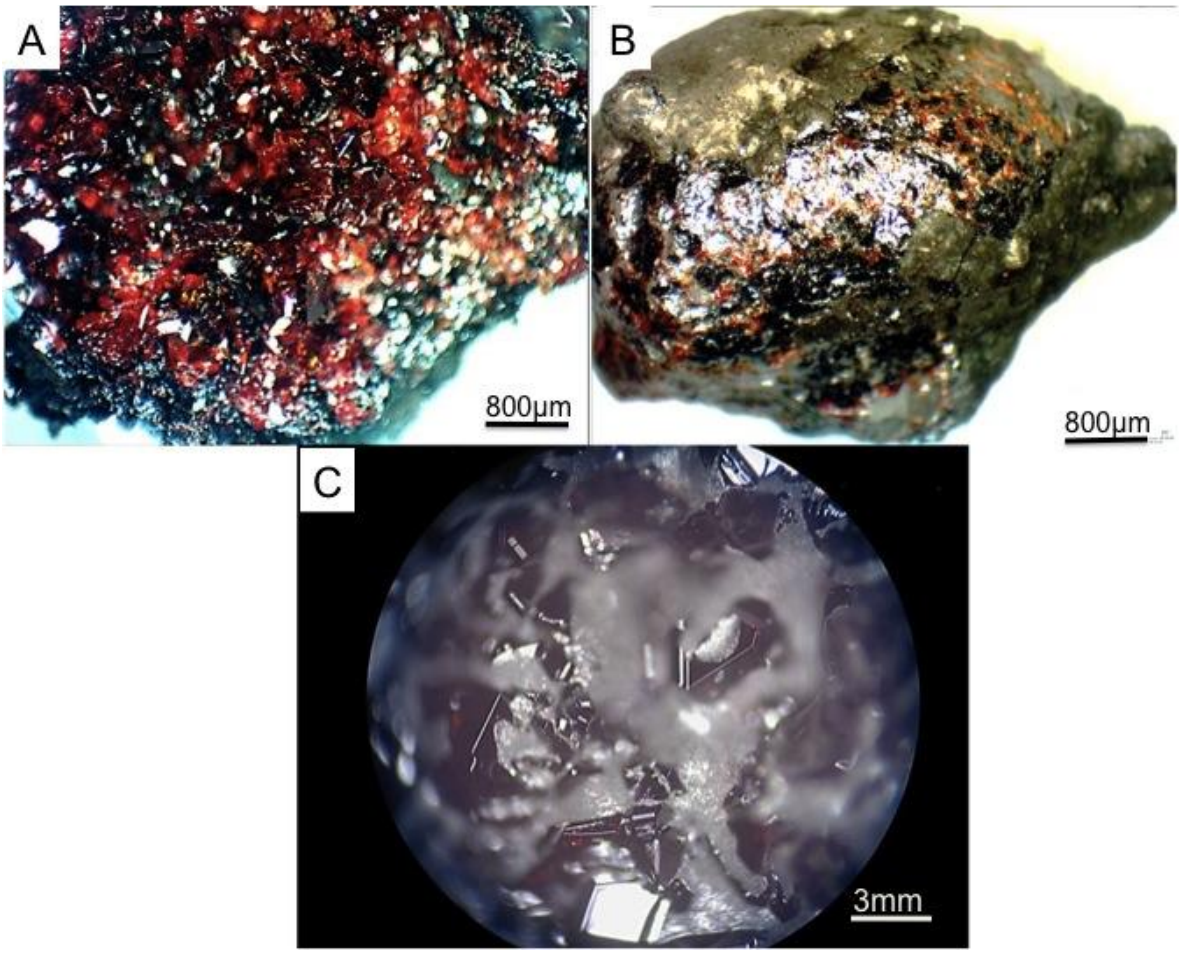

Figure 3-1: (A) Interior of a geode shell containing many BP crystals; (B) Outside shell of the geode; (C) BP crystals imbedded in nickel ingot

Boron-Nickel-Phosphorus Composition

Experiments were conducted with several boron, nickel, and phosphorus compositions. Although nickel and boron powder were mixed in amounts to produce a eutectic composition of 55 mol. % of nickel and 45 mol.% of boron, typically a quarter of the boron powder didn't dissolved. It remained as powder that was separated from the ingot (see Figure 3-2). If the B-Ni solution contains less than 55 mol. % of nickel, some of the boron reacts with the nickel and phosphorus but most of the boron was unchanged (see Figure 3-3). A homogenous mixture is achieved when 45 mol. % of boron in nickel is reacted with phosphorus (shown in Figure 3-4), which is the eutectic composition for B-Ni binary system (*63*).

When there was insufficient phosphorus (less than 49 mol. %) in the tube, black crystals (shown in Figure 3-5) formed with a few red crystals. In this case, the dissolved boron is deprived of phosphorus from the formation of nickel phosphides. The formed crystals and the nickel ingot were analyzed with XRD. The XRD patterns in Figure 3-7 prove that Ni_5P_4 and $B_{12}P_2$ were formed in these instances. 49 mol. % of phosphorus is required for the formation of stoichiometric BP and Ni_5P_4. Experiments conducted with the appropriate composition (2:3:5 mol ratio of B: Ni: P) produced red and transparent BP crystals as shown in Figure 3-6. The XRD pattern of the red crystals obtained (shown in Figure 3-8) matched that reported for BP [peak from (111), (200), (220), (311), and (222) planes] consistent with those reported in literatures (*12, 22, 38, 45, 64*). The preferred orientation of the BP crystals was the (111) plane, which has a peak FWHM of 0.275° demonstrating its high crystallinity.

The SEM image with EDS mapping of a BP crystal as shown in Figure 3-9, shows the morphology of this 1.5 mm single crystal contained flat facets. The EDS compositional analysis of a BP crystal was 74 wt% (49.8 at %) for phosphorus and 26-wt% (50.1 at %) for boron, demonstrating the stoichiometry of boron to phosphorus has a 1:1 ratio.

The black and red crystals were compared using Raman spectroscopy. Figure 3-10 shows the Raman peaks of a BP crystal compared to the crystal in Figure 3-5A incorporated with $B_{12}P_2$. These Raman spectra of BP, done by Vikas Berry's group at KSU, shows a convoluted shift at 833 cm^{-1} which is a combination of the characteristic transverse optical (TO) and longitudinal optical (LO) phonon peaks known to be at 800 cm^{-1} and 830 cm^{-1}, respectively (*13*). The $B_{12}P_2$ spectra had peaks that corresponds to the characteristic peaks reported in literature (*65, 66*). Another Raman spectra of BP in Figure 3-11, done by Martin Kuball's group at University of

Bristol, illustrates the not-convoluted Raman peaks of a BP crystal with the TO peak at 800 cm^{-1} and LO peak at 830 cm^{-1}. The FWHM of the LO peak is 4 cm^{-1} showing the high-ordered crystallinity of the produced crystals.

Table 3-1 summaries the results obtained from various reactant compositions.

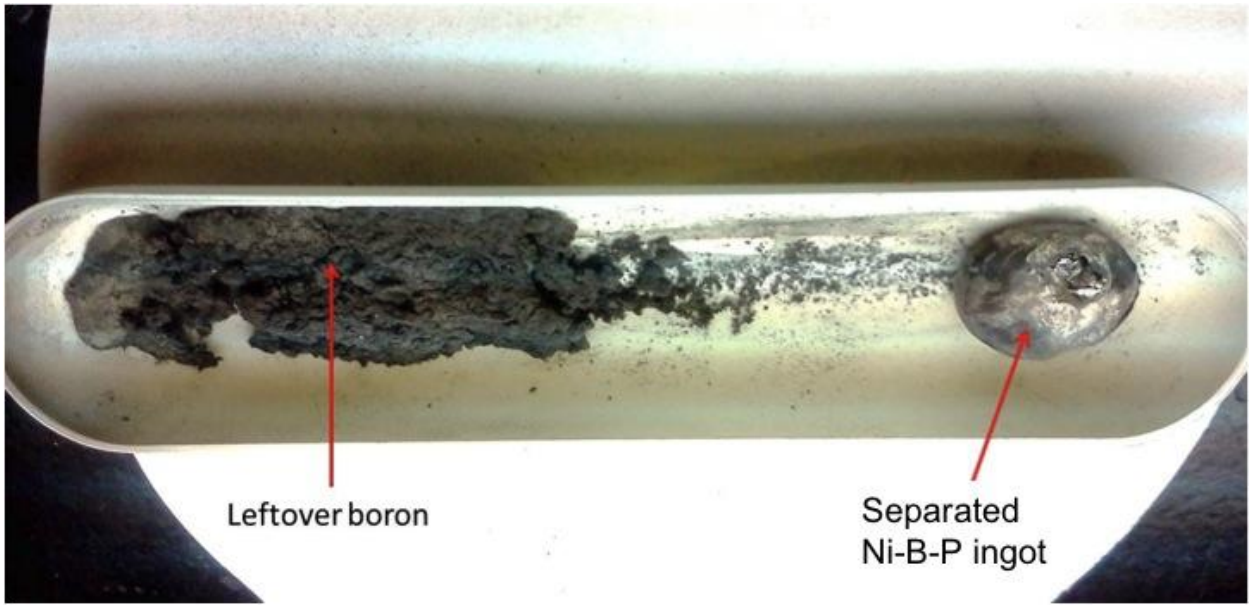

Figure 3-2: An experiment with 3:5:2 mole ratios of boron, nickel and phosphorus, respectively, with soak time of 36hr, dwell temperature of 1150°C, and cooling rate of 3°C/hr. The ingot containing relatively high amount of nickel easily separated from the boron.

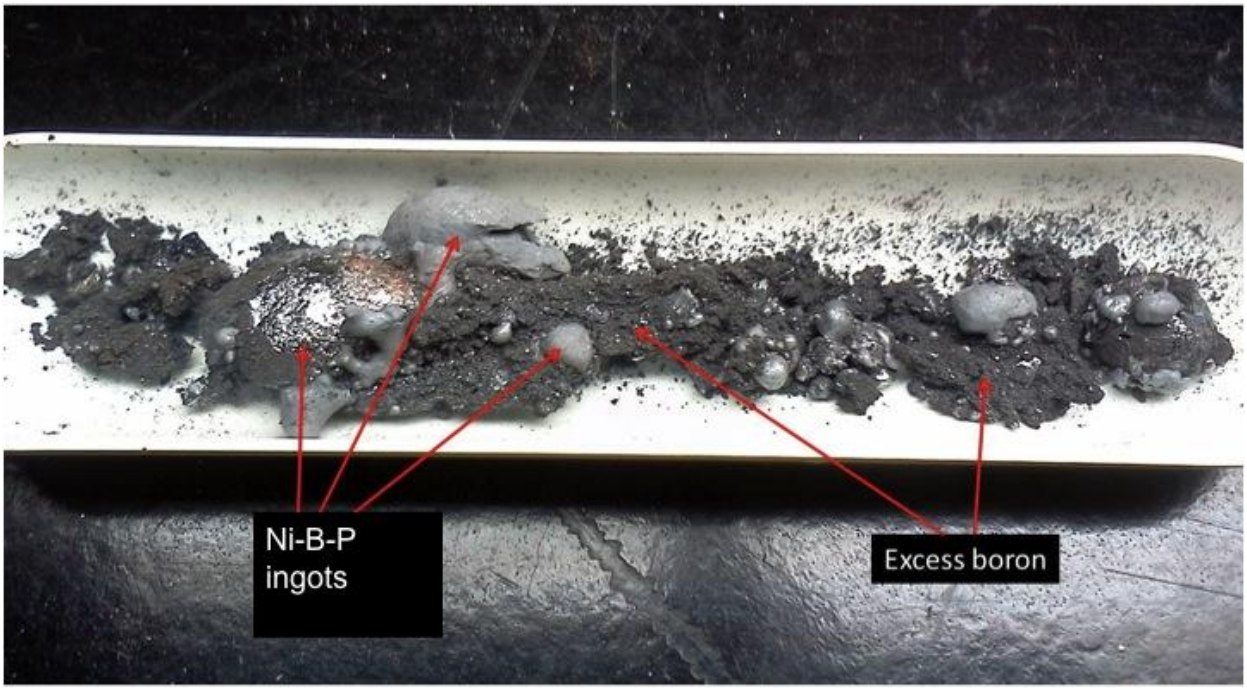

Figure 3-3: An experiment with 3:3:4 mole ratios of boron, nickel and phosphorus, respectively, with soak time of 36hr, dwell temperature of 1150°C, and cooling rate of 3°C/hr. Some boron powder didn't react with nickel and phosphorus.

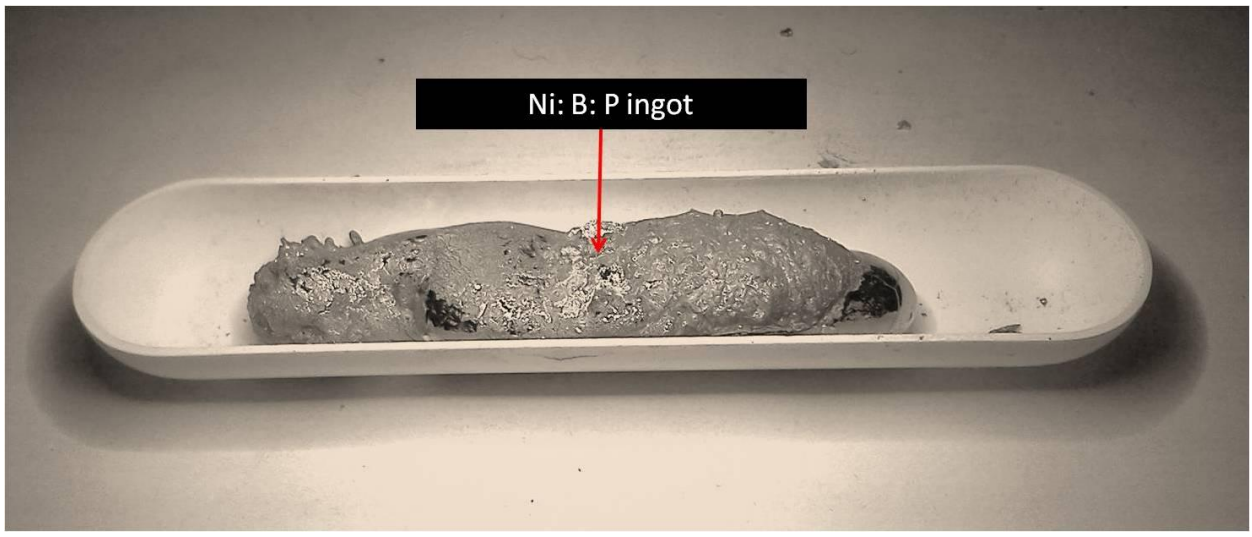

Figure 3-4: An experiment with 3:4:3 mole ratios of boron, nickel and phosphorus, respectively, with soak time of 36hr, dwell temperature of 1150°C, and cooling rate of 3°C/hr. Boron completely reacted with nickel and phosphorus.

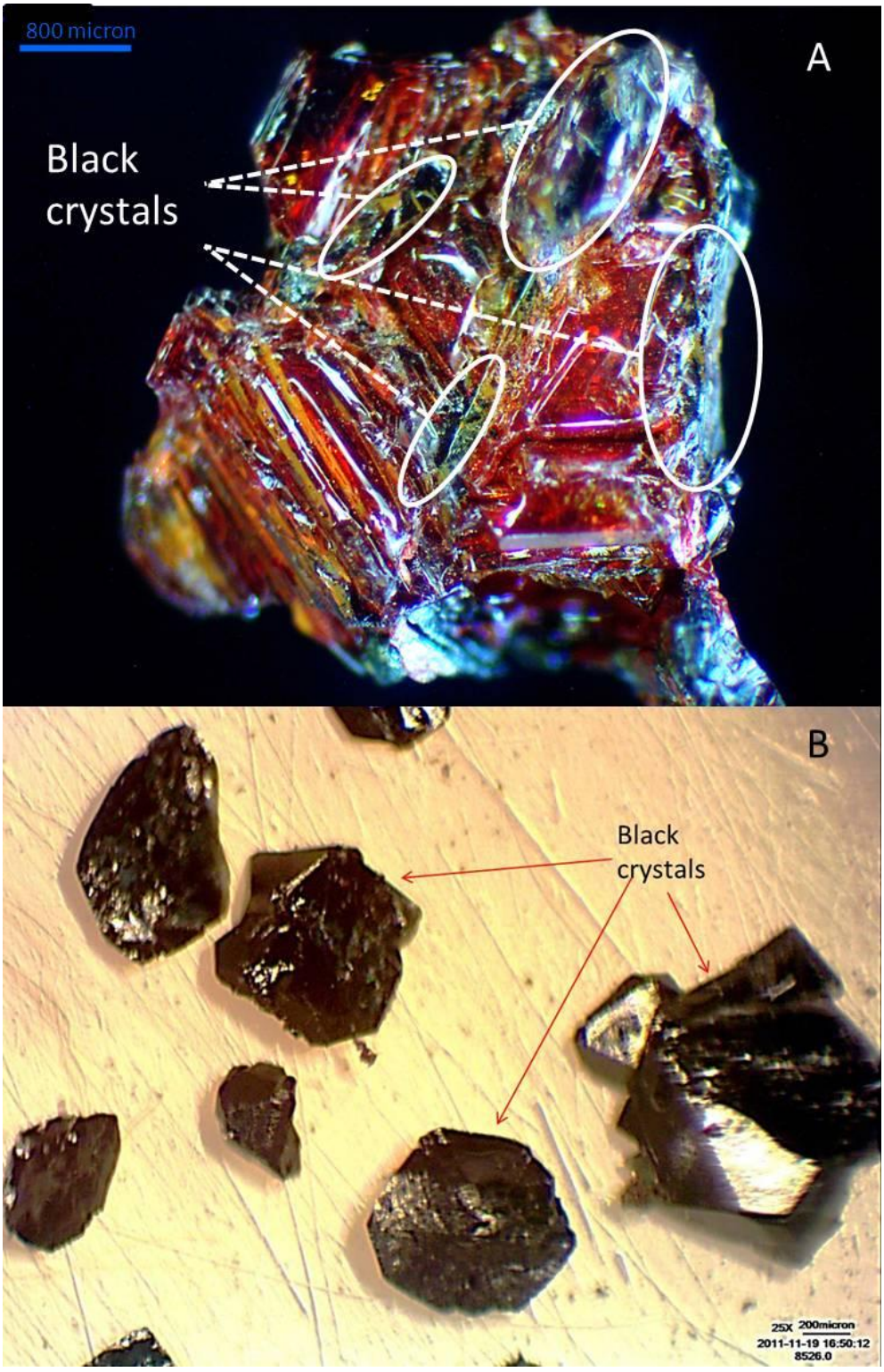

Figure 3-5: (A) black crystals incorporated in BP crystal. (B) Black crystals formed where there was insufficient phosphorus. Subsequent XRD and Raman spectroscopy demonstrated these were $B_{12}P_2$ crystals.

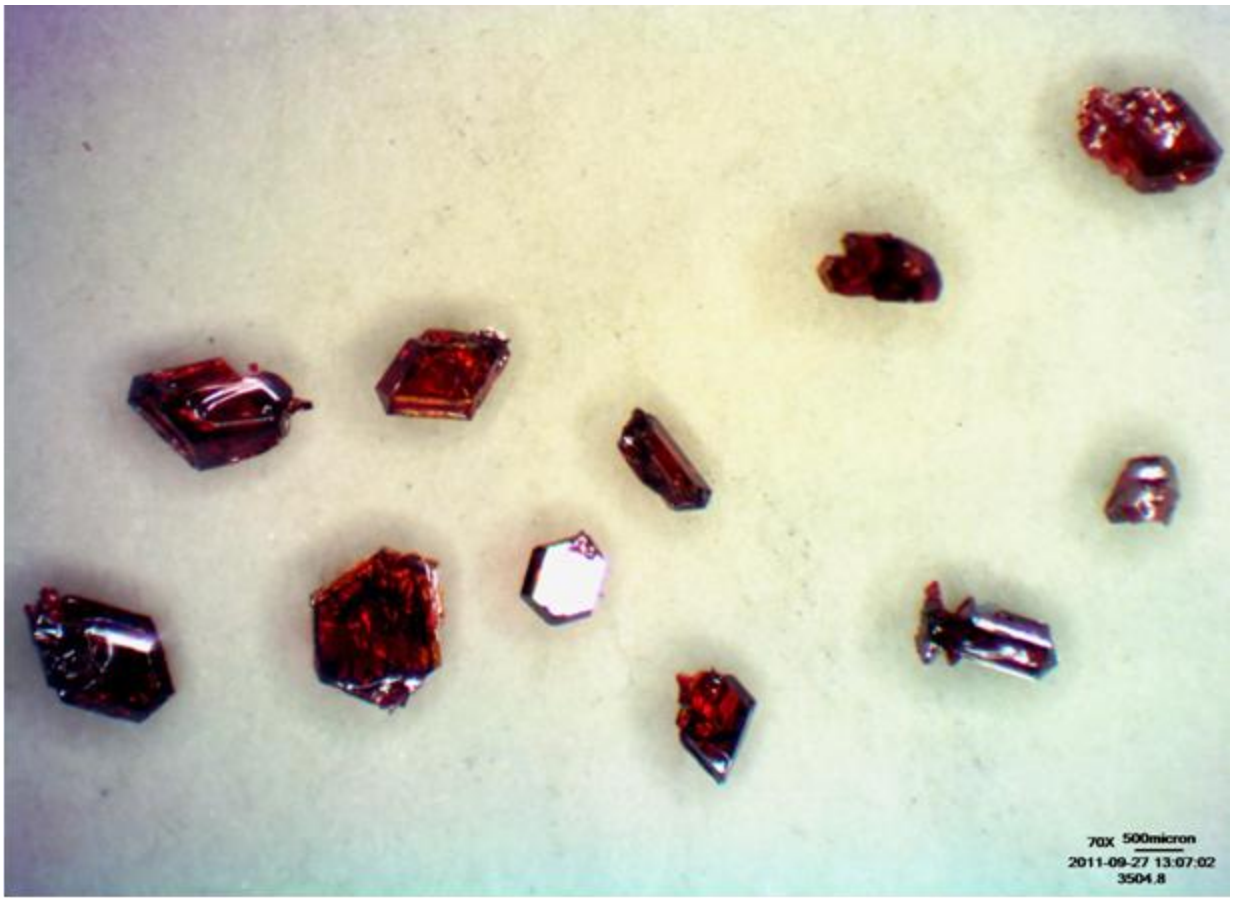

Figure 3-6: BP crystals formed with 2:3:5 mol ratio of B: Ni: P at dwell temperature of 1150°C, dwell time of 72hr, soak time of 12hr, and cooling rate of 3°C/hr.

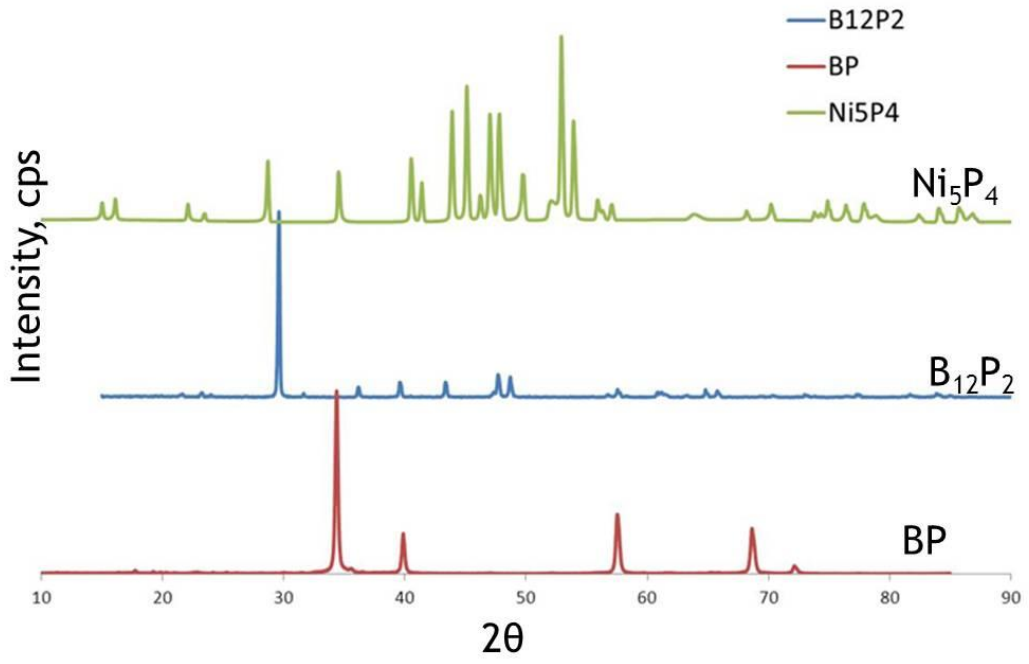

Figure 3-7: XRD patterns comparing products from an experiment where dissolved boron is deprived of phosphorus from the formation of nickel phosphides. Top two patterns show the formation of nickel phosphide and icosahedral boron phosphide (black crystals).

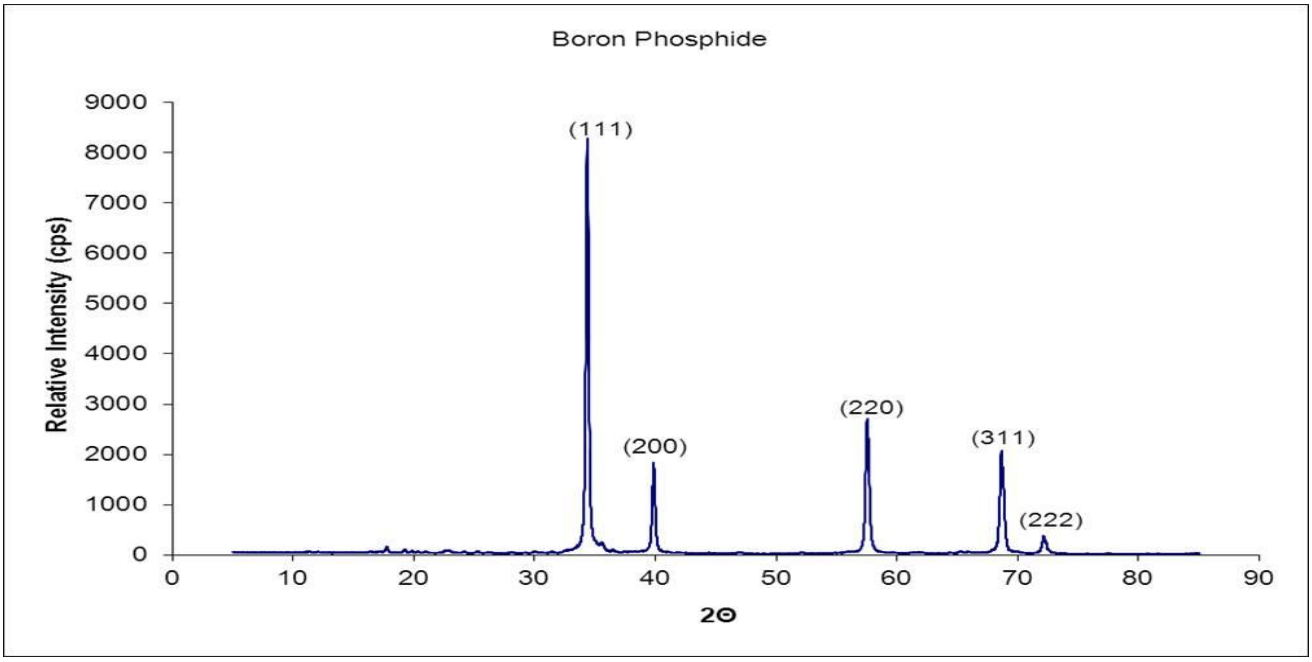

Figure 3-8: A characteristic XRD pattern from a BP crystal. The crystal planes associated with each peak are labeled.

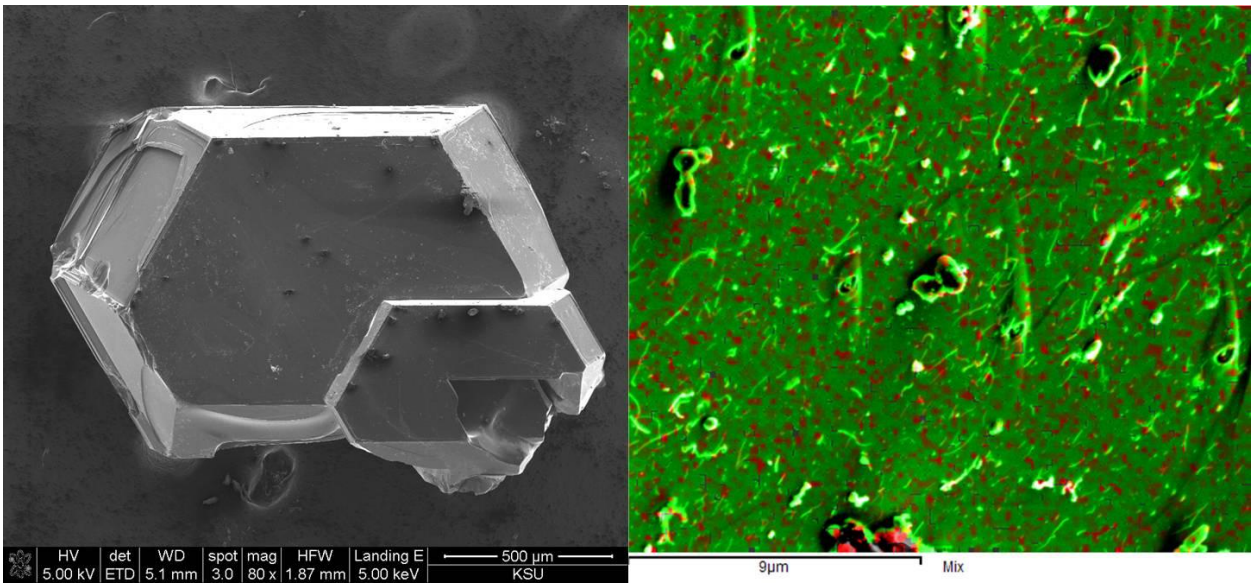

Figure 3-9: (left) SEM images of a 1.5 mm BP crystal showing its facets, (right) EDS mapping of BP crystal surface illustrating 1:1 ratio of boron to phosphorus where green and red indicate boron and phosphorus respectively.

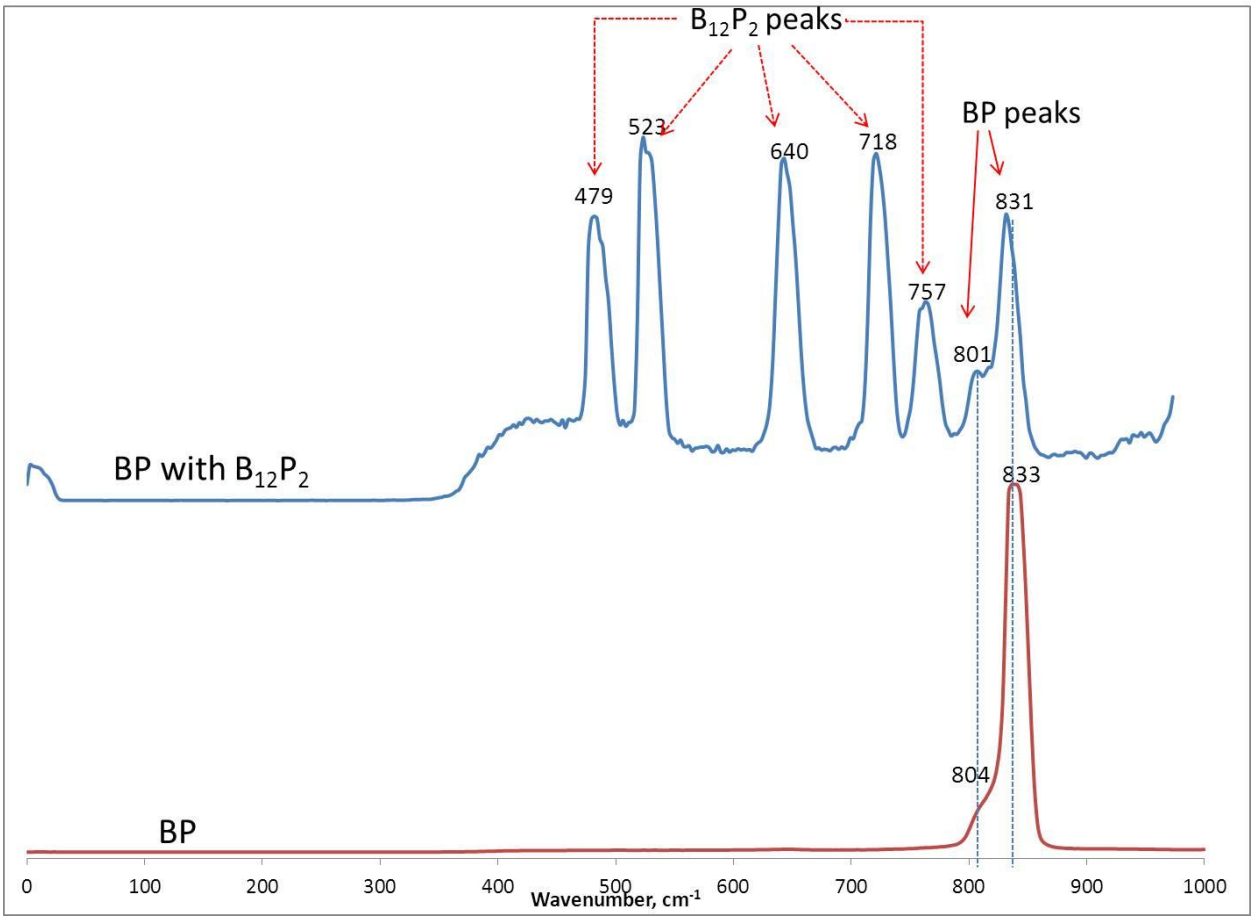

Figure 3-10: Raman spectroscopy comparison of BP crystal and BP with $B_{12}P_2$ crystals. $B_{12}P_2$ crystals were formed from an experiment where the dissolved boron was deprived of phosphorus from the formation of nickel phosphides.

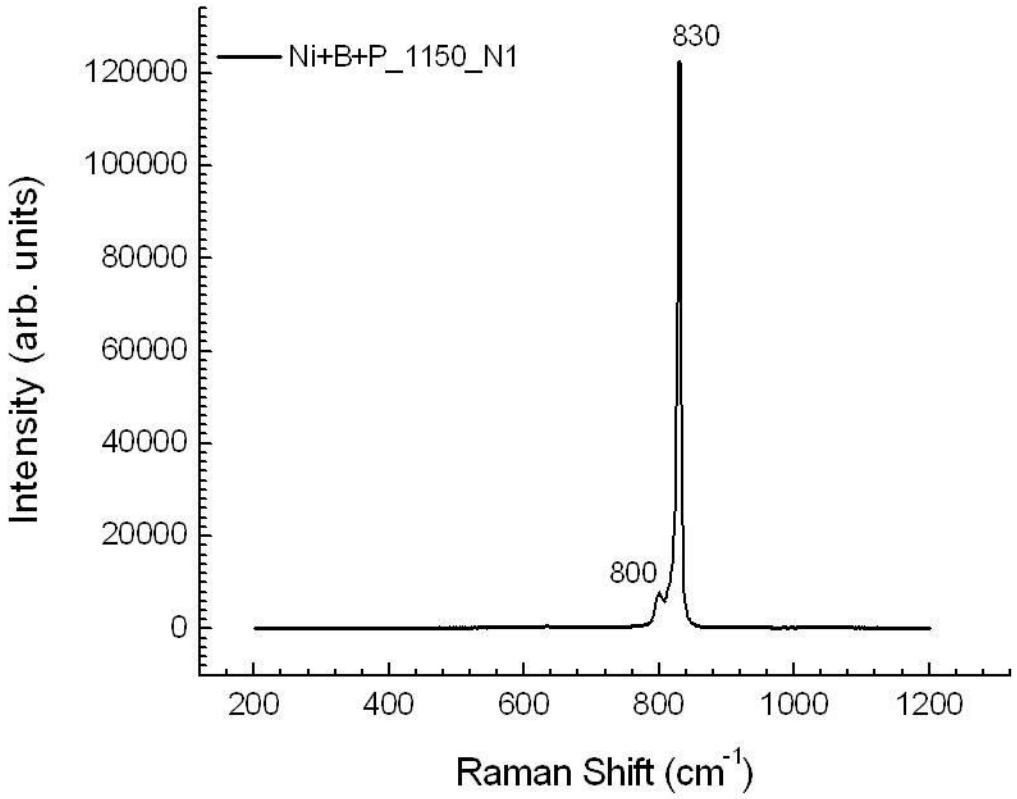

Figure 3-11: Raman spectra from a pure BP crystal with the TO peak at 800 cm^{-1} and LO peak at 830 cm^{-1}.

Table 3-1: Summary of B: P: Ni compositions used in some experiments and the resulting crystal sizes.

Ternary Compositions - B:P:Ni (Mol %)			B in Ni (Mol %)	Largest Crystal Length (mm)	comments
B	P	Ni			
22.5	50	27.5	44.9	1.7	
29.4	34.9	35.7	45.1	1.2	B dissolves, but not enough P_2. Black crystals formed
29.8	30.7	39.5	42.9	0.8	Most B dissolves
35.9	37.6	26.5	57.6	0.4	Some B dissolves
28.3	19.7	52	35.2	N/A	Most of P reacts with Ni
16.5	23	60.5	21.4	N/A	Too much Ni promotes separation

Phosphorus Pressure

The amount of phosphorus in the system is not the only factor that affects the stoichiometry of the BP crystals formed, its vapor pressure is also important. As discussed in Chapter 2, if the vapor pressure of sublimed phosphorus is less than 1 atmosphere, phosphorus reacts with boron and nickel, but it dissociates from boron phosphide (forming no crystals or only $B_{12}P_2$). Most of the phosphorus then deposits at the cooler end of the reaction vessel (quartz tube) after the experiment (as shown in Figure 3-12). Since the pressure of phosphorus in the system is controlled by the temperature, the cooler end of the quartz tube had to be kept slightly above 430°C to achieve a reaction pressure of 1-3 atmospheres. Above 450°C, the phosphorus vapor pressure is above 5 atm (see Figure 2-4) which can expand and rupture the quartz tube as shown in Figure 3-13. The rupture occurs at the hotter end of the quartz tube where the expanded phosphorus gases (expands from P_4 to $2P_2$) exerts more force on the softened quartz tube walls.

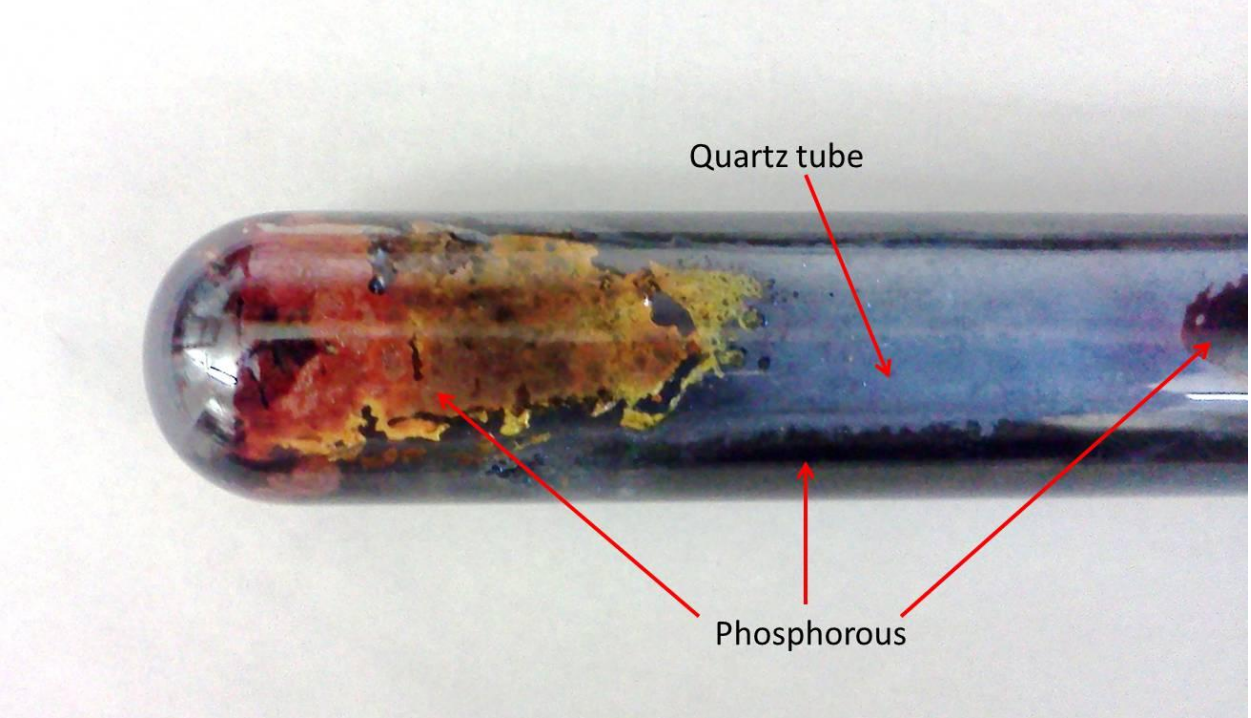

Figure 3-12: phosphorus deposited on quartz tube walls

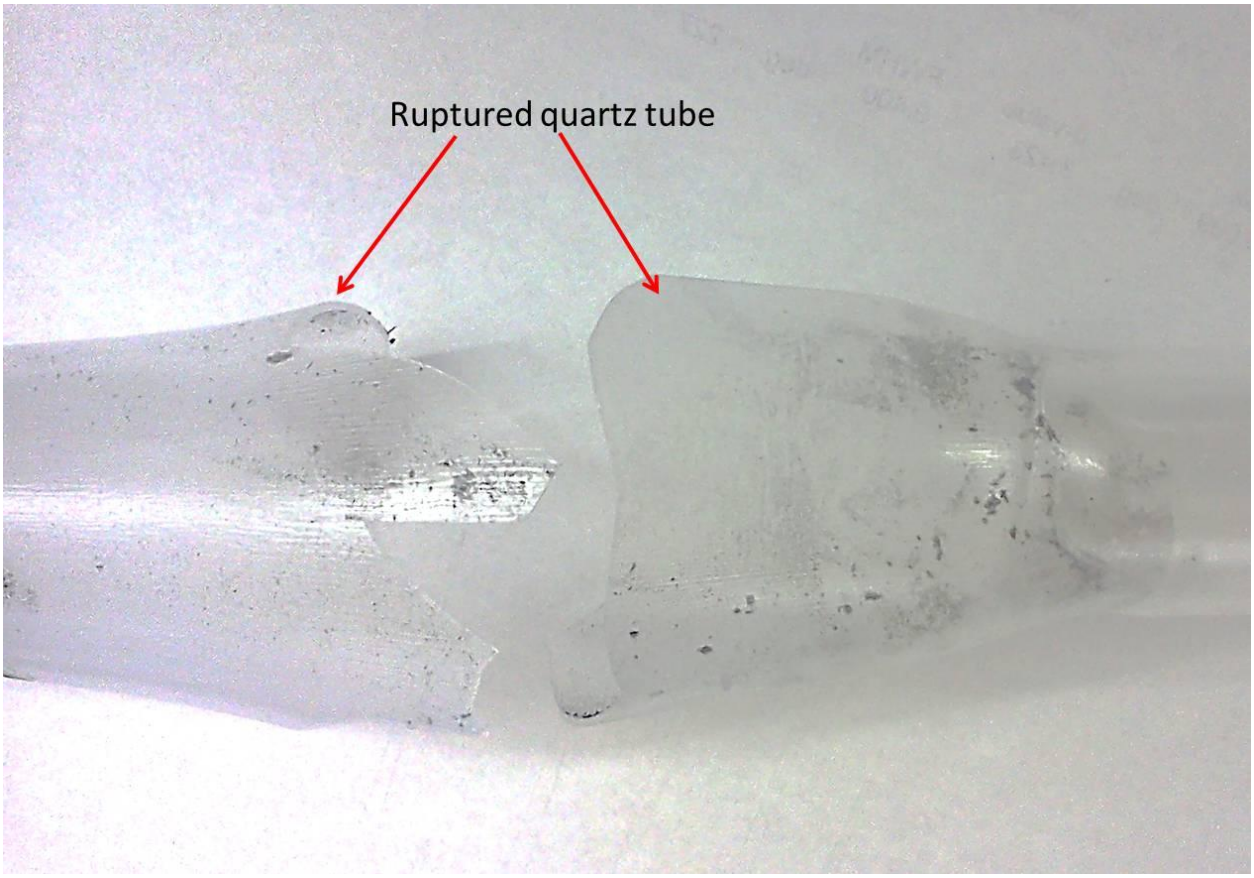

Figure 3-13: Ruptured quartz tube caused by high phosphorus vapor pressure. The tube diameter expanded to more than twice its original size before breaking.

Boron-Nickel Mixture Soak Time

The impact of the soak time, the time allotted for the nickel-boron solution to form before introducing phosphorus vapor was studied in several experiments. In cases where the phosphorus vapor was created and introduced to the B-Ni mixture without any soak time, almost no BP crystals formed. Apparently, the formation of Ni_5P_4 impeded the growth of BP crystals. Several experiments were conducted at various soak time and cooling rates (see Table 3-2) to prove that soak time really does effect the size of the crystals. Figure 3-14 shows a plot of maximum BP crystal size grown with a constant cooling rate of 3°C/hr. versus soak time. The largest BP crystals, sizes of up to 2.5 mm, were produced at the longest soak time, 52 hr, with a dwell time of 72 hours. Probably more boron is dissolved with longer soak times, and this contributes to larger BP crystals forming.

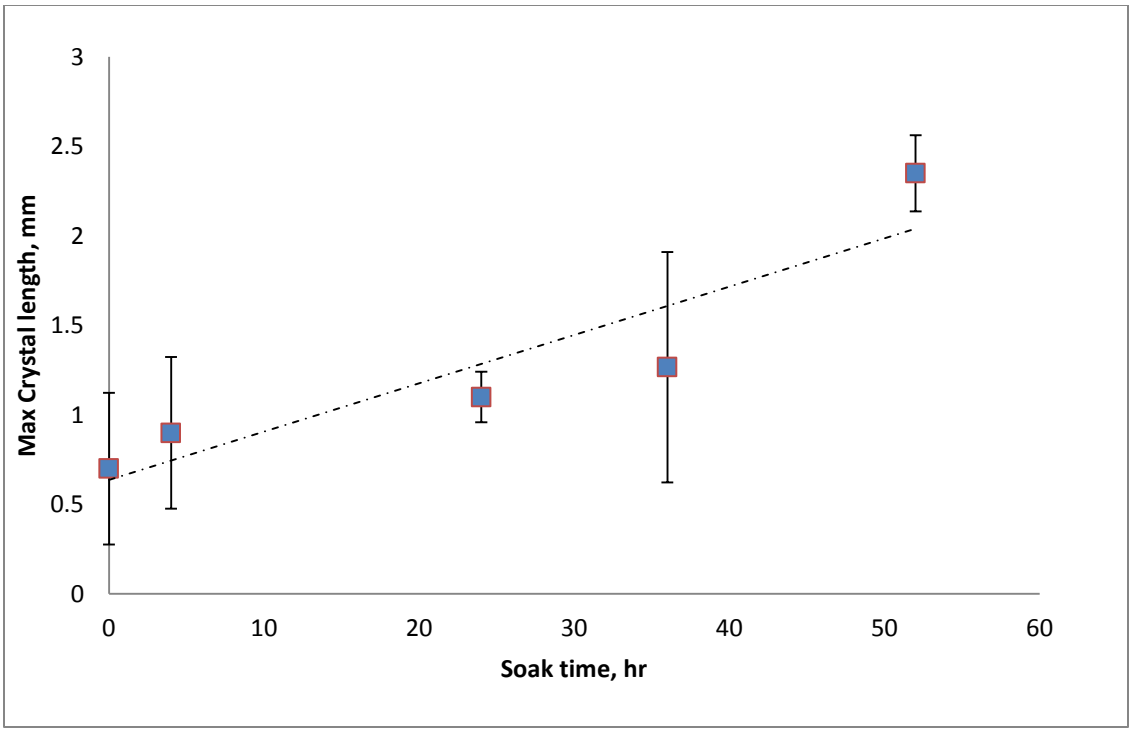

Figure 3-14: The maximum crystal length versus soak time with constant growth temperature (1150°C) and cooling rate (3°C/hr.) kept relatively constant

Table 3-2: BP crystal size as a function of cooling rates and soak times.

Dwell time constant at 72 hr.				
	Soak times at 1150°C (hr.)			
cooling rate	0 hr.	24 hr.	36 hr.	52 hr.
500°C/hr.	0mm	0.2mm	0.5mm	1mm
10°C/hr.	0.4mm	0.8mm	1.2mm	1.5mm
3°C/hr.	1mm	1.2mm	***2.2mm***	***2.5mm***

Reaction Temperature Dwell Time

Another set of experiments examined whether the time allowed for phosphorus reaction with the B-Ni mixture had any effects on the growth of BP crystals. Table 3-3 summaries the results of crystal growth carried out at constant soak time of 36 hr. with varying cooling rates and

dwell times. The maximum crystal size increased with the dwell time. The largest crystal, length of 4 mm, was obtained with a soak time of 36 hr. and a dwell time of 96 hr. This result suggests that with more time the phosphorus can completely diffuse into the B-Ni solution. Figure 3-15 shows the plot of crystal sizes grown at various dwell times with a constant cooling rate of 3°C/hr. and growth temperature of 1150°C.

Table 3-3: BP crystal size as a function of cooling rates and high temperature dwell times.

Soak time constant at 36 hr.				
cooling rate	Dwell times at 1150°C (hr.)			
	0 hr.	52 hr.	72 hr.	96 hr.
500°C/hr.	0 mm	0 mm	0.5 mm	1 mm
10°C/hr.	0 mm	1 mm	1.5 mm	2.5 mm
3°C/hr.	0 mm	1.2 mm	2.5 mm	***4 mm***

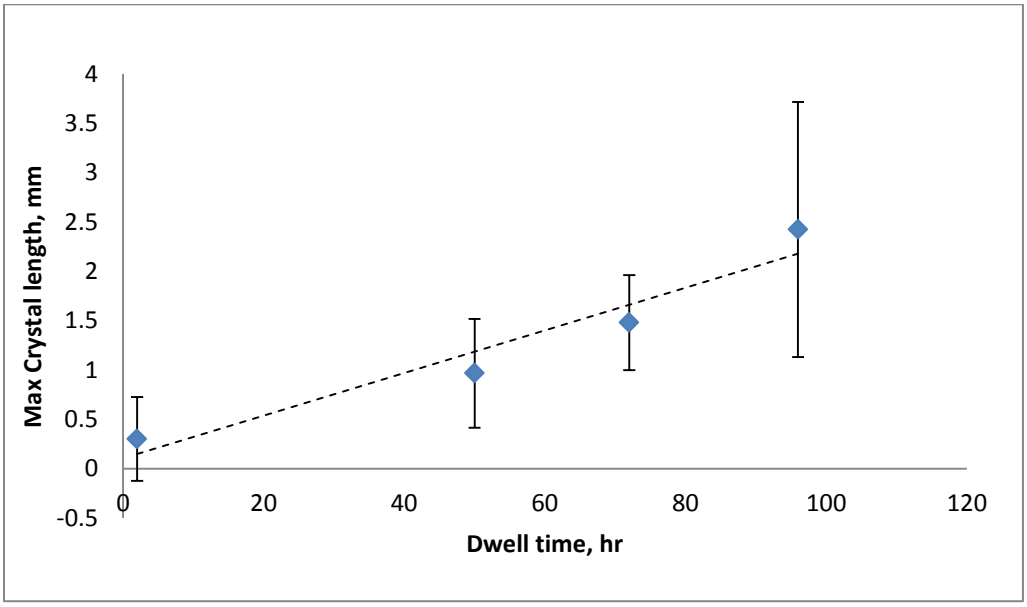

Figure 3-15: Crystal length versus dwell time with constant growth temperature (1150°C) and cooling rate (3°C/hr.).

Reaction Cooling Rate

The cooling rate also affected the crystal size. Plots of the crystal length for three cooling rates are presented in Figure 3-16 and Figure 3-17. Granule size crystals (<<1 mm) were formed at high cooling rates (>10 ºC/hr.), while slower cooling rates produced larger crystals formed. Thus, it is safe to say that slow cooling rates allow the already formed BP nuclei to act as seeds to form bigger crystalline structures.

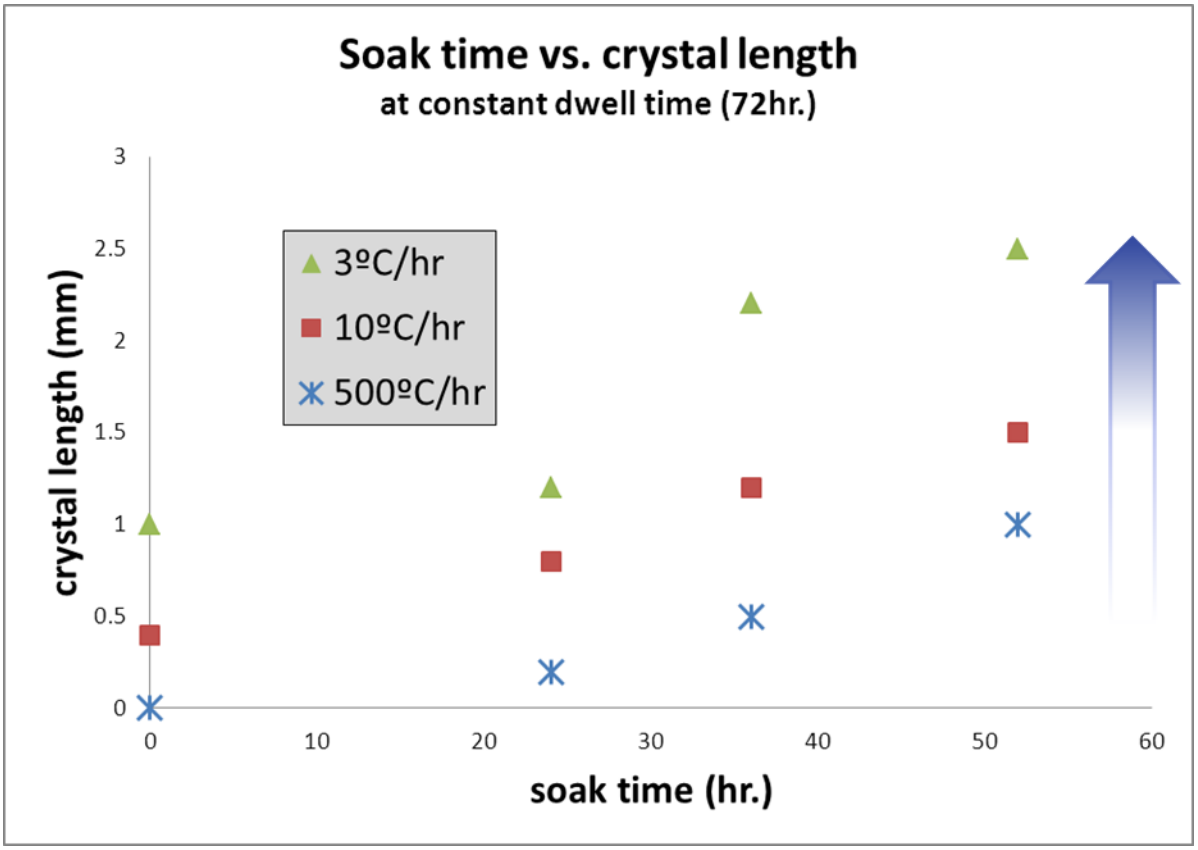

Figure 3-16: Crystal size versus soak time for three cooling rates. The crystal size increases with the soak time and decrease with cooling rate.

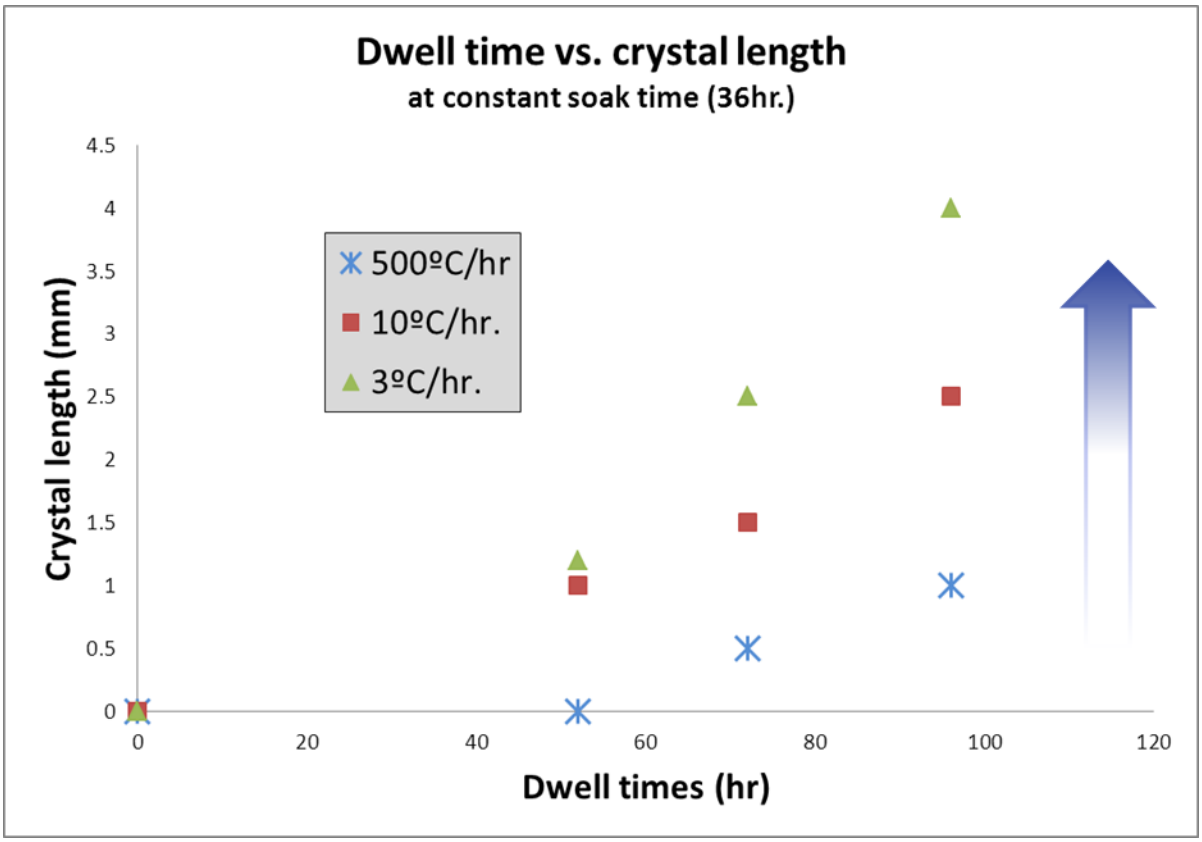

Figure 3-17: The crystal size at various dwell times for three cooling rates.

Additional Characterization Results

Defect Selective Etching (DSE)

The defect selective etching temperature and time was optimized by utilizing 50:50 eutectic mixtures of KOH and NaOH as an etchant. The crystals were etched within a minute at temperatures above 325°C, but weren't visibly etched at 300°C. The crystals were first visibly etched within two minutes at 300°C and etched faster above 325°C. BP didn't etch below 300°C but revealed lots of etch pits above 325°C after one minute. The etchant produced triangular and striated etch pits on two different crystal planes, probably (111) and (100).

Studies to optimize the etch temperature were done first at temperatures between 300°C and 475°C for one minute. For this amount of time the crystals were etched at 325°C, 350°C, 425°C, and 475°C. SEM images of the results are shown in Figure 3-18. The etch pit edges were rough and the overlapped when etched between 325°C and 475°C. At 475ºC, the etching is very aggressive and is no longer selective, based on Figure 3-18D. Thus, such conditions were too

aggressive to accurately determine the EPD. Etching above 325°C is too high a temperature for one minute. Although at 300°C etching for one minute did not produce any etch pits, pits were seen after two minutes. Images of the same crystal before and after etching at 300°C for 2 minutes are shown in Figure 3-19. Both triangular and striated etch pits were observed on different facets of the crystal. SEM image of the crystal (seen in Figure 3-20) has some overlapping etch pits, but it was good enough to obtain an average EPD. The calculated average EPD of the triangular and striated etch pits were ~4 x 10^7 cm^{-2} and 9.2 x 10^7 cm^{-2} respectively.

For other semiconductors such as GaAs, InP, and GaN, the polarity of the close-packed planes can be distinguished by etching. For example, the N-polar (0001) GaN plane is reactive while the Ga-polar plane is essentially inert. Etch pits were observed on two facet of the BP crystals. If the etching behavior of boron phosphide is similar to other boron semiconductors, the boron polarized facets on the boron phosphide will always develop etch pits (*67*). The (111) plane in a zinc blende structure could be either B-polar or P-polar. The B-polarity is (111) while the P-polar surface is ($\overline{1}\overline{1}1$). This makes it easy to distinguish the different facets of a BP crystal.

Ideally, DSE should produce sharp edges and flat surfaces that correspond to slow etching crystallographic planes. Such well-defined features are produced with the DSE of other semiconductors such as GaN, SiC, and GaAs. The shape of the etch pits formed is determined by the specific crystal plane being etched and the slow etching planes that intersect the surface. Inverted tetrahedrons and pyramids are common to cubic symmetry (or zinc-blende) DSE etched (111) and (100) planes respectively. Rectangles occur on the (110) planes. The same general shapes are visible after etching BP crystals, but the edges of the features are rougher and less defined.

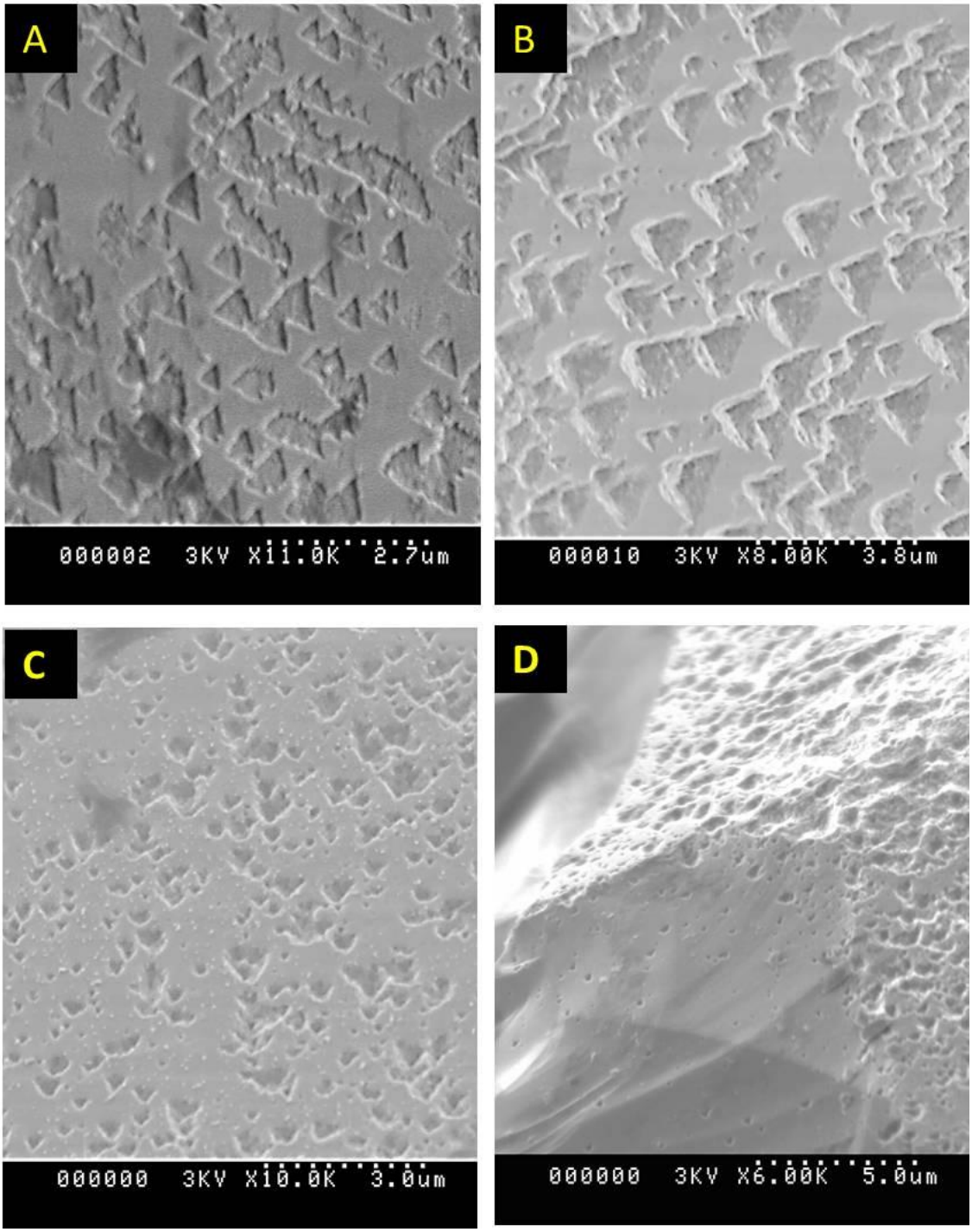

Figure 3-18: SEM images of BP etched in eutectic KOH/NaOH at (A) 325°C, (B) 350°C, (C) 425°C and 475°C for one minute.

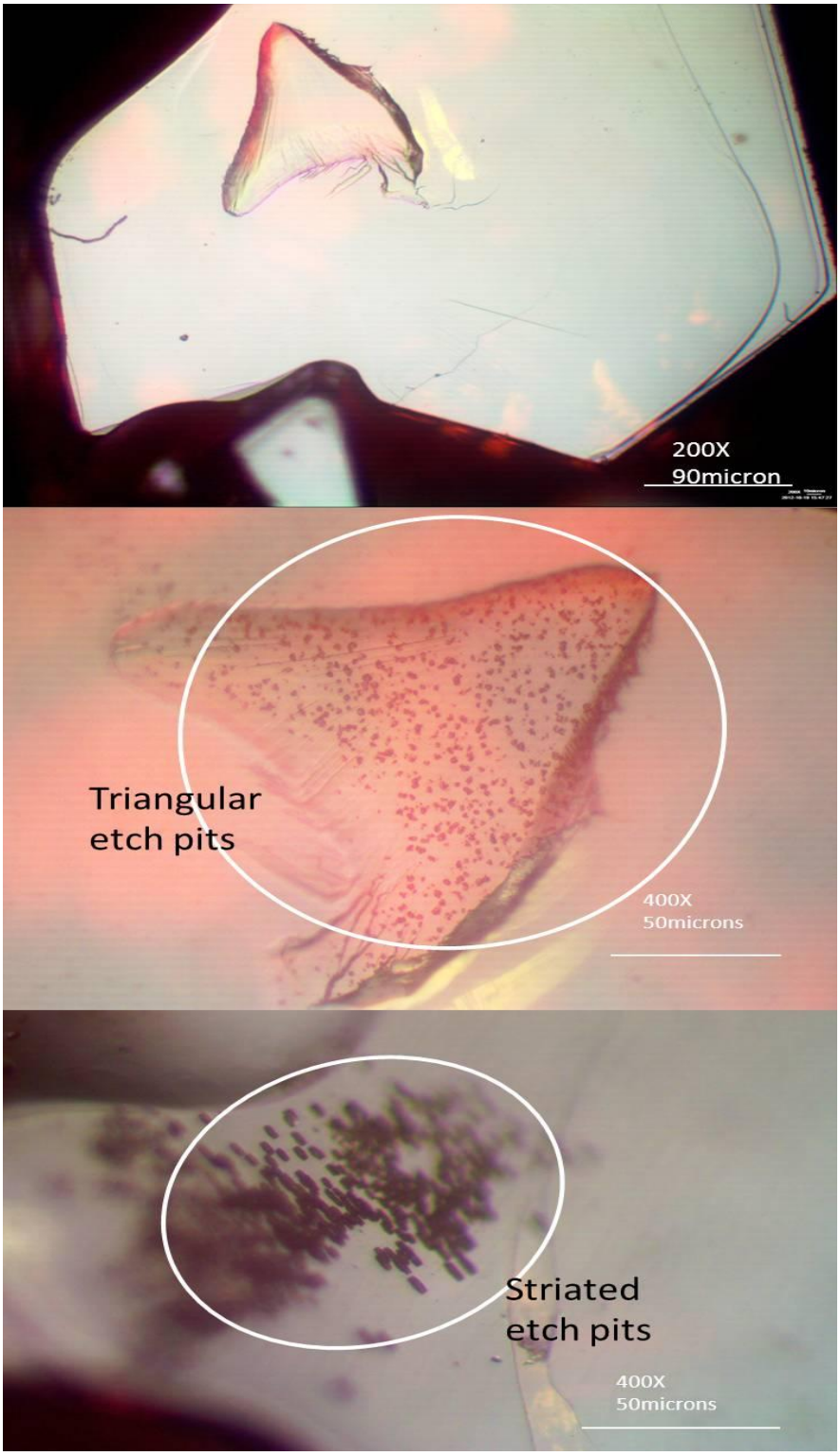

Figure 3-19: Microscope images of BP before etching at 300°C under low magnification (top), etched at 300°C for 2 minutes revealing triangular etch pits (middle) and striated etch pits (bottom).

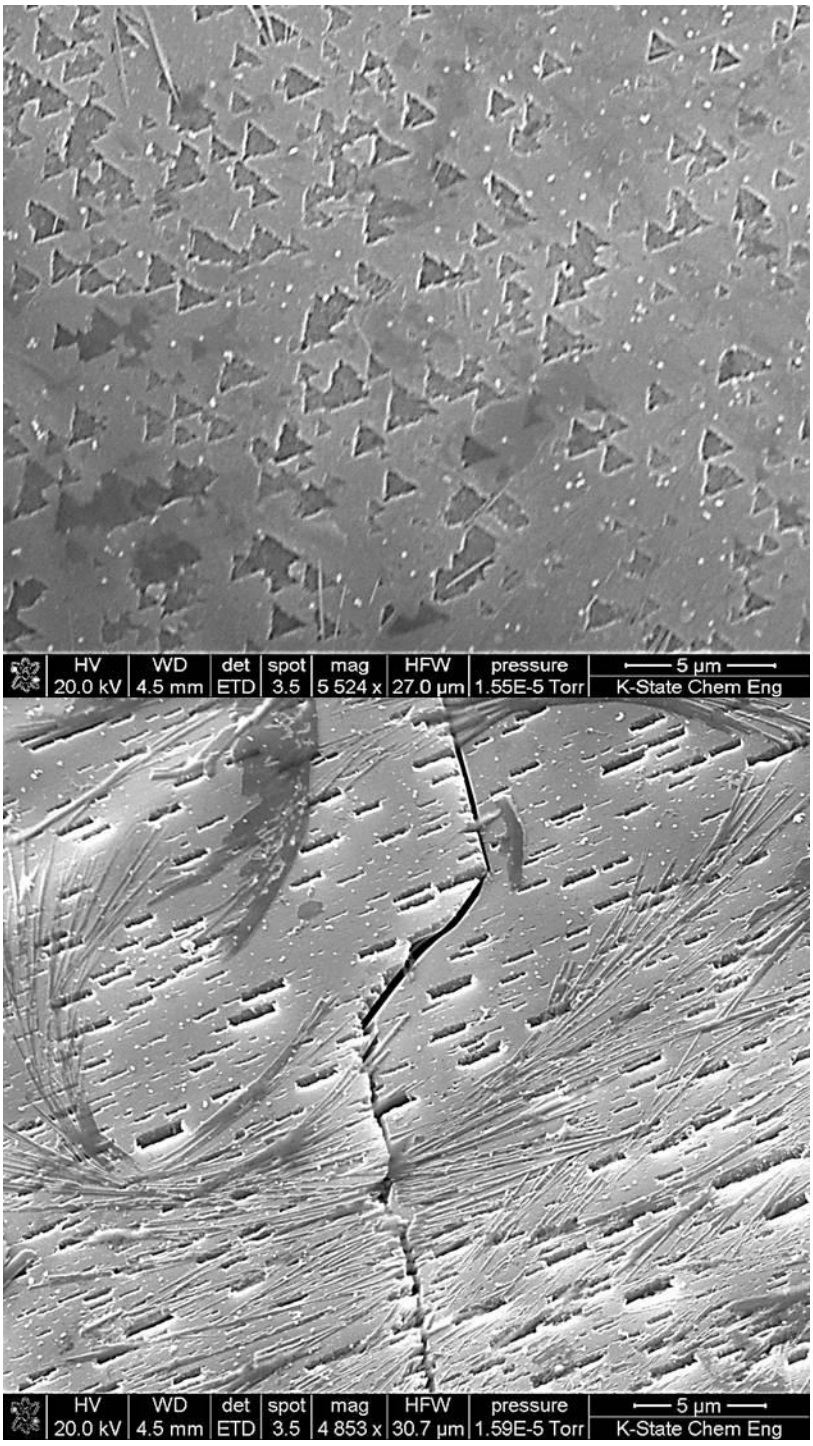

Figure 3-20: SEM image of two different facets of a BP crystal etched at 300°C for 2 minutes. (Top) Triangle-shaped pits formed on what is probably a (111) facet, (bottom) rectangle-shaped pits formed on what is probably a (110) plane. The string-like features are probably residual KOH-NaOH remaining on the surface of the sample.

Electrical Analysis

The I-V measurement of an Au-BP Schottky device is shown in Figure 3-21. The device had rectifying behavior which is evident from the plateau between -2V to +0.5V. This is typical for a diode. I-V plot along with its semi-log plot (seen in Figure 3-22) was employed to compute the turn-on voltage, ideality factor, and leakage current density of the diode. Rectifying behavior is desired because small fluctuations of voltage in this region during operation of a neutron detector will not produce any significant change in current. Therefore, only current changes due to interaction with neutrons will be measured. The turn-on voltage of the devices is around 0.9V, had an ideality factor of 2.4, and a leakage current density of 0.40 $\mu A*cm^{-2}$. The high ideality factor ($\eta = 1$ for ideal) of the device results from compensating impurities in the BP crystals, which reduces the resistance, R in the diode.

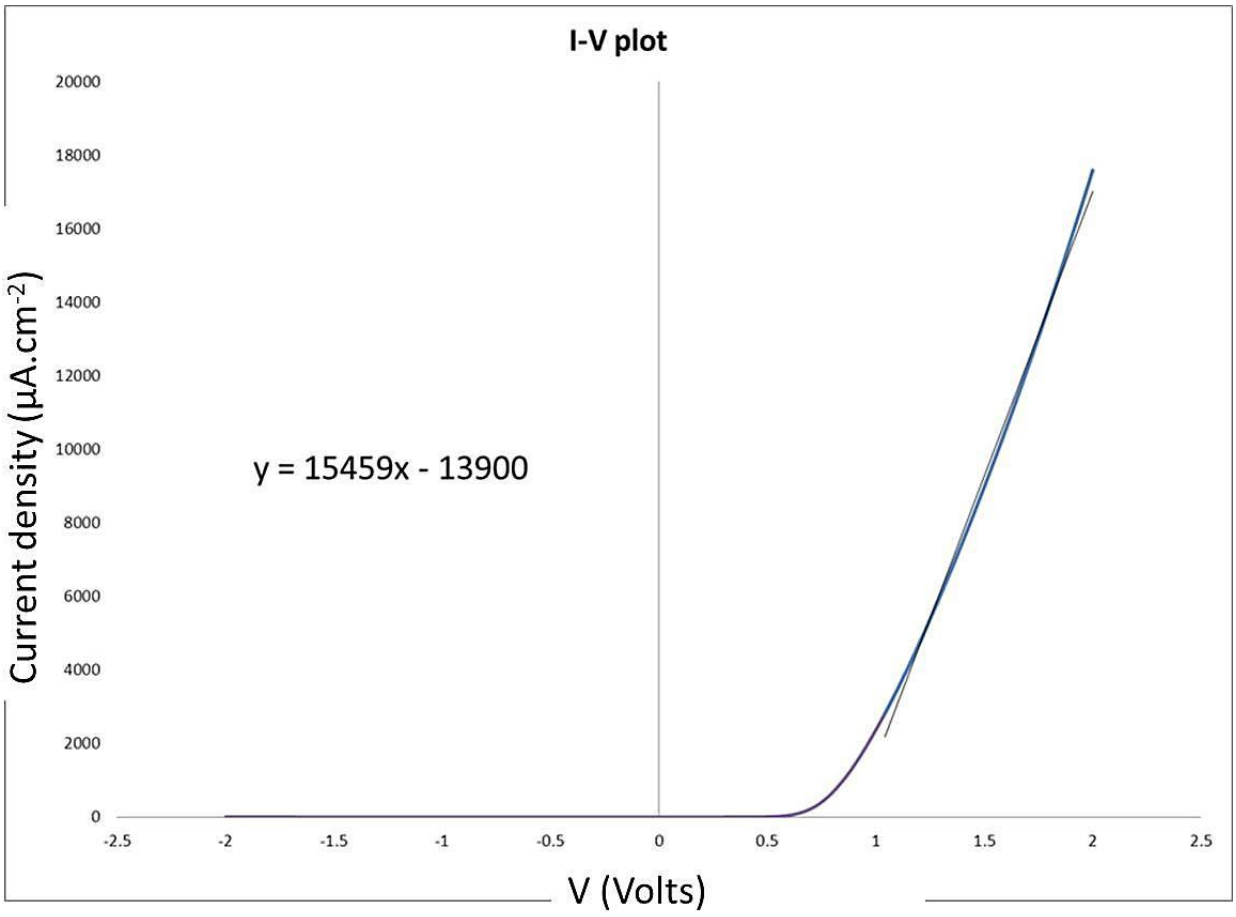

Figure 3-21: I-V measurement of an Au-BP Schottky diode showing a rectifying behavior.

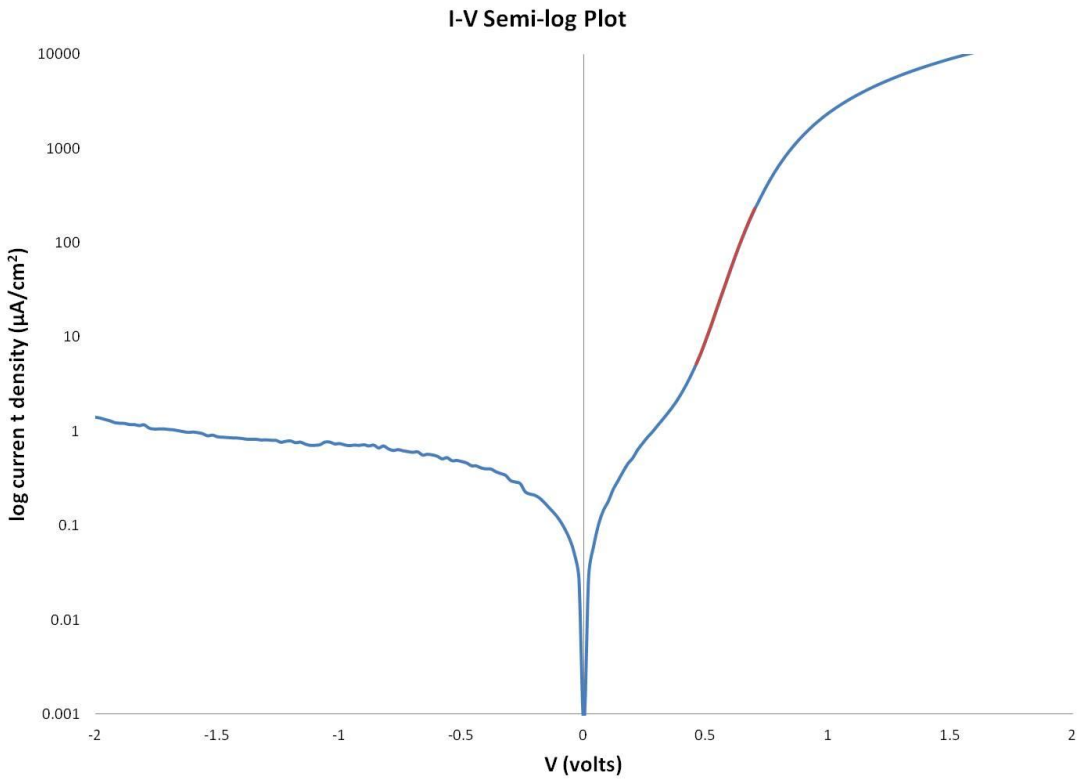

Figure 3-22: Semi-log I-V plot of an Au-BP Schottky diode.

The resistivity, ρ_{sh} of the BP crystals was also calculated from a I-V measurement. Measurements were made between the 1-2, 1-5, and 1-6 Au-Cr ohmic contacts on a BP crystal (shown in Figure 3-23). The I-V plot in Figure 3-24 shows that the slope which is the inverse of the resistance, decreases as spacing between the contacts increases. This is also illustrated in the plot of contact distance against resistance in Figure 3-25. The contact resistance was 0.0964 Ω*cm^2, and the resistivity of the BP crystal was approximately 0.0136 Ω*cm which is well within the range reported in literature between ~ 10^2 to 10^{-4} Ω*cm (*10*, *31*, *32*).

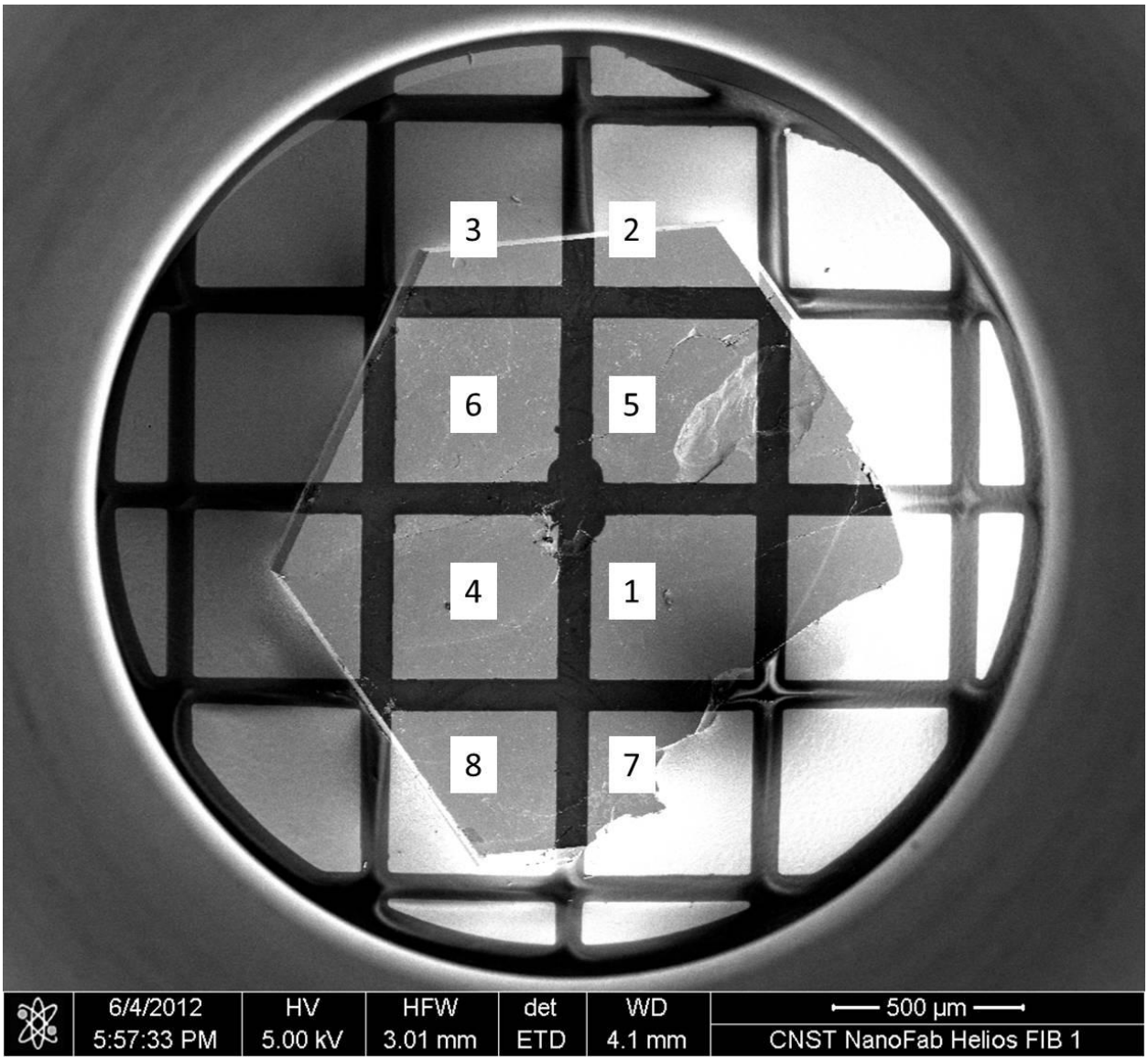

Figure 3-23: A SEM micrograph of a BP crystal with numbered Au-Cr ohmic contacts for resistivity and Hall-effect measurements.

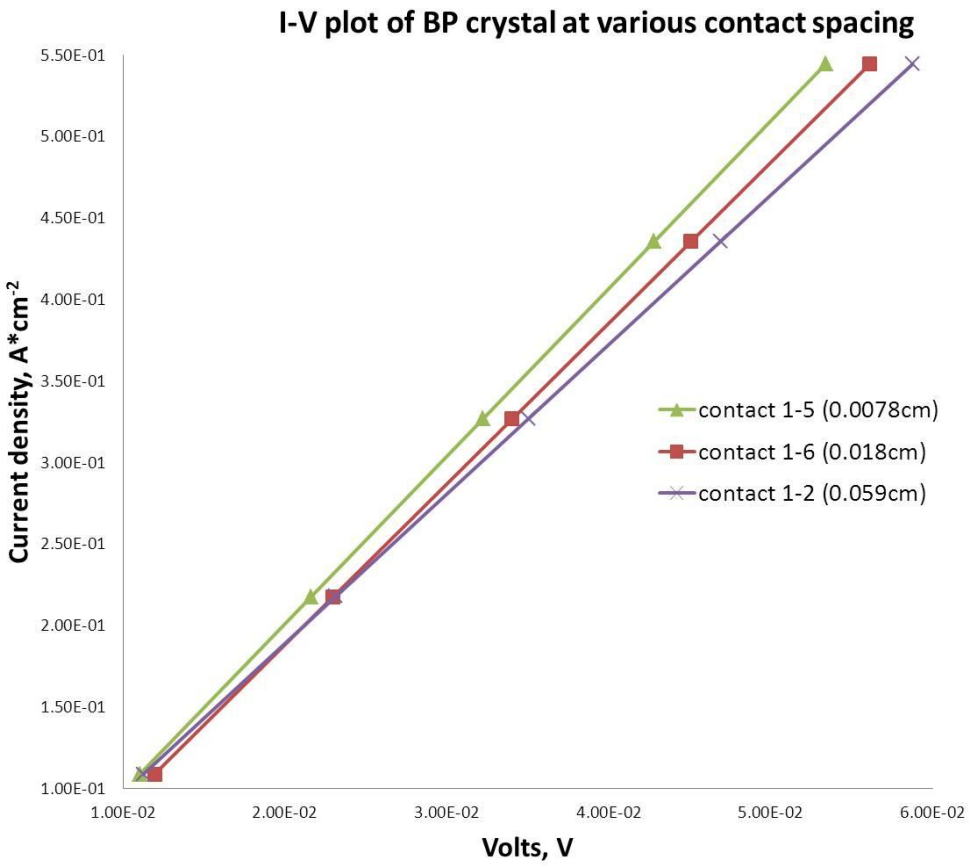

Figure 3-24: I-V plots between ohmic contacts at various contact spacings on a BP crystal.

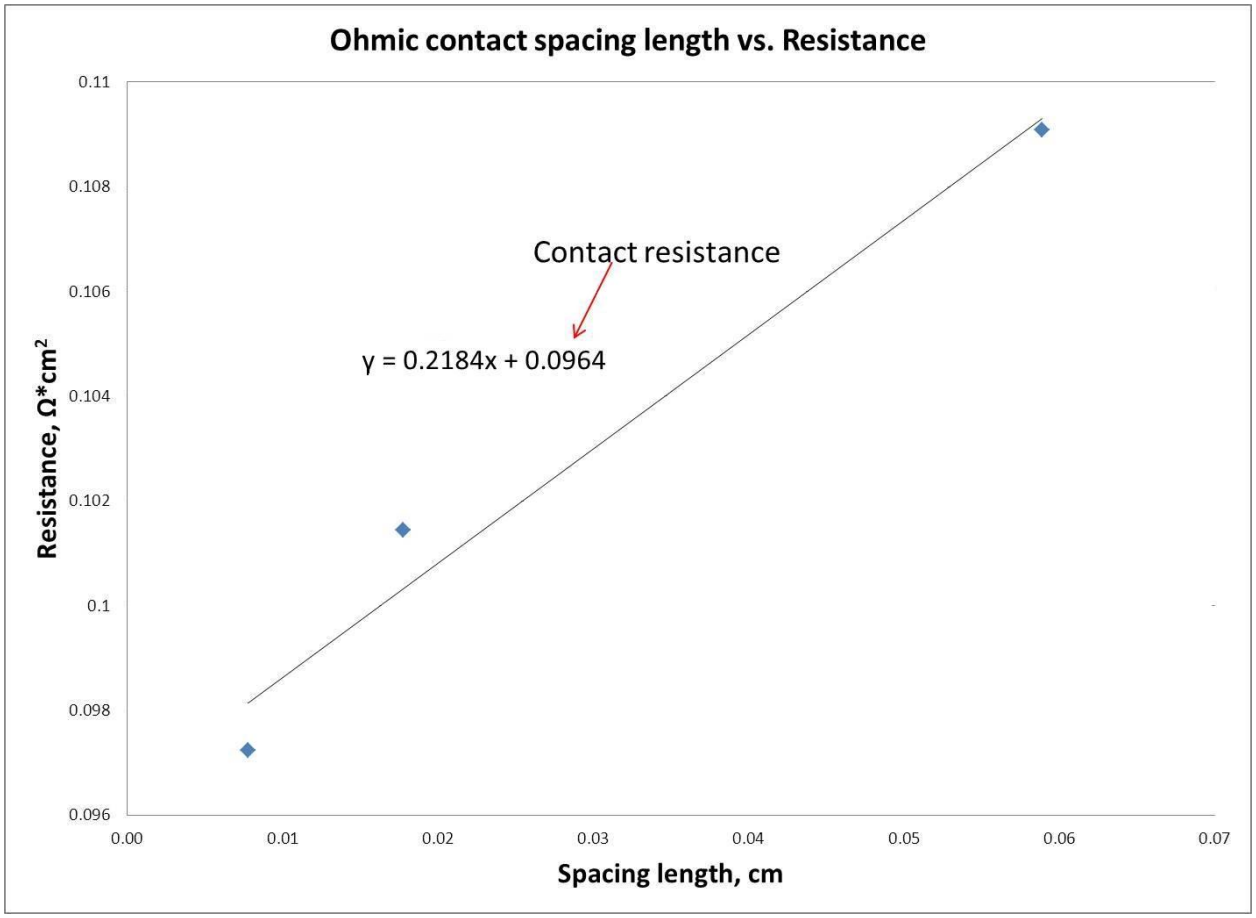

Figure 3-25: Ohmic contact spacing length on a BP crystal versus its resistance. The resulting slope is the resistance and the y-intercept is the contact resistance of the crystal shown in Figure 3-23.

The result of the capacitance measurement for Au-BP Schottky device at various voltages is shown in Figure 3-26. The device was fully depleted at a reverse bias of -0.5 V demonstrating low-voltage operations. The plot of capacitance showed signs of hysteresis as positive and negative voltage sweeps during data collection showed different results. The hysteresis behavior could be the result of high charge trapping caused by impurities in the crystal. This made it difficult to calculate the dopant density, and dielectric constant of the Au-BP Schottky device. Several researchers have reported values of the dielectric constant and dopant density to be between 6.9-11 and ~10^{15}-10^{18} cm^{-3} respectively (*36*, *42*, *68–70*). The linear relation of $1/C^2$ with the voltage is shown in Figure 3-27. The extrapolation of the line to the voltage axis intercept gives a value for the built-in potential of the device of 0.64 volts. This means that any external

current (from the neutron interaction) passed through the Schottky device will develop about 0.64 volts across it.

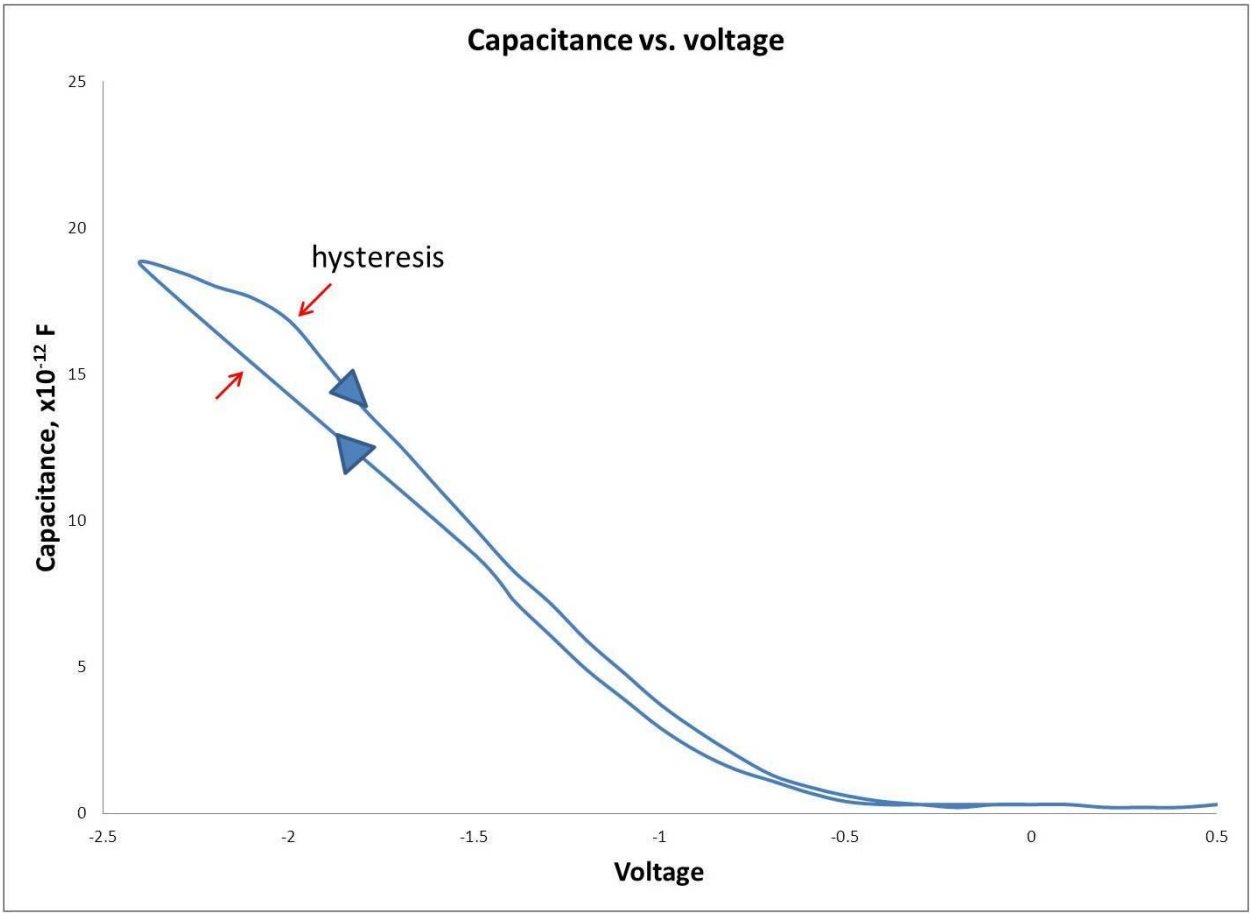

Figure 3-26: Capacitance versus voltage measurement of the BP Schottky diode. The response was slightly different as the voltage was swept in the opposite direction leading to hysteresis.

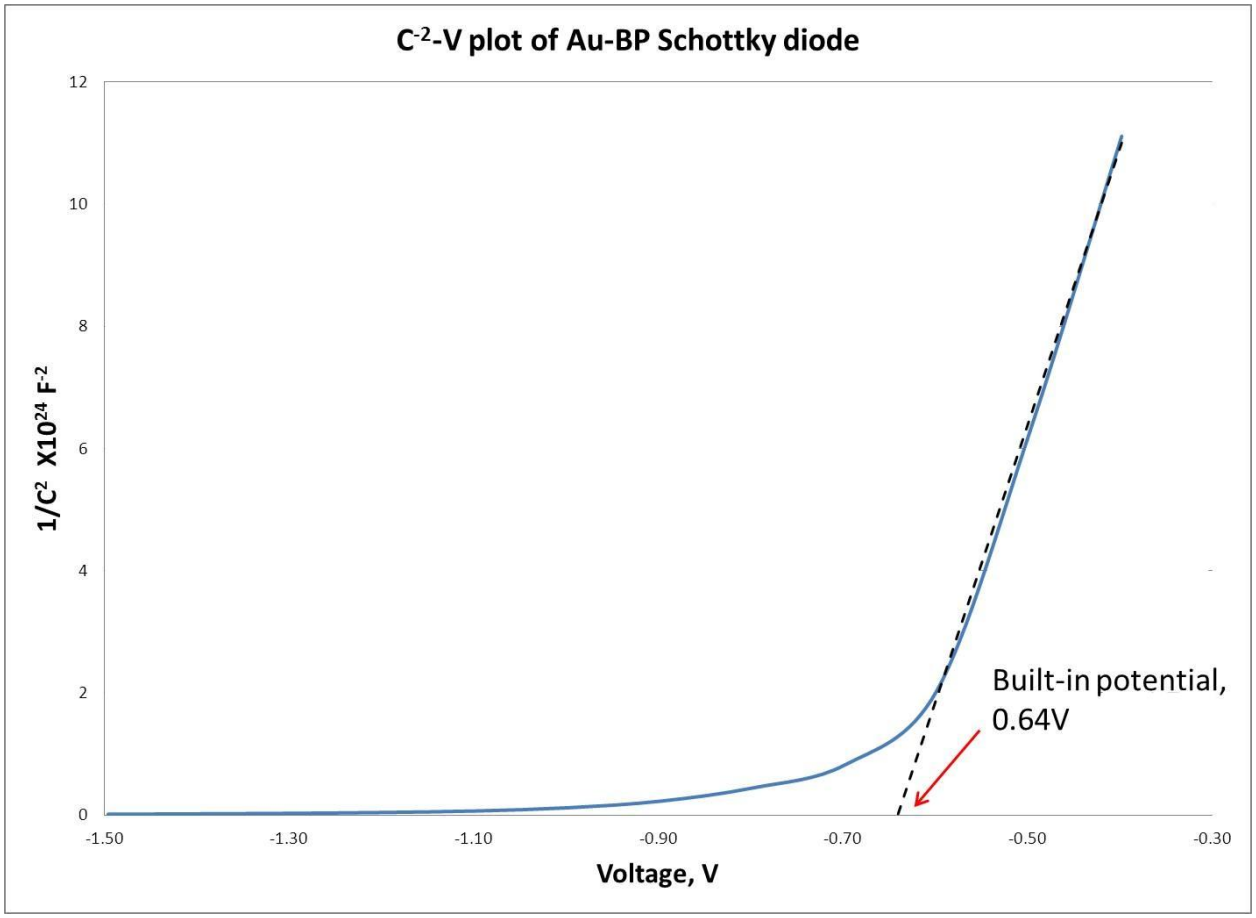

Figure 3-27: $1/C^2$ versus applied voltage bias for Au-BP Schottky diode.

Further electrical evaluation was done on the BP crystal shown in Figure 3-23 utilizing a Hall-effect measurement with a magnetic field of 5 kG at room temperature. The crystal had *n*-type conductivity with a resistivity of 0.0137 Ω*cm, the same as result calculated using resistance at various contact spacings. The highest carrier mobility and the lowest carrier concentration of the BP crystal were ~39.8 $cm^2/(V*s)$ and 1.141 x 10^{19} cm^{-3} which is similar to the results reported in literature (*10*, *11*, *29*, *71*) for BP grown through other methods without any intentional doping of the crystal. The mobility is high enough to quickly move and collect electrons and holes created from neutron interaction before they recombined or are trapped (*72*).

Chapter 4 - Conclusions and Recommendations

The goal of this research was to grown cubic BP crystals that could be used in neutron detectors. Some parameters such as the growth conditions, and reactant compositions, as well as the structural characterization, and electrical properties of the crystals were examined.

At a growth temperature of 1150°C, with a boron and nickel eutectic composition (45at.% boron), the longer the soak time the more homogeneous the solution became. Since boron and nickel phosphides are formed when phosphorus vapor interacts with the metal solution, a reasonable amount of phosphorus (>40 mol. %) along with vapor pressure greater than atmospheric (but not greater than the reactor's rupture pressure) was required to insure the formation of stoichiometric BP and also the nickel phosphide side product. Larger crystals, with dimensions up to 3 mm x 4 mm x 1 mm, were obtained from experiments with an extended reaction time (dwell time at 96 hr.), and also a slow cooling rate (<3°C/hr.) than from experiments with no reaction time and fast cooling rate. Applying these parameters to a large scale of crystal growth may yield larger size crystals (>1 cm^3) which will make device fabrication of neutron detectors easier.

X-Ray diffraction showed that the BP crystals are highly crystalline. The FWHM of the narrowest peak, (111), is 0.275° which is the narrowest ever reported. This demonstrates the high quality of the produced crystals.

The Raman spectroscopy of the crystals showed intense, sharp phonon peaks located at 800 cm^{-1} and 830 cm^{-1}, in agreement to values reported in the literature. The FWHM of the 830 cm-1 peak is 4 cm-1 which also shows that the crystals are high quality crystals.

Defect selective etching of BP crystals at 300°C for 2 minutes in molten eutectic mixture of KOH and NaOH produced low densities of triangular and striated etch pits of about 4 x 10^7 cm^{-2} and 9.2 x 10^7 cm^{-2} respectively on different facets of BP crystals. These different facets which are believed to be the (111) B and (100) faces of BP crystals would require further investigation. Calibration is needed to make it clear what defect is associated with the etch pits formed. Possibilities include edge screw and mixed dislocations.

The electrical characteristics of the produced crystals were measured with I-V, C-V, and Hall-effect measurements. I-V measurement of a diode made for a BP crystal, showed a rectifying behavior with, a turn-on voltage of 0.9V, a leakage current density of 0.4 $\mu A*cm^{-2}$,

and an ideality factor of 2.4. A built-in potential of 0.64 volts was calculated from the C-V measurement of the diode. Hall-effect measurement revealed that the crystals produced were *n*-type carriers with a charge mobility of 39.8 $cm^2/(V*s)$, a carrier concentration of 1.149 x 10^{19} cm^{-3}, and resistivity of 0.0137 Ω*cm. Although properties needed for neutron detection such as, high charge mobility, high resistivity and low operation voltage were achieved, the crystals have high ideality factor, and below normal electrical properties. This can be credited to impurity concentrations in the crystals and also the metal contacts. There could be more optimization of the metal contacts. I think this could be a big source of the problem.

Future study will surely include producing larger, higher purity quality BP crystals. Measuring the impurity concentrations is the first step, and then reducing their concentration is next. This can be done by starting with higher purity source materials and introducing oxygen absorbing metal (such as Ti, Al) in the reaction vessel during a scaled-up flux growth, or by using crystals grown through flux growth as substrates for epitaxial growth of BP crystals with less lattice constraints and easily controlled doping. Higher purity crystals will improve BP's electrical properties so it can be applied in neutron detection. Thus, a more precise elemental analysis is recommended to track improvements of the crystal purity. Although 4 mm sized crystals are sufficient enough for neutron capture, scaling up to produce larger crystals will allow for easy handling and easier device fabrication.

References

(1) Helium-3 shortage endangers nuclear detection capabilities. http://www.homelandsecuritynewswire.com/helium-3-shortage-endangers-nuclear-detection-capabilities (accessed June 6, 2012).

(2) Crane, T. W.; Baker, M. P. *Neutron Detectors*; pp. 379–406.

(3) Norris, R. S.; Kristensen, H. M. Global nuclear stockpiles, 1945-2006. *Bulletin of the Atomic Scientists* **2006**, *62*, 64–66.

(4) Nikolic, R.; Conway, A. Fabrication of Pillar-structured thermal neutron detectors. *IEEE Nuclear Science Symposium Conference Record* **2007**, *2*, 1577– 1580.

(5) Rose, A. Sputtered boron films on silicon surface barrier detectors. *Nuclear Instruments and Methods* **1967**, *52*, 166–170.

(6) Robertson, B. W.; Adenwalla, S.; Harken, a.; Welsch, P.; Brand, J. I.; Dowben, P. a.; Claassen, J. P. A class of boron-rich solid-state neutron detectors. *Applied Physics Letters* **2002**, *80*, 3644.

(7) McGregor, D. S.; Unruh, T. C.; McNeil, W. J. Thermal neutron detection with pyrolytic boron nitride. *Nuclear Instruments and Methods in Physics Research Section A: Accelerators, Spectrometers, Detectors and Associated Equipment* **2008**, *591*, 530–533.

(8) Kumashiro, Y.; Kudo, K.; Matsumoto, K.; Okada, Y.; Koshiro, T. Thermal neutron irradiation experiments on ^{10}BP single-crystal wafers. *Journal of the Less Common Metals* **1988**, *143*, 71–75.

(9) Moissan, H. Préparation et propriétés des phosphures de bore. http://visualiseur.bnf.fr/CadresFenetre?O=NUMM-3069&I=726&M=tdm (accessed July 7, 2011).

(10) Takenaka, T.; Takigawa, M.; Shohno, K. Diffusion layers formed in Si substrates during the epitaxial growth of BP and application to devices. *Journal of The Electrochemical Society* **1978**, *I*, 633–637.

(11) Kumashiro, Y. Refractory semiconductor of boron phosphide. *Journal of Materials Research* **1990**, *5*, 2933–2947.

(12) Popper, P.; Ingles, T. A. Boron phosphide, a III–V compound of zinc-blende structure. *Nature* **1957**, *179*, 1075–1075.

(13) Schmitt, J. O.; Edgar, L. J. H.; Liu, L.; Nagarajan, R.; Szyszko, T.; Podsiadlo, S.; Wojciech, G. Close-spaced crystal growth and characterization of BP crystals. *Physica Status Solidi (C)* **2005**, *2*, 1077–1080.

(14) Stone, B.; Hill, D. Semiconducting properties of cubic boron phosphide. *Physical Review Letters* **1960**, *4*, 282–284.

(15) Bouhafs, B.; Aourag, H.; Ferhat, M.; Certier, M. Competition between the ionic and covalent character in the series of boron compounds BP, BAs, and BSb. *Journal of Physics: Condensed Matter* **1999**, *11*, 5781–5796.

(16) Wentzcovitch, R. M.; Chang, K.; Cohen, M. L. Electronic and structural properties of BN and BP. *Physical Review B* **1986**, *34*, 1071.

(17) Wang, L. D.; Kwok, H. S. Cubic aluminum nitride and gallium nitride thin films prepared by pulsed laser deposition. *Applied Surface Science* **2000**, *154-155*, 439–443.

(18) Goossens, A.; Schoonman, J. An impedance study of boron phosphide semiconductor electrodes. *J. Electrochem. Soc* **1992**, *139*, 893–900.

(19) Emin, D. Icosahedral Boron-Rich Solids. *Physics Today* **1987**, *40*, 55.

(20) Emin, D. Unusual properties of icosahedral boron-rich solids. *Journal of Solid State Chemistry* **2006**, *179*, 2791–2798.

(21) Lund, J. C.; Olschner, F.; Ahmed, F.; Shah, K. S. Boron phosphide on silicon for radiation detectors. *MRS Proceedings* **1989**, *162*, 601.

(22) Dalui, S.; Hussain, S.; Varma, S.; Paramanik, D.; Pal, A. Boron phosphide films prepared by co-evaporation technique: Synthesis and characterization. *Thin Solid Films* **2008**, *516*, 4958–4965.

(23) Institute, I. Physical Properties of Silicon (Si). http://www.ioffe.ru/SVA/NSM/Semicond/Si/.

(24) Goldberg, Y. A.; Levinshtein, M.; Rumyantsev, S. L. *Properties of Advanced Semiconductor Materials: GaN, AIN, InN, BN, SiC, SiGe*; John Wiley & Sons, Inc.: New York, 2001.

(25) Edgar, J. H. *Properties of Group III Nitrides*; Institution of Engineering and Technology: London, 1994.

(26) Harris, G. L. *Properties of Silicon Carbide*; INSPEC: Institute of Electrical Engineers: London, 1995.

(27) Slack, G.; Bartram, S. Thermal expansion of some diamondlike crystals. *Journal of Applied Physics* **1975**.

(28) Chu, T.; Jackson, J.; Smeltzer, R. The crystal growth of boron monophosphide from metal phosphide solutions. *Journal of The Electrochemical Society* **1973**, 3–5.

(29) Shohno, K.; Takigawa, M.; Nakada, T. Epitaxial growth of BP compounds on Si substrates using the B_2H_6-PH_3-H_2 system. *Journal of Crystal Growth* **1974**, *24-25*, 193–196.

(30) Chu, T.; Jackson, J.; Smeltzer, R. The growth of boron monophosphide crystals by chemical transport. *Journal of Crystal Growth* **1972**.

(31) Nishinaga, T.; Ogawa, H.; Watanabe, H.; Arizumi, T. Vapor growth of boron monophosphide using open and closed tube processes. *Journal of Crystal Growth* **1972**, *13*, 346–349.

(32) Kumashiro, Y. Isotope effects on boron phosphide single-crystal wafers. *Journal of Crystal Growth* **1993**, *132*, 611–613.

(33) Williams, F. V.; Ruehrwein, R. A. The preparation and properties of boron phosphides and arsenides. *Journal of the American Chemical Society* **1960**, *82*, 1330–1332.

(34) Chu, T.; Hyslop, A. Crystal growth and properties of boron monoarsenide. *Journal of Applied Physics* **1972**, *43*, 276–279.

(35) Information on the properties of boron carbide. http://www.insaco.com/matpages/mat_display.asp?M=BC (accessed June 6, 2012).

(36) Gielisse, P.; Mitra, S.; Plendl, J.; Griffis, R.; Mansur, L.; Marshall, R.; Pascoe, E. Lattice infrared spectra of boron nitride and boron monophosphide. *Physical Review* **1967**, *155*, 1039–1046.

(37) Iwami, M.; Tohda, T.; Kammura, W.; Kawabe, K. Crystal growth of boron monophosphide and its properties. *Technology Reports of the Osaka University* **1976**, *26*, 201–209.

(38) Feng, X.; Shi, L.; Hang, J.; Zhang, J.; Fang, J.; Zhong, Q. Low temperature synthesis of boron phosphide nanocrystals. *Materials Letters* **2005**, *59*, 865–867.

(39) Chu, T.; Gill, M.; Smeltzer, R.; Chu, T. L.; Gill, M.; Smeltzer, R. K. Growth of boron monophosphide crystals with the accelerated container rotation technique. *Journal of Crystal Growth* **1976**, *33*, 53–57.

(40) Chu, T. L.; Jackson, J. M.; Hyslop, A. E.; Chu, S. C. Crystals and epitaxial layers of boron phosphide. *Journal of Applied Physics* **1971**, *42*, 420.

(41) Kumashiro, Y.; Yoshizawa, H.; Yokoyama, T. Epitaxial growth of rhombohedral boron phosphide single crystalline films by chemical vapor deposition. *Journal of Solid State Chemistry* **1997**, *133*, 104–112.

(42) Schroten, E.; Goossens, A.; Schoonman, J. Photo-and electroreflectance of cubic boron phosphide. *Journal of applied physics* **1998**, *83*, 98–101.

(43) Elwell, D.; Scheel, H. J. *Crystal Growth from High-Temperature Solutions*; Academic Press Inc.: New York, 1975; Vol. 11, pp. 28–29.

(44) Yamamoto, M.; Hamazaki, Y.; Tsukihara, M.; Naoi, Y.; Nishino, K.; Sakai, S. Growth of AlN and GaN by metalorganic chemical vapor deposition on BP synthesized by flux Method. *Japanese Journal of Applied Physics* **2007**, *46*, L323–L325.

(45) Kumashiro, Y.; Yao, T.; Gonda, S. Crystal growth of boron phosphide by high pressure flux method. *Journal of Crystal Growth* **1984**, *70*, 515–518.

(46) Taskinen, P. Thermodynamic assessment of Ni-B phase diagram. *Materials Science and Technology* **1993**.

(47) Iwami, M.; Fujita, N.; Kawabe, K. Preparation of BP single crystals from B-Ni-P solution. *Japanese Journal of Applied Physics* **1971**, *10*, 1746.

(48) Iseler, G.; Clark Jr, H.; Bliss, D. Time and temperature dependence of phosphorus vapor pressure as measured by a pressure-balanced, sealed-ampoule technique. In *Indium Phosphide and Related Materials, 1992., Fourth International Conference on*; IEEE, 1992; pp. 266–269.

(49) Bachmann, K.; Buehler, E. Phase equilibria and vapor pressures of pure phosphorus and of the indium/phosphorus system and their implications regarding crystal growth of InP. *Journal of the Electrochemical Society* **1974**.

(50) Weyher, J.; Brown, P.; Rouviere, J. Recent advances in defect-selective etching of GaN. *Journal of Crystal Growth* **2000**, *210*, 151–156.

(51) Lessoff, H.; Gorman, R. A eutectic dislocation etch for gallium arsenide. *Journal of Electronic Materials* **1985**, *14*, 203–203.

(52) Zhuang, D. Bulk AlN crystal growth by direct heating of the source using microwaves. *Journal of Crystal Growth* **2004**, *262*, 168–174.

(53) Rouviere, J. L.; Weyher, J. L.; Seelmann-Eggebert, M.; Porowski, S. Polarity determination for GaN films grown on (0001) sapphire and high-pressure-grown GaN single crystals. *Applied Physics Letters* **1998**, *73*, 668.

(54) Whiteley, C. E.; Zhang, Y.; Gong, Y.; Bakalova, S.; Mayo, a.; Edgar, J. H.; Kuball, M. Semiconducting icosahedral boron arsenide crystal growth for neutron detection. *Journal of Crystal Growth* **2011**, *318*, 553–557.

(55) Schroder, D. K. *Semiconductor material and device characterization*; Wiley-Interscience publication.: New York, 1990.

(56) Everhart, T.; Thornley, R. Wide-band detector for micro-microampere low-energy electron currents. *Journal of Scientific Instruments* **1960**, *246*.

(57) Callister, Jr., W. D. *Materials Science and Engineering An Introduction*; 2nd Ed.; Wiley, 1990; pp. 54–59.

(58) Ishida, H. *Characterization of Composite Materials*; Momentum Press, 2010.

(59) Sanjurjo, J.; Lopez-Cruz, E. Dependence on volume of the phonon frequencies and the ir effective charges of several III-V semiconductors. *Physical Review B* **1983**, *28*, 4579–4584.

(60) Sze, S. M. *Semiconductor Devices Physics and Technology*; 2nd Ed.; Wiley, 2002.

(61) Zeghbroeck, B. V. Principles of Electronic Devices. http://ecee.colorado.edu/~bart/book/ (accessed December 8, 2012).

(62) The Hall Effect. http://www.nist.gov/pml/div683/hall_effect.cfm#lorentz (accessed December 8, 2012).

(63) Massalski, T. B. *Binary Alloy Phase Diagrams*; Massalski, T. B., Ed.; ASM International, 1990; Vol. 2, pp. 787–789.

(64) Abe, Y.; Komiyama, J.; Suzuki, S.; Nakanishi, H. SiC epitaxial growth on Si(001) substrates using a BP buffer layer. *Journal of Crystal Growth* **2005**, *283*, 41–47.

(65) Ovsyannikov, S. V.; Polian, A.; Munsch, P.; Chervin, J.-C.; Le Marchand, G.; Aselage, T. L. Raman spectroscopy of $B_{12}As_2$ and $B_{12}P_2$ up to 120 GPa: Evidence for structural distortion. *Physical Review B* **2010**, *81*, 1–4.

(66) Aselage, T. L.; Tallant, D. R.; Emin, D. Isotope dependencies of Raman spectra of $B_{12}As_2$, $B_{12}P_2$, $B_{12}O_2$, and $B_{12+x}C_{3-x}$: Bonding of intericosahedral chains. *Physical Review B* **1997**, *56*, 3122–3129.

(67) Kagamida, M.; Kanda, H.; Akaishi, M.; Nukui, A. Crystal growth of cubic boron nitride using Li_3BN_2 solvent and morphology of the grown crystal. *Science and Technology of New Diamond* **1990**, 221–225.

(68) Ryan, F.M. Miller, R. C. Photoluminescence and pair spectrum in boron phosphide. *Physical Review* **1966**, *148*, 858–862.

(69) Takenaka, T.; Takigawa, M.; Shohno, K. Dielectric constant and refractive index of boron monophosphide. *Japanese Journal of Applied Physics* **1976**, *15*, 2021–2022.

(70) Dalui, S.; Pal, a Synthesis of n-type boron phosphide films and formation of Schottky diode: Al/n-BP/Sb. *Applied Surface Science* **2007**, *254*, 3540–3547.

(71) Nishinaga, T.; Mizutani, T. Effect of growth parameters on the epitaxial growth of BP on Si substrate. *Japanese Journal of Applied Physics* **1975**, *14*, 753–760.

(72) Tsoulfanidis, N.; Landsberger, S. *Measurement and detection of radiation*; 3rd ed.; CRC press, 2011; pp. 202–203.

Chapter 5 - Appendix

Flux growth of boron phosphide (BP) crystals procedure

Purpose

The goal of this experiment is to grow BP crystals of high structural quality and low residual impurity concentrations using the flux growth method.

Hazards

Red phosphorus is one of the source materials employed in this project. It comes in powder form or 1-5mm chunks. It is a flammable solid, and will ignite at sudden impacts. At normal temperature and humidity, red phosphorus reacts slowly with water vapor and oxygen in the air to form phosphine gas, which is extremely toxic; therefore it should be handled carefully with minimum exposure to air.

White phosphorus is formed in the sealed quartz tube during high temperature experiments. It is highly flammable and pyrophoric (self-igniting) upon contact with air and is toxic (causing severe liver damage on ingestion). The fumes of combustion of phosphorus consist of phosphorus pentoxide (P_4O_{10}), which is also highly toxic if inhaled. It is recommended to wear appropriate personal protective equipment (PPE) (shaded face shield, apron and thermal gloves), and also to work under a high performance fume-hood when opening a quartz tube containing white phosphorus.

Quartz tube pressure is very important to monitor during experiments. The rupture pressure of the quartz tube is rated as 5 atmospheres at room temperature. An overpressure of the quartz tube during experiments will result in rupture, thus causing an explosion due to white phosphorus being exposed to air. To avoid such accidents, one end of the sealed quartz tube is kept at a temperature between (but no more than) 430-450°C, which keeps the tube's pressure between 1-3 atmospheres during experiments.

Procedure

First, slowly add pure phosphorus powder (or chunks) to the fused end of a 25mm ID x 28.8mm OD x 500mm long quartz tube. Next, mix boron and nickel powder in a Pyrolytic boron nitride boat, and place the boat into the quartz tube.

Next, connect the quartz tube to a vacuum system, and heat with heating tape to about 100°C to remove adsorbed water and other volatile impurities. Evacuate the system while it is heated overnight to pressure of about 10^{-6} Torr. Seal the quartz tube under vacuum using a hydrogen and oxygen torch. And then place the sealed tube in a multi zone furnace.

Slowly heat up the end containing nickel and boron to 1150°C within 12 hours, while simultaneously heating the end containing phosphorus to 430°C within 24 hours. Hold the temperature of the nickel and boron end at 1150°C for 24 hours and then cool to 1000°C at a rate of 3°C per an hour. Quench cool the whole system to room temperature.

After growth, with the appropriate PPE and under a fume hood, cut the quartz tube open with a diamond saw, and let the tube vent. Pull out the nickel melt containing the BP crystals from the tube and put it in Aqua Regia (a mixture of nitric acid and hydrochloric acid, at volumetric ratio 1:3) overnight to etch the nickel away from the crystals at room temperature. Finally, rinse the leftover crystals with water and let air dry.